A kinetic-based model for polydisperse, high-speed, fluid–particle flows

Rodney O. Fox, Jacob W. Posey, Ryan W. Houim, Frédérique Laurent

A Kinetic-Based Model for Polydisperse, High-Speed, Fluid–Particle Flows

Rodney O. Fox[a,b,d], Jacob W. Posey[c], Ryan W. Houim[c], Frédérique Laurent[d]

[a]*Department of Chemical and Biological Engineering, Iowa State University, Ames, IA 50011-1098, USA*
[b]*Center for Multiphase Flow Research and Education, Iowa State University, Ames, IA 50011, USA*
[c]*Department of Mechanical and Aerospace Engineering, University of Florida, Gainesville, FL 32611, USA*
[d]*Laboratoire EM2C, CNRS, CentraleSupélec, Université Paris-Saclay, 91192 Gif-sur-Yvette, France*

Abstract

Hyperbolic conservation equations for polydisperse, high-speed, compressible, fluid–particle flows with added mass and fluid-phase pseudoturbulence are derived. First, the kinetic-based model for monodisperse particles that accounts for collisional and frictional pressure, as well as added mass and internal energy, is reviewed. Then, a kinetic-based model for polydisperse particles is formulated in terms of the moments of the particle size distribution, and velocity moments conditioned on the particle mass or size. Transport equations for velocity moments up to second order (or total kinetic energy) are closed using the hyperbolic quadrature method of moments. In the numerical implementation for the spatial fluxes and source terms, the particle mass distribution is treated using the generalized quadrature method of moments and the size-conditioned moments are found with the conditional quadrature method of moments. Example results for spatially 1-D test cases demonstrate the ability of the polydisperse model to capture a wide range of particle-size-dependent multiphase flow physics.

Keywords: fluid–particle flow, polydispersity, kinetic theory of granular flow, quadrature-based moment methods, added mass, pseudoturbulence

1. Introduction

Compressible polydisperse multiphase flows are ubiquitous in nature and important to many industrial applications. Particle size distributions are required to describe the dynamics of volcanic ash plumes and pyroclastic flows [23], triboelectric charging [8], cloud formation and precipitation [4], the dispersal of dust layers by shock waves [20], and the ignition and combustion explosively dispersed powders [25]. Experimentation of these multiphase flows are challenging due to their extreme conditions and high optical thicknesses hindering modern diagnostic techniques. As a result, numerical simulations are often required to obtain a detailed understanding of these flows. Lagrangian point-particle methods can naturally handle polydisperse flows, but are limited to systems where the number of particles is computationally feasible. This presents a barrier to practical scenarios that can involve many trillions of particles.

Eulerian multiphase flow models can naturally handle large numbers of particles, but are typically limited to monodisperse size distributions [2, 5, 6, 18]. Recently developed Eulerian models have included polydisperse size distributions using binning approaches [20]. These approaches require a large number of bins to accurately reconstruct realistic size distributions, which is impractical for many realistic scenarios. Quadrature-based moment methods (QBMM) have recently been adapted to incompressible polydisperse multiphase flows [19]. The number of transported quantities is significantly reduced for QBMM relative to binning. Nevertheless, thus far polydisperse multiphase flows have only been applied to low-speed incompressible flows. Extending the QBMM to high-speed, compressible, polydisperse flows is the main objective of this work.

In this work, we derive the hyperbolic conservation equations for polydisperse, high-speed, collisional particle flows with added mass and internal energy starting from a kinetic model for granular flows. These equations are

Email addresses: rofox@iastate.edu (Rodney O. Fox), jposey@ufl.edu (Jacob W. Posey), rhouim@ufl.edu (Ryan W. Houim), frederique.laurent@centralesupelec.fr (Frédérique Laurent)

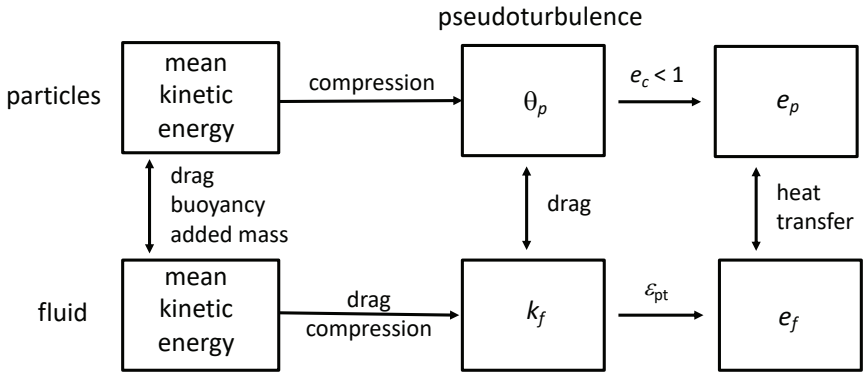

Figure 1: Energy flow in fluid–particle macroscale model from [6]. Random particle motion is measured by Θ_p, while particle-scale, fluid-phase, fluctuating kinetic energy is measured by k_f. The internal energies e_f and e_p define by the thermodynamic temperatures T_p and T_f (°K). Inelastic collisions transform Θ_p into an increase in e_p. Pseudoturbulent dissipation ε_{pt} transform k_f into an increase in e_f. At each scale, the phases are coupled through drag or heat transfer. Compression in the particle phase increases α_p, while in the fluid phase it increases ρ_f.

coupled with modified Euler equations for the fluid phase, including pseudoturbulent kinetic energy (PTKE). Details for the monodisperse case can be found in prior work [6]. The fluid phase is treated as ideal and inviscid with coupling terms discussed in [14]. The particle phase is treated as inviscid with inelastic collisions, and a frictional-pressure term is added to handle dense cases. Particle velocity moments up to second order (total kinetic energy) are included. The diagram in fig. 1 provides a schematic on how kinetic energy is distributed in the compressible fluid–particle flow. Given that most of the physical models have been described in detail for monodisperse particles in [6], the main focus of this work is on how polydispersity in particle mass is handled using QBMM.

2. Macroscale model for monodisperse, high-speed, fluid–particle flows

In this section, the macroscale model for monodisperse particles derived in [6] and applied in [5] to model shock–particle-curtain experiments is reviewed. Here, macroscale refers to the Euler–Euler model found from the moments of a kinetic-based mesoscale model. The latter is related to an Euler–Lagrange description such as the one proposed in [7]. The principal objective of this section is to remind the reader how added mass, internal energy, and PTKE are treated, and to introduce the notation used in the rest of the paper. The monodisperse model equations for the nine conserved variables are summarized in tables 1 and 2, and example parameter values for fluid–particle flow are given in table 3.

The variable fluid density is denoted by ρ_f, and the constant solid density by ρ_p, both have units kg/m^3. The fluid- and particle-phase velocities are $\mathbf{u}_f$ and $\mathbf{u}_p$, respectively, with units m/s. The total energies of the fluid and particle phases are denoted as E_f and E_p, respectively. The total energy is the sum of kinetic and internal energies. We denote the former for each phase as K_f and K_p, and the latter as e_f and e_p. (All energy variables have units of m^2/s^2.) The phasic total energies are thus $E_f = K_f + e_f$ and $E_p = K_p + e_p$. The total kinetic energy is divided into mean and fluctuating components (see fig. 1):

$$K_f = \frac{1}{2}u_f^2 + k_f \quad \text{and} \quad K_p = \frac{1}{2}u_p^2 + \frac{3}{2}\Theta_p. \tag{1}$$

Here, $u^2 = \mathbf{u} \cdot \mathbf{u}$, k_f is the PTKE and Θ_p is the granular "temperature". For the fluid phase, it is convenient to solve transport equations for E_f and k_f. In contrast, for the particle phase, the kinetic description leads naturally to transport equations for K_p and e_p. In any case, the thermodynamic temperatures T_f and T_p (units °K) are found from the internal energies e_f and e_p, respectively, using the heat capacities for each phase [18]. The equation for PTKE has production terms due to drag and turbulent dissipation (term with C_f) at the length scale of the particle diameter [27].

In our modeling approach, added mass is handled by assigning a fraction of the fluid phase surrounding a particle to move with the velocity $\mathbf{u}_p$ of the particle phase [14]. In the context of two-fluid models, we define $\alpha_p^\star = \alpha_p + \alpha_a$

Table 1: Nine-equation macroscale model for monodisperse fluid–particle flow derived in [6] and written in conservative form. Gravity $\mathbf{g}$ is included in the model for completeness. The pfp-pressure tensor $\mathbf{P}_{pfp}$ appears as flux in the particle-phase momentum balance and a work term in the energy balances. Alternatively, it can be written as a force in the momentum balances [14].

Mass balances:

$$\partial_t \alpha_p + \partial_{\mathbf{x}} \cdot \alpha_p \mathbf{u}_p = 0$$
$$\partial_t \rho_f \alpha_f^\star + \partial_{\mathbf{x}} \cdot \rho_f \alpha_f^\star \mathbf{u}_f = -S_a$$
$$\partial_t \rho_e \alpha_p^\star + \partial_{\mathbf{x}} \cdot \rho_e \alpha_p^\star \mathbf{u}_p = S_a$$

Momentum balances:

$$\partial_t \rho_f \alpha_f^\star \mathbf{u}_f + \partial_{\mathbf{x}} \cdot (\rho_f \alpha_f^\star \mathbf{u}_f \otimes \mathbf{u}_f + \hat{p}_f \mathbf{I}) = \alpha_p^\star (\partial_{\mathbf{x}} \hat{p}_f + \mathbf{F}_{pf}) + \frac{\rho_e \alpha_p^\star}{\tau_p} \mathbf{u}_{pf} - \mathbf{S}_{fp} + \rho_f \alpha_f^\star \mathbf{g}$$
$$\partial_t \rho_e \alpha_p^\star \mathbf{u}_p + \partial_{\mathbf{x}} \cdot \rho_e \alpha_p^\star (\mathbf{u}_p \otimes \mathbf{u}_p + \Theta_p \mathbf{I} + P_p \mathbf{I} + \mathbf{P}_{pfp}) = -\alpha_p^\star (\partial_{\mathbf{x}} \hat{p}_f + \mathbf{F}_{pf}) - \frac{\rho_e \alpha_p^\star}{\tau_p} \mathbf{u}_{pf} + \mathbf{S}_{fp} + \rho_e \alpha_p^\star \mathbf{g}$$

Fluid-phase energy balances (total and PTKE):

$$\partial_t \rho_f \alpha_f^\star E_f + \partial_{\mathbf{x}} \cdot [\rho_f \alpha_f^\star \mathbf{u}_f E_f + (\alpha_f^\star \mathbf{u}_f + \alpha_p^\star \mathbf{u}_p) \hat{p}_f] = -\mathbf{P}_{pfp} : \partial_{\mathbf{x}} \mathbf{u}_p + \alpha_p^\star \mathbf{u}_p \cdot (\partial_{\mathbf{x}} \hat{p}_f + \mathbf{F}_{pf})$$
$$+ \frac{\rho_e \alpha_p^\star}{\tau_p} [3a\Theta_p - 2(1-a)k_f + \mathbf{u}_{pf} \cdot \mathbf{u}_p] + H_{pf} - S_E + \rho_f \alpha_f^\star \mathbf{u}_f \cdot \mathbf{g}$$
$$\partial_t \rho_f \alpha_f^\star k_f + \partial_{\mathbf{x}} \cdot \rho_f \alpha_f^\star \mathbf{u}_f k_f + \frac{2}{3} \rho_f \alpha_f^\star k_f \partial_{\mathbf{x}} \cdot \mathbf{u}_f = \frac{\rho_e \alpha_p^\star}{\tau_p} [3a\Theta_p - 2(1-a)k_f + u_{pf}^2 - C_f k_f]$$

Particle-phase energy balances (kinetic and internal):

$$\partial_t \rho_e \alpha_p^\star K_p + \partial_{\mathbf{x}} \cdot [\rho_e \alpha_p^\star \mathbf{u}_p (K_p + \Theta_p + P_p) + \mathbf{P}_{pfp} \cdot \mathbf{u}_p] = \mathbf{P}_{pfp} : \partial_{\mathbf{x}} \mathbf{u}_p - \alpha_p^\star \mathbf{u}_p \cdot (\partial_{\mathbf{x}} \hat{p}_f + \mathbf{F}_{pf})$$
$$- \frac{\rho_e \alpha_p^\star}{\tau_p} [3a\Theta_p - 2(1-a)k_f + \mathbf{u}_{pf} \cdot \mathbf{u}_p] - H_p + S_K + \rho_e \alpha_p^\star \mathbf{u}_p \cdot \mathbf{g}$$
$$\partial_t \rho_e \alpha_p^\star e_p + \partial_{\mathbf{x}} \cdot \rho_e \alpha_p^\star e_p \mathbf{u}_p = H_p - H_{pf} + S_e$$

Table 2: Parameters appearing in macroscale model in table 1. In the definition of $\mathbf{R}$, the parameters must satisfy $3B_1 + B_2 > 0$ so that $tr(\mathbf{R}) = u_{pf}^2$ and $C_{pfp} > 0$. The correlations for B_1 and B_2 come from [30], and are valid for a limited range of Re_p and $\alpha_p > 0.01$. For smaller α_p, B_1 can be taken as constant. The thermodynamic temperatures T_f and T_p are found from the internal energies of their respective phases. λ_f is the fluid-phase thermal conductivity.

$$\kappa = \frac{\rho_e\alpha_p^\star - \rho_p\alpha_p}{\rho_f\alpha_f^\star} \qquad \alpha_f = 1 - \alpha_p \qquad \alpha_a = \frac{\kappa}{1+\kappa}\alpha_f \qquad \alpha_p^\star = \alpha_p + \alpha_a \qquad \alpha_f^\star = \alpha_f - \alpha_a \qquad \mathbf{u}_{pf} = \mathbf{u}_p - \mathbf{u}_f$$

$$\mathbf{R} = \frac{B_1 u_{pf}^2 \mathbf{I} + B_2 \mathbf{u}_{pf} \otimes \mathbf{u}_{pf}}{3B_1 + B_2} \quad \mathbf{P}_{pfp} = C_{pfp}\rho_f\alpha_p^\star\mathbf{R} \quad \mathbf{F}_{pf} = \mathbf{R}\cdot\partial_\mathbf{x}\rho_f - (\gamma_f - 1)\rho_f(\partial_\mathbf{x}\cdot\mathbf{u}_f)\mathbf{u}_{pf} + C_l\rho_f\mathbf{u}_{pf}\times(\partial_\mathbf{x}\times\mathbf{u}_f)$$

$$S_a = \frac{\rho_f}{\tau_a}(c_m^\star\alpha_f\alpha_p - \alpha_a) \qquad \mathbf{S}_{fp} = \max(S_a, 0)\,\mathbf{u}_f + \min(S_a, 0)\,\mathbf{u}_p \qquad S_E = \max(S_a, 0)\,E_f + \min(S_a, 0)\,E_p$$

$$S_K = \max(S_a, 0)\,K_f + \min(S_a, 0)\,K_p \qquad S_e = \max(S_a, 0)\,e_f + \min(S_a, 0)\,e_p \qquad H_{pf} = \frac{6\alpha_p^\star\lambda_f Nu}{d_p^2}(T_p - T_f)$$

$$Re_p = \frac{d_p\nu_{pf}}{\nu_f} \quad Pr_f = \frac{\rho_f C_{p,f}\nu_f}{\lambda_f} \quad Nu = (7 - 10\alpha_f + 5\alpha_f^2)(1 + 0.7Re_p^{0.2}Pr_f^{1/3}) + (1.33 - 2.4\alpha_f + 1.2\alpha_f^2)Re_p^{0.7}Pr_f^{1/3}$$

$$v_{pf} = \frac{\alpha_f^\star}{\alpha_f}u_{pf} \quad c_m^\star = \frac{1}{2}\min(1 + 2\alpha_p, 2) \quad \tau_a = C_a\tau_p \quad \tau_p = \frac{4\rho_e d_p^2}{3\mu_f C_D Re_p} \quad C_D = \frac{24}{Re_p}\left(1 + 0.15Re_p^{0.687}\right)\alpha_f^{-2.65}$$

$$\tau_c = \frac{d_p\sqrt{\pi}}{12\alpha_p g_0 \Theta_p^{1/2}} \quad \tau_{fr} = \frac{c_{fr}}{h_{fr}(\alpha_p)\max(|\partial_\mathbf{x}\cdot\mathbf{u}_p|, 1/\tau_c)} \qquad g_0 = \frac{1 + \alpha_f}{2\alpha_f^3} \quad h_{fr}(\alpha_p) = \frac{1}{2}\left[1 + \tanh\left(\frac{\alpha_p - \alpha_{max}}{\Delta_{fr}}\right)\right]$$

$$p_f = (\gamma_f - 1)\rho_f e_f - \gamma_f p_{\infty,f} \qquad e_f = E_f - \frac{1}{2}u_f^2 - k_f \qquad \Theta_p = \frac{2}{3}K_p - \frac{1}{3}u_p^2 \qquad H_p = \rho_e\alpha_p^\star\left[\frac{1}{\tau_c}(1 - e_c^2) + \frac{1}{\tau_{fr}}\right]\Theta_p$$

$$\hat{p}_f = p_f + \frac{2}{3}\rho_f k_f \qquad P_p = P_c + P_{fr} \qquad P_c = 2(1 + e_c)\alpha_p g_0 \Theta_p \qquad P_{fr} = \frac{p_{fr}\alpha_p g_0}{\rho_e\alpha_p^\star}h_{fr}(\alpha_p)$$

$$T_f = \frac{\gamma_f e_f}{C_{p,f}} \qquad T_p = \frac{e_p}{C_{p,p}} \qquad C_f^{-1} = \alpha_p[1 + 1.25\alpha_f^3\exp(-\alpha_p\alpha_f^{1/2}Re_p^{1/2})] \qquad \frac{1-a}{1-a_{min}} = \frac{\rho_f}{\rho_p K + \rho_f} \qquad C_{pfp} = c_m^\star$$

Table 3: Default model constants for fluid–particle flow examples.

$$B_1 = \max(1.0915 - 0.95Re_p^{0.02} + 0.01\ln\alpha_p, -B_2) \quad B_2 = -\max(0.4046Re_p^{-0.3} - 0.042, 0)$$

$$a_{min} = 0.5 \quad K = 0.06 \quad C_l = 0.5 \quad C_a = 1 \quad c_{fr} = 0.01 \quad \alpha_{max} = 0.63 \quad \Delta_{fr} = 0.01 \quad p_{fr} = 533,333\ \text{kg/m/s}^2$$

$$e_c = 0.9 \quad \nu_f = 1.48\times10^{-5}\ \text{m}^2/\text{s} \quad \gamma_f = 1.4 \quad \lambda_f = 0.026\ \text{kg m/s}^3/\text{K} \quad C_{p,f} = 1005\ \text{m}^2/\text{s}^2/\text{K} \quad C_{p,p} = 840\ \text{m}^2/\text{s}^2/\text{K}$$

where α_a is the volume fraction of the added-mass phase while α_p is the particle-phase volume fraction. It then follows that $\alpha_f^\star = \alpha_f - \alpha_a$ where α_f is the fluid-phase volume fraction. The mass of the fluid, excluding added mass, is then $\rho_f \alpha_f^\star$, while for the particle phase, including the added mass, it is $\rho_e \alpha_p^\star$. The mass of the particle + added-mass phase can be expressed as

$$\rho_e \alpha_p^\star = \rho_p \alpha_p + \rho_f \alpha_a = (\rho_p - \rho_f)\alpha_p + \rho_f \alpha_p^\star, \tag{2}$$

which defines the effective density ρ_e. In the mass balances, S_a is the mass-transfer rate from the fluid phase to the added-mass phase with timescale τ_a, and $\mathbf{S}_{fp}$ and S_E are the corresponding rates for momentum and energy. Notice that the velocity of the fluid phase (including the added mass) is $\mathbf{v}_f = (\alpha_f^\star \mathbf{u}_f + \alpha_a \mathbf{u}_p)/\alpha_f$ [14]. Thus, the slip velocity without added mass $\mathbf{v}_{pf} = (\alpha_f^\star/\alpha_f)(\mathbf{u}_p - \mathbf{u}_f)$ is always smaller than the slip velocity denoted by $\mathbf{u}_{pf} = \mathbf{u}_p - \mathbf{u}_f$. This difference must be taken into account when applying drag (or other) correlations from the literature that depend on $\mathbf{v}_{pf}$ (e.g., through the particle Reynolds number Re_p).

In the momentum and energy balances, $\hat{p}_f = p_f + \frac{2}{3}\rho_f k_f$ is the modified fluid pressure, and $\mathbf{D}$, D_{PT}, and D_E represent drag exchange with the particle phase with timescale τ_p. The fluid pressure p_f is found from the pure fluid-phase equation of state (i.e., it does not depend on α_p). In the total energy balance, H_{pf} represents convective heat transfer from the particle phase due to the temperature (and velocity) difference [18]. The slip-pressure tensor $\mathbf{R}$ and exchange term $\mathbf{F}_{pf}$ arise due to finite-size particles [14], and are the same as when added mass is neglected. The particle–fluid–particle pressure tensor $\mathbf{P}_{pfp}$ modifies the particle-phase pressure tensor and ensures hyperbolicity [14]. Because it scales with the fluid density, $\mathbf{P}_{pfp}$ is less important for heavy particles ($\rho_f \ll \rho_p$); however, it can produce a significant pressure in the particle phase in high-speed flows with very large u_{pf} [5]. In the energy balances, the term $\mathbf{P}_{pfp} : \partial_{\mathbf{x}} \mathbf{u}_p$ represents the work done by the fluid on the particles to lower the particle-phase volume fraction.

In the model, ρ_p is constant, but ρ_f changes due to compression/expansion of the fluid. Thus, given α_p from the particle-phase mass balance and the conserved variables $\rho_e \alpha_p^\star$ and $\rho_f \alpha_f^\star$, α_a is found from

$$\alpha_a = \frac{\kappa}{1+\kappa}(1-\alpha_p) \qquad \text{with} \qquad \kappa = \frac{\rho_e \alpha_p^\star - \rho_p \alpha_p}{\rho_f \alpha_f^\star} = \frac{\alpha_a}{\alpha_f^\star} \tag{3}$$

and $\alpha_f = 1 - \alpha_p$. Then $\alpha_p^\star = \alpha_p + \alpha_a$ and $\alpha_f^\star = \alpha_f - \alpha_a$, so that ρ_f is found from the conserved variable $\rho_f \alpha_f^\star$. The detailed derivation of the monodisperse two-fluid model is available in [6], and follows the same procedure employed for polydisperse particles described below. An extended discussion of the physical meaning of each term in the nine-equation macroscale model in table 2, and a robust numerical solution algorithm for the balance equations can be found in [6] and references cited therein (e.g., [10, 14]).

In any case, summing together the balance equations for the two phases, it is straightforward to show that mass ($\rho_f \alpha_f^\star + \rho_e \alpha_p^\star$), momentum ($\rho_f \alpha_f^\star \mathbf{u}_f + \rho_e \alpha_p^\star \mathbf{u}_p$) and total energy ($\rho_f \alpha_f^\star E_f + \rho_e \alpha_p^\star E_p$) are conserved.[1] Compared to "standard" multi-fluid models, the spatial fluxes reflect the mesoscale physics incorporated in the kinetic-based description of the disperse phase (e.g., the particle-phase pressures P_p and $\mathbf{P}_{pfp}$ and the fluid pressure p_f seen by the particles). Thus, the most important terms in the two-fluid model are closed at the level of the kinetic description, and no additional information need be introduced (e.g., the mixture equation of state) as is the case for multi-fluid models derived using phase averages [17]. More importantly, as shown next, the kinetic-based description developed for monodisperse particles extends naturally to polydisperse particles.

3. Kinetic-based model for polydisperse particles

In this section, a 1-D size space and 3-D velocity space kinetic model is developed for polydisperse particles with added mass. The principal objective is to demonstrate how polydisperse particles are treated using QBMM [19]. A key assumption made in the following equations is that ρ_e is the same for all particles at the same location. This essentially amounts to assuming that α_a is proportional to the volume fraction of each particle size: $\alpha_p = \int \alpha(\xi)\,\mathrm{d}\xi$ where $\alpha(\xi)\,\mathrm{d}\xi$ is the volume fraction of particles of mass ξ.[2] This assumption implies that the added-mass factor

[1] For constant ρ_f, conservation of mixture volume leads to the constraint $\partial_{\mathbf{x}} \cdot (\alpha_f^\star \mathbf{u}_f + \alpha_p^\star \mathbf{u}_p) = 0$, which determines the fluid pressure p_f.

[2] $\alpha(\xi) = V_p(\xi) n(\xi)$ where $V_p(\xi)$ is the volume of a particle with mass ξ and $n(\xi)$ is their number concentration. Here, particles are approximated by spheres with diameter $d_p(\xi)$.

$\beta(t, \mathbf{x})$, defined by (c_m is related to the added-mass constant [6])

$$\beta = \frac{\rho_e \alpha_p^\star}{\rho_p \alpha_p} = 1 + \frac{\rho_f \alpha_a}{\rho_p \alpha_p} = 1 + c_m \alpha_f \frac{\rho_f}{\rho_p}, \tag{4}$$

which does not depend on ξ. In words, if m_p is the particle mass, then $m_p^\star = \beta m_p$ with $\beta \geq 1$ is its effective mass (i.e., including the added mass). Thus, when $\xi = m_p$ is a distributed variable as in the polydisperse model, its local effective mass $m_p^\star = \beta(t, \mathbf{x})\xi$ is also a distributed variable that is linearly proportional to ξ. As shown below, the kinetic model for the polydisperse case will be expressed in terms of the particle mass ξ, instead of the effective mass.

After manipulating the mass balances for $\rho_e \alpha_p^\star$ and $\rho_p \alpha_p$ from table 1, we find the transport equation for the added-mass factor:

$$\partial_t \beta + \mathbf{u}_p \cdot \partial_{\mathbf{x}} \beta = \frac{1}{\tau_a}(\beta^\star - \beta) \tag{5}$$

where $\beta^\star = 1 + c_m^\star \alpha_f \rho_f / \rho_p$ is the local equilibrium value of β. For β to be independent of ξ, τ_a must be independent of ξ. In the dilute limit ($\alpha_f \to 1$), $c_m^\star$ is the added-mass constant. In practice, τ_a is small enough that $\beta \approx \beta^\star$ in most regions of the flow [14]. In summary, the effective particle density $\rho_e(t, \mathbf{x})$ defined in eq. (2) and the added-mass factor $\beta(t, \mathbf{x})$ defined by eq. (4) do not depend on the particle size in the polydisperse macroscale model derived below. This is equivalent to taking the size-dependent added volume to be $\alpha_a(\xi) = c_m^\star \alpha_f \alpha(\xi)$. As done in the monodisperse model, in the polydisperse model we solve a transport equations for $\rho_e \alpha_p^\star$ and α_p, which is equivalent to solving for β using eq. (5).

3.1. Definitions

For polydisperse particles, we must extend the velocity distribution function used in [6] to include the particle mass. Let ξ be the particle mass and $\mathbf{u}$ be its particular velocity in the sense of kinetic theory [10]. As in [6], e is the particle internal energy. Dropping the space and time variables, the number-based distribution function for the particles is denoted by $n(\xi, \mathbf{u}, e)$. Then, in order to account for added mass in the momentum balance, we multiply the NDF for the particles by $\beta(t, \mathbf{x})$ to define the joint NDF for mass, velocity and internal energy: [3]

$$f(\xi, \mathbf{u}, e) = \beta\, n(\xi, \mathbf{u}, e). \tag{6}$$

For convenience, we define lower-order distributions functions by integrating over certain variables. For example, the joint mass–velocity NDF, the joint mass–internal-energy NDF, and the mass NDF are, respectively,

$$f(\xi, \mathbf{u}) = \int f(\xi, \mathbf{u}, e)\, \mathrm{d}e, \quad f(\xi, e) = \int f(\xi, \mathbf{u}, e)\, \mathrm{d}\mathbf{u}, \quad n(\xi) = \frac{1}{\beta} \int f(\xi, \mathbf{u}, e)\, \mathrm{d}\mathbf{u}\, \mathrm{d}e = \int n(\xi, \mathbf{u}, e)\, \mathrm{d}\mathbf{u}\, \mathrm{d}e. \tag{7}$$

Thus, if only f appears, then we mean $f(\xi, \mathbf{u}, e)$. Otherwise, the arguments of f will be included. Notice that the mass NDF $n(\xi)$ does not include the added-mass factor. However, if it did, all of the mass moments would be multiplied by β. If these moments were normalized by the zero-order moment, the normalized moments would not depend on β.

In addition to the distributions in eq. (7), we will make use for mass-conditioned variables defined using conditional distributions. For example, $n(\xi, \mathbf{u}, e) = p(\mathbf{u}, e|\xi) n(\xi)$ introduces the conditional probability density function (PDF) $p(\mathbf{u}, e|\xi)$ of velocity and internal energy given particles with fixed mass ξ, which has the property $1 = \int p(\mathbf{u}, e|\xi)\, \mathrm{d}\mathbf{u}\, \mathrm{d}e$. In this manner, we can define mass-conditioned statistics such as velocity, kinetic energy and internal energy:

$$\mathbf{u}_p(\xi) = \int \mathbf{u} p(\mathbf{u}, e|\xi)\, \mathrm{d}\mathbf{u}\, \mathrm{d}e, \quad K_p(\xi) = \int \frac{1}{2} u^2 p(\mathbf{u}, e|\xi)\, \mathrm{d}\mathbf{u}\, \mathrm{d}e, \quad e_p(\xi) = \int e p(\mathbf{u}, e|\xi)\, \mathrm{d}\mathbf{u}\, \mathrm{d}e, \tag{8}$$

respectively. Similarly, we can define the mass-conditioned velocity PDF $p(\mathbf{u}|\xi) = \int p(\mathbf{u}, e|\xi)\, \mathrm{d}e$ and the mass-conditioned internal-energy PDF $p(e|\xi) = \int p(\mathbf{u}, e|\xi)\, \mathrm{d}\mathbf{u}$.

[3] Since ξ is an independent variable, another alternative is to derive the kinetic model using the mass-density function $f(\xi, \mathbf{u}, e) = \beta \xi n(\xi, \mathbf{u}, e)$ [6]. In either case, β is a multiplicative factor that does not depend on the independent variables $(\xi, \mathbf{u}, e)$.

The conserved particle-phase variables (i.e., mass, momentum, internal energy, kinetic energy) that are coupled to the fluid phase are defined by

$$\begin{gathered}\rho_e\alpha_p^\star = \beta\int \xi n(\xi)\,\mathrm{d}\xi, \qquad \rho_e\alpha_p^\star\mathbf{u}_p = \int \xi\mathbf{u}f(\xi,\mathbf{u})\,\mathrm{d}\xi\,\mathrm{d}\mathbf{u} = \beta\int \xi\mathbf{u}_p(\xi)n(\xi)\,\mathrm{d}\xi,\\ \rho_e\alpha_p^\star e_p = \int \xi e f(\xi,e)\,\mathrm{d}\xi\,\mathrm{d}e = \beta\int \xi e_p(\xi)n(\xi)\,\mathrm{d}\xi, \qquad \rho_e\alpha_p^\star K_p = \int \xi\frac{1}{2}u^2 f(\xi,\mathbf{u})\,\mathrm{d}\xi\,\mathrm{d}\mathbf{u} = \beta\int \xi K_p(\xi)n(\xi)\,\mathrm{d}\xi\end{gathered} \tag{9}$$

where we have made use of the distributions defined in eqs. (7) and (8). In addition, to account for the particle mass NDF and to compute the mass-conditioned moments, we will make use of the following higher-order moments in ξ:[4]

$$\begin{gathered}\mathcal{M}_{s/3} = \beta\int \xi^{s/3}n(\xi)\,\mathrm{d}\xi, \quad \mathcal{M}_{s/2} = \beta\int \xi^{s/2}n(\xi)\,\mathrm{d}\xi, \quad \mathcal{M}_s = \beta\int \xi^s n(\xi)\,\mathrm{d}\xi,\\ \boldsymbol{\mathcal{U}}_s^1 = \int \xi^s\mathbf{u}f(\xi,\mathbf{u})\,\mathrm{d}\xi\,\mathrm{d}\mathbf{u} = \beta\int \xi^s\mathbf{u}_p(\xi)n(\xi)\,\mathrm{d}\xi,\\ \mathcal{E}_s = \int \xi^s e f(\xi,e)\,\mathrm{d}\xi\,\mathrm{d}e = \beta\int \xi^s e_p(\xi)n(\xi)\,\mathrm{d}\xi, \qquad \mathcal{K}_s = \int \xi^s\frac{1}{2}u^2 f(\xi,\mathbf{u})\,\mathrm{d}\xi\,\mathrm{d}\mathbf{u} = \beta\int \xi^s K_p(\xi)n(\xi)\,\mathrm{d}\xi\end{gathered} \tag{10}$$

where s is a non-negative integer. Notice that the particle-phase conserved variables in the monodisperse model are related to the above integrals by $\rho_e\alpha_p^\star = \mathcal{M}_1$, $\rho_e\alpha_p^\star\mathbf{u}_p = \boldsymbol{\mathcal{U}}_1^1$, $\rho_e\alpha_p^\star e_p = \mathcal{E}_1$, and $\rho_e\alpha_p^\star K_p = \mathcal{K}_1$. Comparing with eq. (9), we see that the monodisperse model uses $s = 1$ for all moments including the mass $\mathcal{M}_1$. Our principal objective in the remainder of this section is to derive transport equations for the conserved moments in eq. (10) starting from a kinetic model for $f(\xi,\mathbf{u},e)$.[5]

3.2. Kinetic model for polydisperse particles

The generalized population balance equation (GPBE) [22] for the joint mass–velocity–internal-energy number density function (NDF) $f(\xi,\mathbf{u},e)$ is written as

$$\begin{aligned}\partial_t f + \partial_{\mathbf{x}}\cdot\left(\mathbf{u}f - P_p\frac{\partial f}{\partial\mathbf{u}}\right) + \frac{\partial}{\partial\mathbf{u}}\cdot\left[\frac{1}{\tau_p(\xi)}(\mathbf{u}_f-\mathbf{u})\,f - \frac{1}{\rho_e}(\partial_{\mathbf{x}}\hat{p}_f + \mathbf{F}_{pf})f - \frac{1}{\rho_e\alpha_p^\star}(\partial_{\mathbf{x}}\cdot\mathbf{P}_{pfp})f\right] + \frac{\partial}{\partial e}[A_e(\xi)f] =\\ \frac{\partial^2}{\partial\mathbf{u}\partial\mathbf{u}} : [\mathbf{B}_u(\xi)f] + C + F + S.\end{aligned} \tag{11}$$

This GPBE is the same as for the monodisperse case in [6], except that now some of the physical processes depend on the particle mass ξ. As in [6], the particles are assumed to not change mass so that terms involving gradients in ξ phase space are absent in eq. (11). (Numerous examples of a GPBE containing such terms can be found in [22].) The term involving the spatial derivative $\partial_{\mathbf{x}}$ contains free-transport and particle pressure P_p. The terms inside of $\partial_{\mathbf{u}}$ represent particle acceleration due to surface forces (e.g., fluid drag, buoyancy, pfp-pressure). Here, the drag time scale $\tau_p(\xi)$ depends on the particle diameter, while the other forces have the same form as for the monodisperse case. Likewise, the heat-transfer rate $A_e(\xi)$ depends on ξ through the particle diameter.

On the right-hand side, the fluctuation source term for the particle velocity has the form [6]

$$\mathbf{B}_u(\xi) = \frac{1-a}{\tau_p(\xi)}\left[(\mathbf{u}-\mathbf{u}_p(\xi))\otimes(\mathbf{u}-\mathbf{u}_p(\xi)) + \frac{2}{3}k_f\mathbf{I}\right]. \tag{12}$$

The trace of $\mathbf{B}_u(\xi)$ can be conditionally averaged with respect to mass to find

$$\int tr(\mathbf{B}_u)p(\mathbf{u}|\xi)\,\mathrm{d}\mathbf{u} = \frac{1-a}{\tau_p(\xi)}[3\Theta_p(\xi) + 2k_f] \tag{13}$$

[4] Fractional moments with $s/3$ and integer s correspond to a NDF based on a characteristic length [22].

[5] We use $f(\xi,\mathbf{u},e)$ instead of $n(\xi,\mathbf{u},e)$ because the particle acceleration depends on the added mass through $\beta(t,\mathbf{x})$. Nevertheless, using a change of variables, it is straightforward to find the transport equation for $n(\xi,\mathbf{u},e)$ that can be somewhat simplified using eq. (5). In either case, since no processes that change ξ are included, the form of eq. (11) will be the same.

where $\Theta_p(\xi)$ is the mass-conditioned granular temperature. This second form will be needed to solve for the mass-conditioned particle-phase kinetic energy $K_p(\xi)$. The remaining terms (C, F, S) corresponding to point processes [22] are defined below. For example, C represents particle–particle collisions and considers inelastic collisions between particles with different masses (see Appendix A for details).

The GPBE in eq. (11) has the same form as the kinetic equation in [6]. If the particle mass were evolving in time, then there would be additional terms to account for such physics. Hereinafter, we assume that the individual particle masses (in a Lagrangian sense) remain constant. Finally, for simplicity, we take $\mathbf{F}_{pf}$ and $\mathbf{P}_{pfp}$ to be the same as in the monodisperse model (i.e., they do not depend on ξ). An easy generalization for $\mathbf{F}_{pf}$ would be to replace $\mathbf{u}_p$ with the mass-conditioned mean velocity; however, we anticipate that the effect will be small compared to the size-dependent fluid-drag term.

In the monodisperse limit considered in [6], the NDF can be written as $f(\xi, \mathbf{u}, e) = \beta\,\delta(\xi - \xi_m)g(\mathbf{u}, e)$ where ξ_m is the mass (not including added mass) of the particles and $g(\mathbf{u}, e)$ is proportional to the average number of particles with velocity $\mathbf{u}$ and internal energy e per unit volume. Its relationship with the monodisperse $f(\mathbf{u}, e)$ is thus (by integrating ξf first over ξ, and then over $\mathbf{u}$ and e)

$$f(\mathbf{u}, e) = \int \xi f(\xi, \mathbf{u}, e)\,\mathrm{d}\xi = \beta\,\xi_m g(\mathbf{u}, e) \quad \rightarrow \quad \rho_e \alpha_p^\star = \beta\,\xi_m M_0 \tag{14}$$

where M_0 is the number concentration of monodisperse particles. This result also illustrates that when the particles masses do not change, the mass moments of a monodisperse NDF can all be found from M_0 and $\beta\,\xi_m$.

When particles with different chemical composition (and hence different ρ_p) are of interest, eq. (11) is written for each particle type. In addition, collision terms involving different particles types are included. Here, for simplicity, only a single type of particle is considered with constant ρ_p. In a moment approach, the GPBE in eq. (11) is used to derive balances equations for the joint mass–velocity–internal-energy moments of interest. For a polydisperse system, we need a GPBE to account for correlations between mass and velocity, which arise due to the physics contained in eq. (11), e.g., size-dependent fluid drag and heat transfer.

3.3. Size-dependent terms in the GPBE

The particle diameter $d_p(\xi)$ is defined by the relation

$$\xi = \rho_p k_v d_p^3 \tag{15}$$

with volume shape factor $k_v = \frac{\pi}{6}$ for spheres. In eq. (11), $\tau_p(\xi)$ is the size-dependent drag timescale with the fluid phase, C is the source term due to particle–particle collisions [10], and the source term due to friction is modeled as

$$F = \frac{1}{\tau_f}\left[\beta\, n(\xi)\delta(\mathbf{u} - \mathbf{u}_p)\delta[e - e_p(\xi) - Q(\xi)] - f(\xi, \mathbf{u}, e)\right] \tag{16}$$

with τ_f defined in table 2. Here, Q is defined such that the particle-phase kinetic energy loss due to friction is transferred to internal energy (see $\mathcal{F}_s^2$ in eqs. (32), (36) and (38)) at a rate proportional to the particle mass. For clarity, and except for added mass, we neglect processes that change the particle mass, such as mass transfer between phases, and aggregation and breakage due to compression. However, such terms are treated in the kinetic formulation similar to added mass.

For simplicity, the particle-phase pressures $P_p = P_c + P_{fr}$ and $\mathbf{P}_{pfp}$ are assumed to not depend explicitly on the distributed variables $(\xi, \mathbf{u}, e)$. As a first approximation, this choice is reasonable because $\mathbf{P}_{pfp}$ is mainly needed to ensure global hyperbolicity in extreme cases such as zero granular temperature. Under 'normal' conditions, it is small compared to the particle pressure and can be modeled using the average slip velocity. Likewise, P_{fr} controls the eigenvalues for dense granular flows and will have the same qualitative effects as for monodisperse particles. In principle, it is possible to allow the collisional pressure P_c to be size dependent; however, this must be done with care to ensure the correct behavior in limiting cases (e.g., monodisperse limit). For simplicity, here we employ a polydisperse collisional pressure of the form

$$P_c = \frac{\beta}{\rho_p}\int \xi\, p_c(\xi) n(\xi)\,\mathrm{d}\xi \tag{17}$$

where a closed expression for $p_c(\xi)$ has been derived from kinetic theory [10, 19] and is given in eq. (A.18). Alternatively, one can employ the size-dependent collisional pressure described in Appendix A.3, which is well suited for the QBMM introduced in section 4.

3.4. Source term for mass exchange in the GPBE

Unlike C and F, S changes the added mass, momentum, and internal energy of the particles due to exchanges with the fluid phase; however, it does not change $n(\xi)$. The integral constraints, similar to those introduced in [6] for monodisperse particles, are thus

$$\int \xi S \, \mathrm{d}\xi = S(\mathbf{u}, e) \tag{18}$$

and

$$\int \xi S \, \mathrm{d}\xi \, \mathrm{d}\mathbf{u} \, \mathrm{d}e = S_a, \quad \int \xi e S \, \mathrm{d}\xi \, \mathrm{d}\mathbf{u} \, \mathrm{d}e = S_e, \quad \int \xi \mathbf{u} S \, \mathrm{d}\xi \, \mathrm{d}\mathbf{u} \, \mathrm{d}e = \mathbf{S}_{fp}, \quad \int \xi \frac{1}{2} u^2 S \, \mathrm{d}\xi \, \mathrm{d}\mathbf{u} \, \mathrm{d}e = S_K \tag{19}$$

where the right-hand sides $(S_a, S_e, \mathbf{S}_{fp}, S_K)$ are given in table 2. The simplest model for S that satisfies these constraints, while keeping the particle size distribution unchanged, is

$$S = C_\xi f + C_u \frac{\partial}{\partial e}[(e - e_f) f] + C_u \frac{\partial}{\partial \mathbf{u}} \cdot [(\mathbf{u} - \mathbf{u}_f) f] + \frac{1}{2} C_u \frac{\partial^2}{\partial \mathbf{u} \partial \mathbf{u}} : [\mathbf{D}_u f] \tag{20}$$

where the parameters (C_ξ, C_u) are the same as in table 2. The velocity diffusion matrix is defined by

$$\mathbf{D}_u = (\mathbf{u} - \mathbf{u}_f) \otimes (\mathbf{u} - \mathbf{u}_f) + \frac{2}{3} k_f \mathbf{I} \tag{21}$$

where the final term represents an isotropic model for the PTKE Reynolds stresses [6]. In the polydisperse two-fluid model, only the trace of $\mathbf{D}_u$ will be needed to determine $\mathcal{K}_s$:

$$\int tr(\mathbf{D}_u) p(\mathbf{u}|\xi) \, \mathrm{d}\mathbf{u} = 3\Theta_p(\xi) + (\mathbf{u}_p(\xi) - \mathbf{u}_f)^2 + 2k_f. \tag{22}$$

Aside from the definition of f, eq. (20) is the same as for the monodisperse case in [6].

In the moment equations that include the particle mass, we will need closed expressions for the following integrals:[6]

$$\mathcal{S}_s^0 = \int \xi^s S \, \mathrm{d}\xi \, \mathrm{d}\mathbf{u} \, \mathrm{d}e = \int \xi^s C_\xi f \, \mathrm{d}\xi \, \mathrm{d}\mathbf{u} \, \mathrm{d}e, \tag{23}$$

$$\mathcal{S}_s^e = \int \xi^s e S \, \mathrm{d}\xi \, \mathrm{d}\mathbf{u} \, \mathrm{d}e = \int \xi^s e \left(C_\xi f + C_u \frac{\partial}{\partial e}[(e - e_f) f] \right) \mathrm{d}\xi \, \mathrm{d}\mathbf{u} \, \mathrm{d}e, \tag{24}$$

$$\boldsymbol{\mathcal{S}}_s^1 = \int \xi^s \mathbf{u} S \, \mathrm{d}\xi \, \mathrm{d}\mathbf{u} \, \mathrm{d}e = \int \xi^s \mathbf{u} \left(C_\xi f + C_u \frac{\partial}{\partial \mathbf{u}} \cdot [(\mathbf{u} - \mathbf{u}_f) f] \right) \mathrm{d}\xi \, \mathrm{d}\mathbf{u} \, \mathrm{d}e, \tag{25}$$

and (including the factor of 1/2 in $\mathcal{K}_s$)

$$\mathcal{S}_s^2 = \int \xi^s \frac{1}{2} u^2 S \, \mathrm{d}\xi \, \mathrm{d}\mathbf{u} \, \mathrm{d}e = \int \xi^s \frac{1}{2} u^2 \left(C_\xi f + C_u \frac{\partial}{\partial \mathbf{u}} \cdot [(\mathbf{u} - \mathbf{u}_f) f] + \frac{1}{2} C_u \frac{\partial^2}{\partial \mathbf{u} \partial \mathbf{u}} : [\mathbf{D}_u f] \right) \mathrm{d}\xi \, \mathrm{d}\mathbf{u} \, \mathrm{d}e \tag{26}$$

for $0 \leq s$. Applying integration by parts yields the definitions of the added-mass source terms:

$$\begin{gathered} \mathcal{S}_s^0 = C_\xi \mathcal{M}_s, \quad \mathcal{S}_s^e = (C_\xi - C_u) \mathcal{E}_s + C_u \mathcal{M}_s e_f, \\ \boldsymbol{\mathcal{S}}_s^1 = (C_\xi - C_u) \boldsymbol{\mathcal{U}}_s^1 + C_u \mathcal{M}_s \mathbf{u}_f, \quad \mathcal{S}_s^2 = (C_\xi - C_u) \mathcal{K}_s + C_u \mathcal{M}_s K_f \end{gathered} \tag{27}$$

[6] For clarity, in the final form on the right-hand side found by inserting eq. (20), only the non-zero parts are retained.

where $\mathcal{S}_s^0$, $\mathcal{S}_s^e$, and $\mathcal{S}_s^2$ are scalars and $\boldsymbol{\mathcal{S}}_s^1$ is a vector. For $s = 1$, these results satisfy eq. (19). Note that the definition of $\mathcal{S}_s^0$ is applicable to non-integer values of s.

3.5. Particular limiting cases

For monodisperse particles with mass ξ_1 and number concentration n_1, the NDF reduces to $f = g_1(\mathbf{u}, e)\beta n_1 \delta(\xi - \xi_1)$ where $\delta(\xi)$ is the Dirac delta function. Integrating eq. (11) over ξ-space yields the kinetic equation for $g(\mathbf{u}, e)$. More generally, a binary system with fixed (unequal) masses ξ_1 and ξ_2 has

$$f = g_1(\mathbf{u}, e)\beta n_1 \delta(\xi - \xi_1) + g_2(\mathbf{u}, e)\beta n_2 \delta(\xi - \xi_2). \tag{28}$$

Thus, integration over mass phase space yields two coupled kinetic equations. More generally, n_i with fixed ξ_i can be found from N mass moments [22]:

$$\mathcal{M}_s = \int \xi^s f \, \mathrm{d}\xi \, \mathrm{d}\mathbf{u} \, \mathrm{d}e = \sum_{i=1}^{N} \beta n_i \xi_i^s \quad \text{for } s = 0, 1, \ldots, N-1; \tag{29}$$

so that solving for moments is equivalent to solving N kinetic equations. The binary case is a difficult numerical test case for moment methods [19]. During spatial transport of the moments, the masses must remain constant, which will be true only if the numerical fluxes are correctly defined. Consistent with our treatment of the monodisperse case, the conditional velocity distribution function will be assumed to be Maxwellian, but with a different mean velocity $\mathbf{u}_p(\xi)$, granular temperature $\Theta_p(\xi)$, and internal energy $e_p(\xi)$ for each mass ξ.

3.6. Definition of particle-phase moments needed for spatial fluxes

In section 3.1, we have defined some of the particle-phase moments needed to derive mass, momentum, and energy balances from eq. (11). In addition, to compute the spatial fluxes, we will need the following moments for $i + j + k = l$ with orders $l = 1, 2, 3$ and $s \geq 0$:

$$\boldsymbol{\mathcal{U}}_s^e = \int \xi^s e \mathbf{u} \, f(\xi, \mathbf{u}, e) \, \mathrm{d}\xi \, \mathrm{d}\mathbf{u} \, \mathrm{d}e, \quad \mathcal{U}_{s,i,j,k}^l = \int \xi^s u^i v^j w^k \, f(\xi, \mathbf{u}) \, \mathrm{d}\xi \, \mathrm{d}\mathbf{u}. \tag{30}$$

In words, the vector $\boldsymbol{\mathcal{U}}_s^1 = (\mathcal{U}_{s,1,0,0}^1, \mathcal{U}_{s,0,1,0}^1, \mathcal{U}_{s,0,0,1}^1)^t$ is the ξ^s-mass-weighted flux of number concentration, $\boldsymbol{\mathcal{U}}_s^e$ is the ξ^s-mass-weighted flux of internal energy, $\boldsymbol{\mathcal{U}}_{s,i,j,k}^2$ are the components of the ξ^s-mass-weighted kinetic-energy tensor, and $\boldsymbol{\mathcal{U}}_{s,i,j,k}^3$ yields the ξ^s-mass-weighted flux of kinetic energy. In the polydisperse model, the set of mass-weighted moments in eq. (10) are the conserved variables, and their spatial fluxes depend on the moments in eq. (30).

For polydisperse particles, the quadrature-based reconstruction developed in section 4 uses $s = 0, 1, 2, 3$. By construction, the mixture mass, momentum and total energy defined, respectively, by $\rho_f \alpha_f^\star + \mathcal{M}_1$, $\rho_f \alpha_f^\star \mathbf{u}_f + \mathcal{M}_1 \boldsymbol{\mathcal{U}}_1^1$, and $\rho_f \alpha_f^\star E_f + \mathcal{M}_1 E_p$, are conserved quantities. When the particle mass NDF does not change (as is the case with inert particles), we shall see that the source terms in the transport equations are most easily evaluated using the mass-conditioned moments introduced in section 4. In general, operator splitting can be employed to separate source terms into two groups: those that do and do not change $n(\xi)$. Specifically adapted numerical methods are then used for each group to ensure that the moments remain realizable at every time step [22].

3.7. Transport equations for the particle-phase moments

Using integration over phase space, the GPBE in eq. (11) yields the generic transport equations for the mass-weighted moments in eq. (10). The derivation methodology follows exactly as is done for monodisperse particles in [6], the only difference being the integration over mass phase space. Thus, in the following, we provide only the final expressions without the intermediate mathematical steps. For the mass moments, the resulting governing equation is

$$\partial_t \mathcal{M}_s + \partial_{\mathbf{x}} \cdot \boldsymbol{\mathcal{U}}_s^1 = \mathcal{S}_s^0 \tag{31}$$

where exponent s can take on non-negative values. Similarly, the internal-energy moments are governed by

$$\partial_t \mathcal{E}_s + \partial_{\mathbf{x}} \cdot \boldsymbol{\mathcal{U}}^e_s = \mathcal{A}^e_s - \frac{1}{2}\mathcal{C}^2_s - \frac{1}{2}\mathcal{F}^2_s + \mathcal{S}^e_s \tag{32}$$

with

$$\mathcal{A}^e_s = \beta \int \xi^s A_e(\xi)\, n(\xi)\, \mathrm{d}\xi, \quad A_e(\xi) = \frac{6\lambda_f Nu}{\rho_e d_p^2(\xi)}[T_f - T_p(\xi)], \tag{33}$$

and where $\mathcal{C}^2_s + \mathcal{F}^2_s \leq 0$ is the kinetic energy lost due to inelastic particle–particle contacts (see Appendix A). The final terms on the right-hand sides of eqs. (31) and (32) are due to added-mass exchange, and $\mathcal{A}^e_s$ represents heat transfer from the fluid phase. Here, the conditional particle temperature $T_p(\xi)$ is computed from the corresponding conditional internal energy $e_p(\xi)$ found as described in section 4. The standard Nusselt number Nu (see table 2) depends on the particle Reynolds number Re_p, but not on a particle Reynolds number based on the RMS velocity $Re_\theta = d_p \Theta_p^{1/2}/\nu_f$. In cases where $Re_p \ll Re_\theta$, this Nu definition will likely underestimate the heat-transfer rate.

It is important to note that for a particle phase with $\alpha_p > \alpha_{max}$ (i.e., under close-packed conditions) conductive heat transfer between particles with different sizes can be significant and, therefore, should be accounted for in the polydisperse model. In practice, this would be modeled by an additional term on the right-hand size of eq. (32) that causes the mass-conditioned internal energies to reach equilibrium while keeping $\mathcal{E}_1$ constant, e.g.,

$$\mathcal{A}^p_s = \beta \int \xi^s A^p_e(\xi)\, n(\xi)\, \mathrm{d}\xi, \quad A^p_e(\xi) = \int h(\xi,\zeta)[T_p(\zeta) - T_p(\xi)]\, \alpha(\zeta)\, \mathrm{d}\zeta \tag{34}$$

where $h(\xi,\zeta) = h(\zeta,\xi)$ is a size-dependent heat-transfer coefficient that must be specified [3]. Such a term corresponds to particle–particle heat transfer between particles in sustained contact with different temperatures.

For the mass–velocity moments (in Cartesian coordinates), the first-order governing equations are

$$\begin{aligned}
\partial_t \mathcal{U}^1_{s,1,0,0} + \partial_x(\mathcal{U}^2_{s,2,0,0} + \mathcal{M}_s P_p) + \partial_y \mathcal{U}^2_{s,1,1,0} + \partial_z \mathcal{U}^2_{s,1,0,1} &= -\frac{\mathcal{M}_s}{\rho_e}(\partial_x \hat{p}_f + F_{pf,x}) - \frac{\mathcal{M}_s}{\rho_e \alpha^\star_p}(\partial_{\mathbf{x}} \cdot \mathbf{P}_{pfp})_x \\
&\quad - \mathcal{A}^1_{s,1,0,0} + \mathcal{C}^1_{s,1,0,0} + \mathcal{F}^1_{s,1,0,0} + \mathcal{S}^1_{s,1,0,0}, \\
\partial_t \mathcal{U}^1_{s,0,1,0} + \partial_x \mathcal{U}^2_{s,1,1,0} + \partial_y(\mathcal{U}^2_{s,0,2,0} + \mathcal{M}_s P_p) + \partial_z \mathcal{U}^2_{s,0,1,1} &= -\frac{\mathcal{M}_s}{\rho_e}(\partial_y \hat{p}_f + F_{pf,y}) - \frac{\mathcal{M}_s}{\rho_e \alpha^\star_p}(\partial_y \cdot \mathbf{P}_{pfp})_y \\
&\quad - \mathcal{A}^1_{s,0,1,0} + \mathcal{C}^1_{s,0,1,0} + \mathcal{F}^1_{s,0,1,0} + \mathcal{S}^1_{s,0,1,0}, \\
\partial_t \mathcal{U}^1_{s,0,0,1} + \partial_x \mathcal{U}^2_{s,1,0,1} + \partial_y \mathcal{U}^2_{s,0,1,1} + \partial_z(\mathcal{U}^2_{s,0,0,2} + \mathcal{M}_s P_p) &= -\frac{\mathcal{M}_s}{\rho_e}(\partial_z \hat{p}_f + F_{pf,z}) - \frac{\mathcal{M}_s}{\rho_e \alpha^\star_p}(\partial_y \cdot \mathbf{P}_{pfp})_z \\
&\quad - \mathcal{A}^1_{s,0,0,1} + \mathcal{C}^1_{s,0,0,1} + \mathcal{F}^1_{s,0,0,1} + \mathcal{S}^1_{s,0,0,1},
\end{aligned} \tag{35}$$

and (for kinetic energy)

$$\partial_t \mathcal{K}_s + \partial_{\mathbf{x}} \cdot (\mathcal{U}^3_s + \boldsymbol{\mathcal{U}}^1_s P_p) = -\frac{1}{\rho_e}\boldsymbol{\mathcal{U}}^1_s \cdot (\partial_{\mathbf{x}} \hat{p}_f + \mathbf{F}_{pf}) - \frac{1}{\rho_e \alpha^\star_p}\boldsymbol{\mathcal{U}}^1_s \cdot (\partial_{\mathbf{x}} \cdot \mathbf{P}_{pfp}) - \mathcal{A}^2_s + \mathcal{B}^2_s + \frac{1}{2}\mathcal{C}^2_s + \frac{1}{2}\mathcal{F}^2_s + \mathcal{S}^2_s \tag{36}$$

where $2\mathcal{K}_s = \mathcal{U}^2_{s,2,0,0} + \mathcal{U}^2_{s,0,2,0} + \mathcal{U}^2_{s,0,0,2}$, and $\mathcal{U}^3_s$ is the free-transport spatial flux of kinetic energy. These equations have the same mathematical structure as in the monodisperse case. The only difference is the dependence on s, whereas for monodisperse particles we have $s = 1$. Physically, with $s = 1$, eq. (31) represents a mass balance, eq. (32) an internal-energy balance, eq. (35) a momentum balance, and eq. (36) a kinetic-energy balance. Additional values of s are required to account for polydispersity. Notice that these balance equations are not yet closed. For example, we must provide a closure for the free-transport momentum flux $\mathcal{U}^2_{s,i,j,k}$ in terms of the conserved variables $(\mathcal{M}_s, \boldsymbol{\mathcal{U}}^1_s, \mathcal{K}_s, \mathcal{E}_s)$.

3.8. Definition of fluxes and source terms in the moment transport equations

The governing equations for the moments have spatial fluxes and source terms that depend on the underlying physics. The particle-phase pressure is again modeled by $P_p = P_c + P_{fr}$ where the collisional and frictional pressures are given in table 2. The acceleration source term from the fluid-phase drag has the monodisperse form, but averaged over the sizes. For example, the fluid-drag vector for the mean velocity is

$$\mathcal{A}_s^1 = \beta \int \xi^s \frac{1}{\tau_p(\xi)} [\mathbf{u}_p(\xi) - \mathbf{u}_f]\, n(\xi)\, \mathrm{d}\xi \quad \text{with} \quad \tau_p(\xi) = \frac{4\rho_e d_p^2(\xi)}{3\mu_f C_D(\xi)\, Re_p(\xi)}. \tag{37}$$

$Re_p(\xi)$ is the particle Reynolds number for particles with mass ξ and $C_D(\xi)$ is the corresponding drag coefficient. In this work, we will mainly consider very small particles near the Stokes regime where $C_D(\xi)\, Re_p(\xi) = 24$. Thus, $\tau_p(\xi) \propto \xi^{2/3}$. Nonetheless, any appropriate model for the drag coefficient can be easily accommodated [24].

The multi-component frictional source terms are

$$\mathcal{F}_s^1 = \frac{1}{\tau_{fr}}(\mathcal{M}_s \mathbf{u}_p - \boldsymbol{\mathcal{U}}_s^1), \quad \mathcal{F}_s^2 = \frac{1}{\tau_{fr}}(\mathcal{M}_s u_p^2 - 2\mathcal{K}_s). \tag{38}$$

Due to conservation of momentum, we have $\mathcal{F}_1^1 = 0$. Momentum and energy exchange between particles of different sizes are captured by $\mathcal{F}_s^1$ and $\mathcal{F}_s^2$, respectively. In addition, friction results in a loss of total granular energy ($\mathcal{F}_1^2 < 0$), which is transferred to internal energy (see Appendix C.5 for details).

The multi-component particle–particle collision term can be written as (see Appendix A for details)

$$C_s^1 = \beta \int \xi^s C^1(\xi)\, n(\xi)\, \mathrm{d}\xi, \quad C_s^2 = \beta \int \xi^s C^2(\xi)\, n(\xi)\, \mathrm{d}\xi \tag{39}$$

with

$$C^1(\xi) = \int \frac{\eta\alpha(\zeta)}{2\tau_c(\xi,\zeta)} [\mathbf{u}_p(\zeta) - \mathbf{u}_p(\xi)]\, \mathrm{d}\zeta \tag{40}$$

and

$$C^2(\xi) = \int \frac{\eta\alpha(\zeta)}{2\tau_c(\xi,\zeta)} \left[\Theta_p(\xi) - \frac{\eta\mu_{\xi,\zeta}}{2} E(\xi,\zeta) + \mathbf{u}_p(\xi) \cdot (\mathbf{u}_p(\xi) - \mathbf{u}_p(\zeta))\right] \mathrm{d}\zeta. \tag{41}$$

The collision timescale[7] is

$$\tau_c(\xi,\zeta) := \frac{[d_p(\zeta) + d_p(\xi)]\sqrt{2\pi}}{12 g_0(\xi,\zeta)\, \mathcal{V}_{\xi,\zeta} \sqrt{E(\xi,\zeta)}}. \tag{42}$$

The volume fraction of particles with mass ζ is related to the NDF by

$$\alpha(\zeta) = \frac{\zeta}{\rho_p} n(\zeta). \tag{43}$$

The particle–particle collision restitution coefficient e_c, and hence $\eta = \frac{1}{2}(1 + e_c)$, are assumed to be independent of particle size. The hard-sphere collision parameters are[8] [10]

$$\mathcal{V}_{\xi,\zeta} = \frac{[d_p(\zeta) + d_p(\xi)]^3}{d_p^3(\xi) + d_p^3(\zeta)}, \quad \mu_{\xi,\zeta} = \frac{2 d_p^3(\zeta)}{d_p^3(\xi) + d_p^3(\zeta)}, \tag{44}$$

and the energy function is

$$E(\xi,\zeta) = \Theta_p(\xi) + \Theta_p(\zeta) + \frac{1}{3}[\mathbf{u}_p(\xi) - \mathbf{u}_p(\zeta)]^2. \tag{45}$$

[7] For the monodisperse case, τ_c include the volume fraction of collision partners α_p. Here, this volume fraction is $\alpha(\zeta)$ in eq. (41). The factor of 2 multiplying π comes from the definition of E in eq. (45).

[8] These parameters are defined for particles with the same density ρ_p. More generally, collisions between particles with different densities can be easily accommodated (e.g., the definition of $\mu_{\xi,\zeta}$ uses the particle masses instead of the volumes).

The radial distribution function for polydisperse particles is [26]

$$g_0(\xi,\zeta) = \frac{1}{\alpha_f} + \left(g_0(\alpha_f) - \frac{1}{\alpha_f}\right)\frac{\langle d_p^2\rangle}{\langle d_p^3\rangle}\frac{2d_p(\xi)d_p(\zeta)}{d_p(\xi)+d_p(\zeta)} \tag{46}$$

where $\langle d_p^n\rangle = \int d_p^n(\xi)\, n(\xi)\,\mathrm{d}\xi$ is the number-averaged value of $d_p^n(\xi)$. For monodisperse particles, this formula reduces to g_0.

Due to conservation of momentum, $C_1^1 = 0$. For elastic collisions ($\eta = \frac{1}{2}(1+e_c) = 1$), the collision term $C_1^2 = 0$ due to conservation of energy. Otherwise, particle–particle collisions result in a loss of total granular energy ($C_1^2 < 0$), which is transferred to internal energy. By applying QBMM (see section 4), the integrals over mass phase space will become weighted sums over mass abscissae. Thus, eq. (39) yields a double summation over all possible binary collision partners.

3.9. Transport equations for polydisperse granular flow: Final form

The moment-conservation equations written in tensor notation that will be used in this work to describe a polydisperse flow are summarized in table 4. For the mass moments, we have eq. (31). Likewise, for internal energy, we have eq. (32), and for kinetic energy eq. (36). Finally, the velocity moments are governed by

$$\partial_t \boldsymbol{\mathcal{U}}_s^1 + \partial_{\mathbf{x}}\cdot(\boldsymbol{\mathcal{U}}_s^2 + \mathcal{M}_s P_p \mathbf{I}) = -\frac{\mathcal{M}_s}{\rho_e}(\partial_{\mathbf{x}}\hat{p}_f + \mathbf{F}_{pf}) - \frac{\mathcal{M}_s}{\rho_e \alpha_p^\star}(\partial_{\mathbf{x}}\cdot\mathbf{P}_{pfp}) - \mathcal{A}_s^1 + C_s^1 + \mathcal{F}_s^1 + \boldsymbol{\mathcal{S}}_s^1 \tag{47}$$

where $\boldsymbol{\mathcal{U}}_s^2$ is the (unclosed) second-order velocity covariance tensor. With $s = 1$, the four equations found from eqs. (31), (32) and (47) + (36) correspond, respectively, to mass, momentum and total energy.

As described in the next section, quadrature-based moment methods (QBMM) are used to close the integrals appearing in the definitions of the source terms, and to define $\boldsymbol{\mathcal{U}}_s^1$ for non-integer values of s. As done in the monodisperse case [6], HyQMOM [11] is applied to the mass-conditioned velocity moments to close the flux vector $\boldsymbol{\mathcal{U}}_s^3$ in eq. (36), and $\boldsymbol{\mathcal{U}}_s^2$ in eq. (47) by assuming that the mass-conditioned velocity moments are Maxwellian. The particle-phase governing equations correspond to Euler equations (left-hand side) for each value of s coupled with the fluid phase and other values of s (right-hand side). It is important to keep in mind that the closures used for the velocity moments require that the particle-phase volume fraction be large enough to allow for significant particle–particle collisions. If this is not the case, then higher-order velocity moments will be needed to accurately model the spatial fluxes [13].

At this point, the system of conservation equations that must be solved to describe polydisperse, high-speed, fluid–particle flows is complete. However, in order to formulate a numerical method to solve them, we must provide a robust algorithm to find mass-conditioned moments from the conserved moments.

4. Quadrature-based moment methods

The transport equations for the particle-phase moments have the form of nonlinear hyperbolic conservation laws [28]. Due to the non-linearity, care must be taken to ensure that the moments remain realizable when solving the system numerically. For polydisperse particles, a powerful approach for ensuring realizability is to design numerical algorithms using QBMM [22]. In the following, we provide an overview of QBMM that specifically addresses the salient points arising for polydisperse fluid–particle flows. A more comprehensive discussion can be found in [22]. In Appendix F, we provide an extension of QBMM to allow for the number of mass quadrature points (N_g) to be larger than the number of mass-conditioned velocities (N). This extension may be useful for cases where the mass NDF has a complex shape requiring large N_g [22], but the coupling with velocity requires only a small value for N (e.g., fine particles with small Stokes number require only $N = 1$).

4.1. Overview of QBMM

In the previous section, we derived unclosed transport equations for the conserved variables for the particle phase (see table 4): $\mathcal{M}_s$, $\boldsymbol{\mathcal{U}}_s^1$, $\mathcal{K}_s$, and $\mathcal{E}_s$. In order to close the spatial fluxes and source terms (see table 5), we must associate

Table 4: Polydisperse model for high-speed fluid–particle flow with added mass, internal energy, and PTKE. See tables 2 and 5 for definitions of the model parameters. For $s = 1$, conservation of mass, momentum and total energy (where $\mathcal{M}_1 = \rho_e \alpha_p^\star$, $\boldsymbol{\mathcal{U}}_1^1 = \rho_e \alpha_p^\star \mathbf{u}_p$, and $\mathcal{U}_1^2 = \rho_e \alpha_p^\star K_p$) for the sum of the two phases defines the exchange terms. The free-transport spatial fluxes for the particle phase are computed using QBMM as described in section 4. The collisional/frictional terms are discussed in detail in Appendix C. The particle-phase balances are written with the fluxes on the left and the sources on the right and gravity $\mathbf{g}$ is included for completeness. Finally, note that α_p is used in place of β to define the added mass.

Mass balances:

$$\partial_t \alpha_p + \partial_{\mathbf{x}} \cdot \alpha_p \mathbf{u}_p = 0$$
$$\partial_t \rho_f \alpha_f^\star + \partial_{\mathbf{x}} \cdot \rho_f \alpha_f^\star \mathbf{u}_f = -\mathcal{S}_1^0$$
$$\partial_t \mathcal{M}_s + \partial_{\mathbf{x}} \cdot \boldsymbol{\mathcal{U}}_s^1 = \mathcal{S}_s^0$$

Momentum balances:

$$\partial_t \rho_f \alpha_f^\star \mathbf{u}_f + \partial_{\mathbf{x}} \cdot (\rho_f \alpha_f^\star \mathbf{u}_f \mathbf{u}_f + \hat{p}_f \mathbf{I}) = \alpha_p^\star (\partial_{\mathbf{x}} \hat{p}_f + \mathbf{F}_{pf}) + \boldsymbol{\mathcal{A}}_1^1 - \boldsymbol{\mathcal{S}}_1^1 + \rho_f \alpha_f^\star \mathbf{g}$$
$$\partial_t \boldsymbol{\mathcal{U}}_s^1 + \partial_{\mathbf{x}} \cdot (\boldsymbol{\mathcal{U}}_s^2 + \mathcal{M}_s P_p \mathbf{I}) = -\frac{\mathcal{M}_s}{\mathcal{M}_1} [\partial_{\mathbf{x}} \cdot \mathbf{P}_{pfp} + \alpha_p^\star (\partial_{\mathbf{x}} \hat{p}_f + \mathbf{F}_{pf})] - \boldsymbol{\mathcal{A}}_s^1 + \boldsymbol{\mathcal{C}}_s^1 + \boldsymbol{\mathcal{F}}_s^1 + \boldsymbol{\mathcal{S}}_s^1 + \mathcal{M}_s \mathbf{g}$$

Fluid-phase energy balances (total and PTKE):

$$\partial_t \rho_f \alpha_f^\star E_f + \partial_{\mathbf{x}} \cdot [\rho_f \alpha_f^\star \mathbf{u}_f E_f + (\alpha_f^\star \mathbf{u}_f + \alpha_p^\star \mathbf{u}_p) \hat{p}_f + \mathbf{P}_{pfp} \cdot \mathbf{u}_p] = \mathbf{u}_p \cdot [\partial_{\mathbf{x}} \cdot \mathbf{P}_{pfp} + \alpha_p^\star (\partial_{\mathbf{x}} \hat{p}_f + \mathbf{F}_{pf})]$$
$$+ \mathcal{A}_1^2 - (1-a)\mathcal{B}_1^2 - \mathcal{A}_1^e - \mathcal{S}_1^2 - \mathcal{S}_1^e + \rho_f \alpha_f^\star \mathbf{u}_f \cdot \mathbf{g}$$
$$\partial_t \rho_f \alpha_f^\star k_f + \partial_{\mathbf{x}} \cdot \rho_f \alpha_f^\star \mathbf{u}_f k_f + \frac{2}{3} \rho_f \alpha_f^\star k_f \partial_{\mathbf{x}} \cdot \mathbf{u}_f = \mathcal{A}_1^f - (2 - 2a + C_g)\, \mathcal{B}_1^f\, k_f$$

Particle-phase energy balances (kinetic and internal):

$$\partial_t \mathcal{K}_s + \partial_{\mathbf{x}} \cdot (\boldsymbol{\mathcal{U}}_s^3 + \boldsymbol{\mathcal{U}}_s^1 P_p) = -\frac{\boldsymbol{\mathcal{U}}_s^1}{\mathcal{M}_1} \cdot [\partial_{\mathbf{x}} \cdot \mathbf{P}_{pfp} + \alpha_p^\star (\partial_{\mathbf{x}} \hat{p}_f + \mathbf{F}_{pf})] - \boldsymbol{\mathcal{A}}_s^2 + (1-a)\boldsymbol{\mathcal{B}}_s^2 + \frac{1}{2}\boldsymbol{\mathcal{C}}_s^2 + \frac{1}{2}\boldsymbol{\mathcal{F}}_s^2 + \boldsymbol{\mathcal{S}}_s^2 + \boldsymbol{\mathcal{U}}_s^1 \cdot \mathbf{g}$$
$$\partial_t \mathcal{E}_s + \partial_{\mathbf{x}} \cdot \boldsymbol{\mathcal{U}}_s^e = \mathcal{A}_s^e - \frac{1}{2}\mathcal{C}_s^2 - \frac{1}{2}\mathcal{F}_s^2 + \mathcal{S}_s^e$$

Table 5: Terms in the polydisperse model for high-speed, fluid–particle flow in table 4. All other terms are in table 2 and $C_\xi = S_a / \mathcal{M}_1$. $\mathbf{u}_p(\xi)$, $K_p(\xi)$, and $\Theta_p(\xi)$ are the velocity moments conditioned on mass ξ, and $e_p(\xi)$ and $T_p(\xi)$ are the mass-conditioned internal energy and the corresponding thermodynamic temperature. Source terms and spatial fluxes are closed using GQMOM with N weights w_β and N mass abscissae ξ_β.

$$\mathcal{S}_s^0 = C_\xi \mathcal{M}_s \quad \boldsymbol{\mathcal{S}}_s^1 = C_u \mathcal{M}_s \mathbf{u}_f + (C_\xi - C_u)\boldsymbol{\mathcal{U}}_s^1 \quad \mathcal{S}_s^2 = C_u \mathcal{M}_s K_f + (C_\xi - C_u)\mathcal{K}_s \quad \mathcal{S}_s^e = C_u \mathcal{M}_s e_f + (C_\xi - C_u)\mathcal{E}_s$$

$$\boldsymbol{\mathcal{A}}_s^1 = \sum_{\beta=1}^N w_\beta \xi_\beta^s \frac{1}{\tau_p(\xi_\beta)} [\mathbf{u}_p(\xi_\beta) - \mathbf{u}_f] \qquad \mathcal{A}_s^2 = \sum_{\beta=1}^N w_\beta \xi_\beta^s \frac{1}{\tau_p(\xi_\beta)} [3\Theta_p(\xi_\beta) + (\mathbf{u}_p(\xi_\beta) - \mathbf{u}_f) \cdot \mathbf{u}_p(\xi_\beta)]$$

$$\mathcal{A}_s^f = \sum_{\beta=1}^N w_\beta \xi_\beta^s \frac{1}{\tau_p(\xi_\beta)} [3a\Theta_p(\xi_\beta) + (\mathbf{u}_p(\xi_\beta) - \mathbf{u}_f)^2] \qquad \mathcal{A}_s^e = \sum_{\beta=1}^N w_\beta \xi_\beta^s \frac{6\lambda_f Nu}{\rho_e d_p^2(\xi_\beta)} [T_f - T_p(\xi_\beta)]$$

$$\mathcal{B}_s^f = \sum_{\beta=1}^N w_\beta \xi_\beta^s \frac{1}{\tau_p(\xi_\beta)} \qquad \mathcal{B}_s^2 = \sum_{\beta=1}^N w_\beta \xi_\beta^s \frac{1}{\tau_p(\xi_\beta)} [3\Theta_p(\xi_\beta) + 2k_f] \qquad \boldsymbol{\mathcal{U}}_{s/3}^1 = \sum_{\beta=1}^N w_\beta \xi_\beta^{s/3} \mathbf{u}_p(\xi_\beta)$$

$$\boldsymbol{\mathcal{U}}_s^2 = \sum_{\beta=1}^N w_\beta \xi_\beta^s [\mathbf{u}_p(\xi_\beta) \otimes \mathbf{u}_p(\xi_\beta) + \Theta_p(\xi_\beta)\mathbf{I}] \quad \boldsymbol{\mathcal{U}}_s^3 = \sum_{\beta=1}^N w_\beta \xi_\beta^s [K_p(\xi_\beta) + \Theta_p(\xi_\beta)] \mathbf{u}_p(\xi_\beta) \quad \boldsymbol{\mathcal{U}}_s^e = \sum_{\beta=1}^N w_\beta \xi_\beta^s e_p(\xi_\beta) \mathbf{u}_p(\xi_\beta)$$

a distribution function to a given set of mass moments (i.e., given choices for s). In QBMM, this is accomplished using the generalized quadrature method of moments (GQMOM) such that the mass NDF is approximated by a summation of $N \geq 1$ Dirac delta functions [12]:

$$\beta\, n(\xi) \approx \sum_{\beta=1}^{N} w_\beta \delta(\xi - \xi_\beta) \tag{48}$$

with mass abscissae ξ_β and number concentrations w_β. The mass moments $\mathcal{M}_s$ are related to the weights and abscissae by

$$\mathcal{M}_s = \sum_{\beta=1}^{N} w_\beta \xi_\beta^s, \quad s \in (0, 1, \ldots, N_s) \tag{49}$$

where $N_s \leq 2N - 1$ fixes the number of moments required for the polydisperse model: $(\mathcal{M}_0, \mathcal{M}_1, \ldots, \mathcal{M}_{N_s})$. Given these moments, w_β and ξ_β are found using a moment-inversion algorithm [12, 15]. By definition, Gaussian quadrature weights are always non-negative if the moments used to construct them are realizable [15, 16]. Except in degenerate cases where the moments correspond to a mass NDF composed of less than N Dirac delta functions, the abscissae are distinct and the weights positive. In the degenerate case, some weights are zero.

The value of N in eq. (48) fixes the number of particle types used to represent the mass NDF. As we will show below in section 4.2, it also fixes the number of momentum and energy balances that must be solved. Based on accumulated experience with QBMM, a value of $N = 3$ or $N = 4$ usually suffices [22]. Variations of GQMOM wherein one of the abscissae is fixed (i.e., Gauss–Radau quadrature) are also available [12]. For example, very small particles can be treated as following the fluid with zero slip (i.e., $\mathbf{u}_p(\xi_0) = \mathbf{u}_f$), and hence we can assign them to have mass $\xi_0 = 0$ with concentration w_0 (i.e., the dusty gas model).

For solid particles, it is often preferable to use the particle-size NDF instead of the mass NDF, which makes use of non-integer moments:

$$\mathcal{M}_{s/3} = \sum_{\beta=1}^{N} w_\beta \xi_\beta^{s/3}, \quad s \in (0, 1, \ldots, N_s). \tag{50}$$

Another viable option is to use an NDF with half-order moments

$$\mathcal{M}_{s/2} = \sum_{\beta=1}^{N} w_\beta \xi_\beta^{s/2}, \quad s \in (0, 1, \ldots, N_s). \tag{51}$$

Note that when non-integer mass moments are used, the weights and abscissae will usually be different than those in eq. (49). However, the procedure in section 4.2 for finding the mass-conditioned moments is exactly the same. For clarity, the mass abscissae for the size moments are defined by $\xi_\beta = \zeta_\beta^3$ where the ζ_β satisfy

$$\mathcal{M}_{s/3} = \sum_{\beta=1}^{N} w_\beta \zeta_\beta^s, \quad s \in (0, 1, \ldots, N_s), \tag{52}$$

and for half-order moments as $\xi_\beta = \varsigma_\beta^2$. The units of ζ_β and ς_β are $\mathrm{kg}^{1/3}$ and $\mathrm{kg}^{1/2}$, respectively. Generally speaking, the moment-inversion algorithm (which returns ζ_β or ς_β, depending on the input moment set) is better conditioned when size moments are used. This is because the higher-order mass moments depend strongly on the tail of the mass NDF (i.e., very heavy particles), which usually represents a very small fraction of the total mass. Nonetheless, to satisfy mass conservation, the mass moment $\mathcal{M}_1$ must always be included as a conserved variable. Thus, size moments are used only when $N_s \geq 3$, and half-order moments when $N_s \geq 2$.

With GQMOM, the unknown higher-order moments (e.g., $\mathcal{M}_s$ with $s > N_s$) are fitted to a particular distribution function (e.g., lognormal, gamma, beta). In our numerical implementation, we use either beta-GQMOM or lognormal-GQMOM with $N = 4$ to approximate the unclosed terms in the particle-phase transport equation. The half-order-moment set for $N_s = 6$ is thus $(\mathcal{M}_0, \mathcal{M}_{1/2}, \mathcal{M}_1, \mathcal{M}_{3/2}, \mathcal{M}_2, \mathcal{M}_{5/2}, \mathcal{M}_3)$, which can capture an NDF with three modes [12]. This choice of N and N_s, and use of the half-order moments, is motivated by the definition of the mass-conditioned moments described in section 4.2. There we show that $N_s = 2(N - 1)$ with half-order moments provides

consistency with the orders of the mass-weighted velocity and energy moments. Nonetheless, using a smaller N_s with mass moments is also an option when the mass NDF is known *a priori* to be uni-modal.

For example, a noteworthy special case is to use beta-GQMOM with $N_s = 2$, and the mass moments $(\mathcal{M}_0, \mathcal{M}_1, \mathcal{M}_2)$. Using three mass moments is the minimal number for capturing mass polydispersity for a uni-modal NDF. Beta-GQMOM allows one to specific an upper/lower bound on the largest/smallest particle, while keeping $N > N_s$ abscissas. Finally, the simplest case is $N_s = 1$ and $N = 1$ that solves for two mass moments: $(\mathcal{M}_0, \mathcal{M}_1)$. QBMM for this case has a single Dirac delta function with number concentration $w_1 = \mathcal{M}_0$ and mean particle mass $\xi_1 = \mathcal{M}_1/\mathcal{M}_0$. This representation of the mass NDF (with zero variance) may be useful for obtaining rough information on the spatial distribution of the particle size for very small particles that nearly follow the fluid. However, it will not be able to capture size segregation due to fluid drag (or other size-dependent physics).

4.2. Mass-conditioned moments

Finding a property (e.g., velocity or internal energy) of particles with a given mass can be accomplished using the conditional quadrature method of moments (CQMOM) [31]. As described above, GQMOM provides the N weights w_β and N mass abscissae ξ_β, computed from the mass (size, or half-order) moments.[9] For example, the mass-weighted internal-energy moments $\mathcal{E}_s$ are related to the mass-conditioned internal-energy moments $M^e_\beta = M^e(\xi_\beta) = w_\beta e_p(\xi_\beta)$ by

$$\mathcal{E}_s = \sum_{\beta=1}^{N} \xi_\beta^s M^e_\beta. \tag{53}$$

For $N \geq 1$, the M^e_β for $\beta = 1, 2, \ldots, N$ are found by solving a linear system:

$$\begin{bmatrix} 1 & 1 & \cdots & 1 \\ \xi_1 & \xi_2 & \cdots & \xi_N \\ \vdots & \vdots & \ddots & \vdots \\ \xi_1^{N-1} & \xi_2^{N-1} & \cdots & \xi_N^{N-1} \end{bmatrix} \begin{bmatrix} M^e_1 \\ M^e_2 \\ \vdots \\ M^e_N \end{bmatrix} = \begin{bmatrix} \mathcal{E}_0 \\ \mathcal{E}_1 \\ \vdots \\ \mathcal{E}_{N-1} \end{bmatrix} \tag{54}$$

where the moments $(\mathcal{E}_0, \ldots, \mathcal{E}_{N-1})$ are found from the polydisperse model in table 4. To avoid ill-conditioning of the linear system, each side of eq. (53) can be divided by ξ_r^s where $0 < \xi_r$ is a reference mass. For example, the Euclidean norm of the vector of abscissae can be used for ξ_r. As the internal energy is positive, the realizability constraint on the mass-conditioned internal energies is $e_p(\xi_\beta) > 0$. The same procedure is applied to find the mass-conditioned kinetic energies $w_\beta K_p(\xi_\beta)$ from the mass-weighted kinetic-energy moments $(\mathcal{K}_0, \ldots, \mathcal{K}_{N-1})$.

Likewise, using CQMOM, the mass-weighted velocity moments $\boldsymbol{\mathcal{U}}^1_s$ are related to the mass-conditioned velocity $\mathbf{M}^1_\beta = w_\beta \mathbf{u}_p(\xi_\beta)$ by

$$\boldsymbol{\mathcal{U}}^1_s = \sum_{\beta=1}^{N} \xi_\beta^s \mathbf{M}^1_\beta. \tag{55}$$

For $N \geq 1$, using eq. (55) for the known conserved moments on the left-hand side, the $\mathbf{M}^1_\beta$ for $\beta = 1, 2, \ldots, N$ are found by solving the linear system:

$$\begin{bmatrix} 1 & 1 & \cdots & 1 \\ \xi_1 & \xi_2 & \cdots & \xi_N \\ \vdots & \vdots & \ddots & \vdots \\ \xi_1^{N-1} & \xi_2^{N-1} & \cdots & \xi_N^{N-1} \end{bmatrix} \begin{bmatrix} \mathbf{M}^1_1 \\ \mathbf{M}^1_2 \\ \vdots \\ \mathbf{M}^1_N \end{bmatrix} = \begin{bmatrix} \boldsymbol{\mathcal{U}}^1_0 \\ \boldsymbol{\mathcal{U}}^1_1 \\ \vdots \\ \boldsymbol{\mathcal{U}}^1_{N-1} \end{bmatrix}. \tag{56}$$

Again, to avoid ill-conditioning of this linear system, each side of eq. (55) can be divided by ξ_r^s where $0 < \xi_r$ is a reference mass.

[9] If mass moments are input to GQMOM, then the N abscissae ξ_β are returned. Otherwise, for size or half-order moments, ζ_β and ς_β, respectively, are returned, from which the ξ_β are computed.

In summary, for $N = 4$, the polydisperse model must provide the velocity moments $(\boldsymbol{\mathcal{U}}_0^1, \boldsymbol{\mathcal{U}}_1^1, \boldsymbol{\mathcal{U}}_2^1, \boldsymbol{\mathcal{U}}_3^1)$ in order to determine the four mass-conditioned velocities $(\mathbf{u}_p(\xi_1), \mathbf{u}_p(\xi_2), \mathbf{u}_p(\xi_3), \mathbf{u}_p(\xi_4))$. Then, the mass-conditioned granular temperatures are found from $3\Theta_p(\xi_\beta) = 2K_p(\xi_\beta) - u_p^2(\xi_\beta)$ and must be non-negative. As mentioned earlier, this velocity moment set is consistent with using the half-order moments with $N_s = 6$ (or mass moments with $N_s = 3$), because the highest-order mass moment needed is $\mathcal{M}_3$, which has the same order in mass as $\boldsymbol{\mathcal{U}}_3^1$, $\mathcal{K}_3$ and $\mathcal{E}_3$. Once the variables w_β, ξ_β, $\mathbf{u}_p(\xi_\beta)$, $\Theta_p(\xi_\beta)$, and $e_p(\xi_\beta)$ are calculated from the conserved moments, they can be used to close the source terms appearing in the transport equations as shown in table 5. Because binary collisions were assumed in the kinetic-theory derivation, double sums over all abscissae arise due to particle–particle collisions (see Appendix A). It is important to notice that the half-order-moment fluxes $\boldsymbol{\mathcal{U}}_{s/2}^1$ for $s = (1, 3, 5)$ are found from

$$\boldsymbol{\mathcal{U}}_{s/2}^1 = \sum_{\beta=1}^{4} w_\beta \xi_\beta^{s/2} \mathbf{u}_p(\xi_\beta). \tag{57}$$

For a system wherein the abscissae are uniform in space and time, this specification of the half-order-moment fluxes ensures that the abscissae remain constant.

4.3. Realizability of conditional moments

The realizability constraints on the mass-conditioned energy moments $(K_p(\xi_\beta), \Theta_p(\xi_\beta), e_p(\xi_\beta))$ must be satisfied at each time step; however, mass-conditioned moments found with CQMOM are not guaranteed to be realizable [31]. In particular, one or more mass-conditioned granular temperatures can be negative. The simplest correction is to set a negative granular temperature to zero. However, this change will increase the kinetic-energy moment $\mathcal{K}_1$ such that the total energy is not conserved. In practice, this can cause the simulation to abort. Another situation that can arise is that a mass-conditioned granular temperature becomes nonphysically too large. This is usually associated with the corresponding w_β tending towards zero. As done in [13], a physics-based upper bound can be applied for the mass-conditioned granular temperature, provided that it does not change $\mathcal{K}_1$.

To enforce conservation of total energy, it is imperative to keep $\mathcal{K}_1$ and $\mathcal{E}_1$ conserved when finding the mass-conditioned particle energies. In our code, in each grid cell, this is done for $N = 4$ as follows:

1. Find $K_p(\xi_\beta)$ for $\beta = 1, 2, 3, 4$ given $(\mathcal{K}_0, \mathcal{K}_1, \mathcal{K}_2, \mathcal{K}_3)$ using CQMOM.
2. Correct the $K_p(\xi_\beta)$ as needed so that $\Theta_p(\xi_\beta)$ is non-negative (or less than a physics-based upper limit).
3. Using the corrected $K_p(\xi_\beta)$, compute $\mathcal{K}_1^* = \sum_{\beta=1}^{4} w_\beta \xi_\beta K_p(\xi_\beta)$, which may be different than $\mathcal{K}_1$.
4. Replace the $K_p(\xi_\beta)$ with $K_p(\xi_\beta)\mathcal{K}_1/\mathcal{K}_1^*$, thereby ensuring that $\mathcal{K}_1$ is conserved.
5. Using the new $K_p(\xi_\beta)$, compute the corrected $\mathcal{K}_0$, $\mathcal{K}_2$ and $\mathcal{K}_3$.

Note that this algorithm conserves $\mathcal{K}_1$, while modifying $\mathcal{K}_0$, $\mathcal{K}_2$ and $\mathcal{K}_3$. Our numerical tests, requiring only that $\Theta_p(\xi_\beta) \geq 0$, indicate that the resulting simulations are robust and do not show any spurious behavior. We anticipate that this correction algorithm can be applied successfully for larger N.

The above algorithm can be used with other conditional variables, such as the mass-conditioned particle velocity and the mass-conditioned internal energy. For the former, as has been previously observed with QBMM [13], the magnitude of a mass-conditioned velocity may diverge as its number density tends towards zero (i.e., the overall contribution to $\boldsymbol{\mathcal{U}}_1^1$ is negligible). The main issue is then to establish an upper limit on the magnitude of the mass-conditioned velocity based on the local variables that is compatible with $\boldsymbol{\mathcal{U}}_1^1$. Notice that the velocity-correction step must be done before computing $\Theta_p(\xi_\beta)$ and correcting the mass-conditioned kinetic energies. Likewise, for the mass-conditioned internal energy, physics-based upper/lower bounds must be determined that are consistent with $\mathcal{E}_1$.

5. Application to 1-D polydisperse, high-speed, fluid–particle flows

In this section, we first present the 1-D model equations for $N = 4$ and $N_s = 6$ using half-order mass moments, and then describe the numerical method used to solve them. The section ends with a description of the two example applications.

5.1. 1-D model equations

The 1-D conservation equations for the fluid phase are

$$\begin{aligned}
\partial_t \rho_f \alpha_f^\star + \partial_x \rho_f \alpha_f^\star u_f &= -\mathcal{S}_1^0, \\
\partial_t \rho_f \alpha_f^\star u_f + \partial_x (\rho_f \alpha_f^\star u_f^2 + \hat{p}_f) - \alpha_p^\star (\partial_x \hat{p}_f + F_{pf}) &= \mathcal{A}_1^1 - \mathcal{S}_1^1, \\
\partial_t \rho_f \alpha_f^\star k_f + \partial_x \rho_f \alpha_f^\star u_f k_f + \frac{2}{3} \rho_f \alpha_f^\star k_f \partial_x u_f &= \mathcal{A}_1^f - (2 - 2a + C_g)\, \mathcal{B}_1^f\, k_f, \\
\partial_t \rho_f \alpha_f^\star E_f + \partial_x [\rho_f \alpha_f^\star u_f E_f + (\alpha_f^\star u_f + \alpha_p^\star u_p) \hat{p}_f] + P_{pfp} \partial_x u_p - \alpha_p^\star u_p (\partial_x \hat{p}_f + F_{pf}) &= \mathcal{A}_1^2 - (1-a)\mathcal{B}_1^2 - \mathcal{A}_1^e - \mathcal{S}_1^2 - \mathcal{S}_1^e.
\end{aligned} \tag{58}$$

The formulas for the source terms on the right-hand side are provided in table 5.

To account for added mass, we solve for the particle-phase volume fraction:

$$\partial_t \alpha_p + \partial_x \alpha_p u_p = 0 \tag{59}$$

where $u_p = \mathcal{U}_1^1 / \mathcal{M}_1$ is found from the polydisperse moments with $s = 1$. Given α_p, the formulas in eq. (3) are used for find α_a. We use GQMOM for the half-order moments with $N_s = 6$. The 19 conserved variables for the polydisperse particle phase are ($\mathcal{M}_0$, $\mathcal{M}_{1/2}$, $\mathcal{M}_1$, $\mathcal{M}_{3/2}$, $\mathcal{M}_2$, $\mathcal{M}_{5/2}$, $\mathcal{M}_3$), ($\mathcal{U}_0^1$, $\mathcal{U}_1^1$, $\mathcal{U}_2^1$, $\mathcal{U}_3^1$), ($\mathcal{K}_0$, $\mathcal{K}_1$, $\mathcal{K}_2$, $\mathcal{K}_3$), and ($\mathcal{E}_0^e$, $\mathcal{E}_1^e$, $\mathcal{E}_2^e$, $\mathcal{E}_3^e$). The system of seven 1/2-order-moment conservation equations is

$$\begin{aligned}
\partial_t \mathcal{M}_0 + \partial_x \mathcal{U}_0^1 &= \mathcal{S}_0^0, \\
\partial_t \mathcal{M}_{1/2} + \partial_x \mathcal{U}_{1/2}^1 &= \mathcal{S}_{1/2}^0, \\
\partial_t \mathcal{M}_1 + \partial_x \mathcal{U}_1^1 &= \mathcal{S}_1^0, \\
\partial_t \mathcal{M}_{3/2} + \partial_x \mathcal{U}_{3/2}^1 &= \mathcal{S}_{3/2}^0, \\
\partial_t \mathcal{M}_2 + \partial_x \mathcal{U}_2^1 &= \mathcal{S}_2^0, \\
\partial_t \mathcal{M}_{5/2} + \partial_x \mathcal{U}_{5/2}^1 &= \mathcal{S}_{5/2}^0, \\
\partial_t \mathcal{M}_3 + \partial_x \mathcal{U}_3^1 &= \mathcal{S}_3^0.
\end{aligned} \tag{60}$$

For the mass-velocity moments, the conservation equations for momentum are

$$\begin{aligned}
\partial_t \mathcal{U}_0^1 + \partial_x (\mathcal{U}_0^2 + P_p \mathcal{M}_0) + \frac{\mathcal{M}_0}{\mathcal{M}_1} \partial_x P_{pfp} + \frac{1}{\rho_e} (\partial_x \hat{p}_f + F_{pf}) \mathcal{M}_0 &= -\mathcal{A}_0^1 + C_0^1 + \mathcal{F}_0^1 + \mathcal{S}_0^1, \\
\partial_t \mathcal{U}_1^1 + \partial_x (\mathcal{U}_1^2 + P_p \mathcal{M}_1) + \partial_x P_{pfp} + \frac{1}{\rho_e} (\partial_x \hat{p}_f + F_{pf}) \mathcal{M}_1 &= -\mathcal{A}_1^1 + \mathcal{S}_1^1, \\
\partial_t \mathcal{U}_2^1 + \partial_x (\mathcal{U}_2^2 + P_p \mathcal{M}_2) + \frac{\mathcal{M}_2}{\mathcal{M}_1} \partial_x P_{pfp} + \frac{1}{\rho_e} (\partial_x \hat{p}_f + F_{pf}) \mathcal{M}_2 &= -\mathcal{A}_2^1 + C_2^1 + \mathcal{F}_2^1 + \mathcal{S}_2^1, \\
\partial_t \mathcal{U}_3^1 + \partial_x (\mathcal{U}_3^2 + P_p \mathcal{M}_3) + \frac{\mathcal{M}_3}{\mathcal{M}_1} \partial_x P_{pfp} + \frac{1}{\rho_e} (\partial_x \hat{p}_f + F_{pf}) \mathcal{M}_3 &= -\mathcal{A}_3^1 + C_3^1 + \mathcal{F}_3^1 + \mathcal{S}_3^1.
\end{aligned} \tag{61}$$

The balance equations for kinetic energy are

$$\begin{aligned}
\partial_t \mathcal{K}_0 + \partial_x \left(\mathcal{U}_0^3 + P_p \mathcal{U}_0^1 \right) + \frac{1}{\mathcal{M}_1} \mathcal{U}_0^1 \partial_x P_{pfp} + \frac{1}{\rho_e} (\partial_x \hat{p}_f + F_{pf}) \mathcal{U}_0^1 &= -\mathcal{A}_0^2 + \frac{1}{2} C_0^2 + \frac{1}{2} \mathcal{F}_0^2 + \mathcal{S}_0^2, \\
\partial_t \mathcal{K}_1 + \partial_x \left(\mathcal{U}_1^3 + P_p \mathcal{U}_1^1 \right) + \frac{1}{\mathcal{M}_1} \mathcal{U}_1^1 \partial_x P_{pfp} + \frac{1}{\rho_e} (\partial_x \hat{p}_f + F_{pf}) \mathcal{U}_1^1 &= -\mathcal{A}_1^2 + \frac{1}{2} C_1^2 + \frac{1}{2} \mathcal{F}_1^2 + \mathcal{S}_1^2, \\
\partial_t \mathcal{K}_2 + \partial_x \left(\mathcal{U}_2^3 + P_p \mathcal{U}_2^1 \right) + \frac{1}{\mathcal{M}_1} \mathcal{U}_2^1 \partial_x P_{pfp} + \frac{1}{\rho_e} (\partial_x \hat{p}_f + F_{pf}) \mathcal{U}_2^1 &= -\mathcal{A}_2^2 + \frac{1}{2} C_2^2 + \frac{1}{2} \mathcal{F}_2^2 + \mathcal{S}_2^2, \\
\partial_t \mathcal{K}_3 + \partial_x \left(\mathcal{U}_3^3 + P_p \mathcal{U}_3^1 \right) + \frac{1}{\mathcal{M}_1} \mathcal{U}_3^1 \partial_x P_{pfp} + \frac{1}{\rho_e} (\partial_x \hat{p}_f + F_{pf}) \mathcal{U}_3^1 &= -\mathcal{A}_3^2 + \frac{1}{2} C_3^2 + \frac{1}{2} \mathcal{F}_3^2 + \mathcal{S}_3^2.
\end{aligned} \tag{62}$$

For the mass-internal-energy moments, the conservation equations are

$$\begin{aligned}
\partial_t \mathcal{E}_0 + \partial_x \mathcal{U}_0^e &= \mathcal{A}_0^e - \frac{1}{2}C_0^2 - \frac{1}{2}\mathcal{F}_0^2 + \mathcal{S}_0^e, \\
\partial_t \mathcal{E}_1 + \partial_x \mathcal{U}_1^e &= \mathcal{A}_1^e - \frac{1}{2}C_1^2 - \frac{1}{2}\mathcal{F}_1^2 + \mathcal{S}_1^e, \\
\partial_t \mathcal{E}_2 + \partial_x \mathcal{U}_2^e &= \mathcal{A}_2^e - \frac{1}{2}C_2^2 - \frac{1}{2}\mathcal{F}_2^2 + \mathcal{S}_2^e, \\
\partial_t \mathcal{E}_3 + \partial_x \mathcal{U}_3^e &= \mathcal{A}_3^e - \frac{1}{2}C_3^2 - \frac{1}{2}\mathcal{F}_3^2 + \mathcal{S}_3^e.
\end{aligned} \tag{63}$$

The collisional and frictional source terms on the right-hand sides are given in section 3.8. The formulae for the spatial fluxes and source terms are provided in table 5. The 1-D polydisperse model has a total of 24 conserved variables.

5.2. Numerical implementation

As done for monodisperse cases in [6], the coupled fluid–particle moment equations have been implemented in a 1-D flow solver. Given that the overall system of equations is hyperbolic, the extension to three dimensions on a structured Cartesian grid would use the same approach with directional splitting [18]. Details on the numerical algorithms are provided in the indicted appendices, and in [6].

Fluid and added-mass phases. The following items have been implemented for the fluid phase:

1. The buoyancy and F_{pf} terms coupled to the particle phase.
2. The drag terms, including PTKE, coupled to the particle phase.
3. The convective heat-transfer term coupled to the particle phase.
4. The added-mass source terms coupled to the particle phase.

Particle phase. The following items have been implemented for the particle phase:

1. The moment-inversion algorithm GQMOM to compute the abscissae.
2. The moment-inversion algorithm CQMOM to compute the mass-conditioned velocity, kinetic energy, and internal energy.
3. The collisional and frictional particle pressures.
4. The buoyancy, F_{pf}, and P_{pfp} terms coupled to the fluid phase (see Appendix D).
5. The collision source terms, including internal energy (see Appendix C).
6. The friction source terms, including internal energy (see Appendix C).
7. The drag terms, including PTKE, coupled to the fluid phase (see Appendix B).
8. The convective heat-transfer term (see Appendix B).
9. The added-mass source terms (see Appendix E).

An operator-splitting approach is employed to solve the coupled moment equations (i.e., for fluid and particles) separately for each item listed above. In the first step, a first order in space and time HLL scheme [14] is used to advance the coupled moment system due to the spatial fluxes. The eigenvalues for the spatial flux are found numerically using a subroutine for the Jacobian matrix that was generated symbolically. These eigenvalues are used to define the numerical fluxes in HLL, and to set the overall time step [14]. After advancing the moments due to the spatial fluxes, the changes due to buoyancy, F_{pf}, and P_{pfp} are computed using an Euler scheme with central differences [14]. Next, the changes in the moments due to the collisional and frictional source terms are computed. Finally, the changes in the moments due to drag and heat transfer are computed. The collisions, friction, drag, and heat transfer are handled with semi-analytical solutions (see Appendix B for an example). Since these source terms do not change the mass abscissas, the solver uses the mass-conditioned velocity moments instead of the mass–velocity moments. Then, GQMOM is used to find the latter from the updated mass-conditioned moments.

When the velocity variance is extremely small (or negative due to round-off error), application of HyQMOM to find M_3 is ill-conditioned. Thus, realizability is checked after each sub-step and the velocity moments are corrected

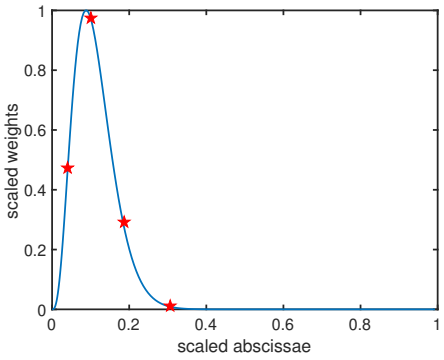

Figure 2: Initial beta PDF of particle diameters scaled by the maximum value (blue curve). The four GQMOM scaled abscissas for diameter $d_p(\xi_\beta)$ are shown by red symbols. These abscissae are used to compute the mass abscissae ξ_β via eq. (15). The scaled weights are multiplied by a constant to achieve the desired α_p.

if needed. Based on numerical experiments, corrections are rarely applied and when they are it usually occurs at the interface with 'particle-free' regions. In the simulations, to avoid division by zero, such regions are initialized with a tiny particle number density. Thus, applying the realizability corrections has no impact on the observable quantities.

The Jacobian matrix needed for the HLL solver can be computed symbolically for $N = 2$, but not with $N = 3$. In any case, the number of eigenvalues becomes quite large for $N > 2$, and only the magnitudes of the largest and smallest eigenvalues are required to define the numerical fluxes. From numerical experiments, it was determined that the latter are well approximated by the nine eigenvalues found for the monodisperse system,[10] i.e., using the added mass and fluid+particle-phase moments. We should emphasize that the intermediate eigenvalues are not available using this approach, but that has no importance for the HLL solver. In general, unless the particle phase is very dense, the largest/smallest eigenvalues correspond to the fluid phase, albeit modified by the presence of the particles.

5.3. Numerical test problems

Two test problems are used to demonstrate the polydisperse model. In the first problem, a shock wave impinging on a dense particle curtain is simulated. As shown in fig. 2, the particle diameter distribution in the particle curtain is initialized as a beta PDF with a mean of 100 μm and maximum of 1000 μm. In the second problem, two particle-laden jets impinge at the center of the domain. We use again a beta PDF with mean size of 100 ηm on the left side and 200 μm on the right side. Simulations have also been run using a lognormal distribution and the results are qualitatively very similar. For both cases, a 1-D computational domain is discretized with 2000 computational cells. In the simulations, we solve for the half-order mass moments ($\mathcal{M}_0$, $\mathcal{M}_{1/2}$, $\mathcal{M}_1$, $\mathcal{M}_{3/2}$, $\mathcal{M}_2$, $\mathcal{M}_{5/2}$, $\mathcal{M}_3$) and use beta-GQMOM to find ς_1, ς_2, ς_3 and ς_4 at each grid point. In order to account for large particle Reynolds numbers and the volume fraction, the drag coefficient is modeled using the Schiller–Naumann formula with the Richardson–Zaki correction used to account for clustering effects [5]:

$$C_D = \frac{24}{Re_p}(1 + 0.15Re_p^{0.687})\alpha_f^{-2.65} \tag{64}$$

where Re_p is different for each particle size. The added-mass timescale τ_a is found from the drag timescales using

$$\frac{1}{\tau_a} = \frac{1}{\rho_e \alpha_p^\star} \sum_{\beta=1}^{4} \frac{w_\beta \xi_\beta}{\tau_p(\xi_\beta)}. \tag{65}$$

The reference value for the frictional pressure constant has been set at $p_f = 533,333$ Pa. The initial thermodynamic temperatures of the particles is set equal to the fluid, and $\rho_p = 2500$ kg/m^3. (Results for monodisperse particles with a wide range of ρ_f/ρ_p are presented in [6].) The default model parameters are given in table 3. Unless stated otherwise, these parameters will be used below. For all cases, the 1-D computational domain extends from -0.2 m to 0.2 m.

[10] In fact, only the seven eigenvalues found with $k_g = e_p = 0$ suffice since these variables are advected with the mean phase velocities.

6. Numerical results

Quantitative examples of shock–particle-curtain interactions using the monodisperse model are available in [6], along with details on the initial conditions and experimental setup used for validation. Here, we focus on qualitative comparisons with emphasis on the effect of polydisperse particles.

6.1. Results for polydisperse particle curtain

The initial number concentrations of the four types of particles inside the curtain are larger than 10^5 1/m^3 due to the small particle diameters. Outside the curtain, relatively smaller values of number concentration are used to avoid division by zero. The fluid density and temperature before the shock (right side) are $\rho_f = 1.18$ kg/m^3 and 300 °K, respectively. Behind the shock (left side), they are $\rho_f = 2.476$ kg/m^3 and 429 °K, respectively. Different temperatures are used to illustrate the effect of heat transfer. The initial phase velocities are null, and inside the curtain α_p is uniform and three cases are simulated $\alpha_p = (0.01, 0.2, 0.6)$. In order to test the robustness of the code, we use $e_c = 1$ so that the particle collisions are elastic. In general, we found that elastic particles are most sensitive to numerical errors that can lead to numerical instabilities. Simulations with inelastic particles were also carried out and are qualitatively very similar.

The space–time contour plots in fig. 3 for the three cases with different initial values of α_p illustrate the qualitative behavior of the model variables. The initial shock, located just to the left of the particle curtain ($x < 0$), is partially reflected, depending on the curtain density. For 0.01, the reflection is very weak, while for 0.6 it is very strong. This creates jumps in density ρ_g and temperature T_g upstream from the curtain. The particle curtain (i.e., α_p) is first compacted due to the shock, before beginning to spread and move to the right. In doing so, the particles exhibit strong size segregation (see $d_{21} = (\mathcal{M}_2/\mathcal{M}_1)^{1/3}$) with small particles accelerating faster than large particles. For 0.01, there are very few particle–particle collisions so that the segregation occurs faster. At $\alpha_p = 0.2$, the frictional pressure P_f plays no role, but the collisional pressure P_c is significant. This causes the larger particles to move to the left of their original position, which shows up in the variable T_p. Due to thermal inertia, the particle temperatures do not change much from their initial values. Thus, the lower T_p on the left side is caused be particles bouncing back due to collisions. Finally, for initial value $\alpha_p = 0.6$, the frictional pressure is very large at short times due to particle packing. The larger mass of the particle curtain at 0.6 slows its acceleration, generating a large drop in p_g across the curtain.

In fig. 4, the weights (number concentration) and mass abscissae at the end of the simulation (2×10^{-3} s) are plotted. Notice that the extreme values (left and right of domain) correspond to the initial values, and that for the abscissae these values are the same for all cases. From the abscissae, it is clear that inside the curtain the particle mass decreases continuously from left to right. Moreover, because GQMOM represents a continuous NDF, the largest (ξ_4) is larger than the initial size. As mentioned above, the size segregation is largest for $\alpha_p = 0.01$ due to the relative lack of collisions. In fig. 5, the contributions to the particle pressure are shown for each case. Aside from the kinetic pressure ($\rho_e \alpha_p^\star \Theta_p$), the pfp pressure is dominant for 0.01, while the collisional component plays a more significant role for 0.2 and 0.6. Notice that the frictional component is null in fig. 5 because α_p is everywhere below α_{max}. Finally, notice in fig. 4 that the strong segregation for 0.01 leads to two abscissae very close to the mean mass near $x = 0.125$. In fact, for this case the mean mass for $x > 0.125$ is very close to the smallest abscissa, indicating that the variance of the mass NDF is very small due to segregation. For 0.2 and 0.6, similar behavior is observed, but to a lesser extent because the gas velocity is lower so that the spreading rate is lower for these cases.

In fig. 6 the mass-conditioned velocities and temperatures, as well as the gas velocity u_g and mean particle values u_p and T_p are plotted at the end of the simulation ($t = 2 \times 10^{-3}$ s). For all cases, the particle velocities lag behind the gas velocity due to particle inertia. The same is true for the particle temperatures due to thermal inertia. As expected, the smaller particles approach the gas values faster than the larger particles. More interesting is the effect of collisions on momentum transfer between different particle masses. For 0.01 where collisions are weak, the mass-conditioned particle velocities inside the curtain remain well separated. On the other hand, for 0.6 where collisions are strong, the mass-conditioned particle velocities inside the curtain are nearly the same. This effect leads to the particle temperatures being nearly equal inside the curtain. Finally, notice that for 0.01 some of the conditional velocities exhibit large variations near $x = 0.125$ where $u_p \approx u_p(\xi_1)$. The reason for this behavior is that the linear system in CQMOM becomes poorly conditioned when the variance of the mass NDF is small. One possible solution to overcome this issue would be to reduce the number of abscissae N in spatial regions where this occurs. Typically, such regions have very small particle volume fraction and a detailed representation of the mass NDF is not needed.

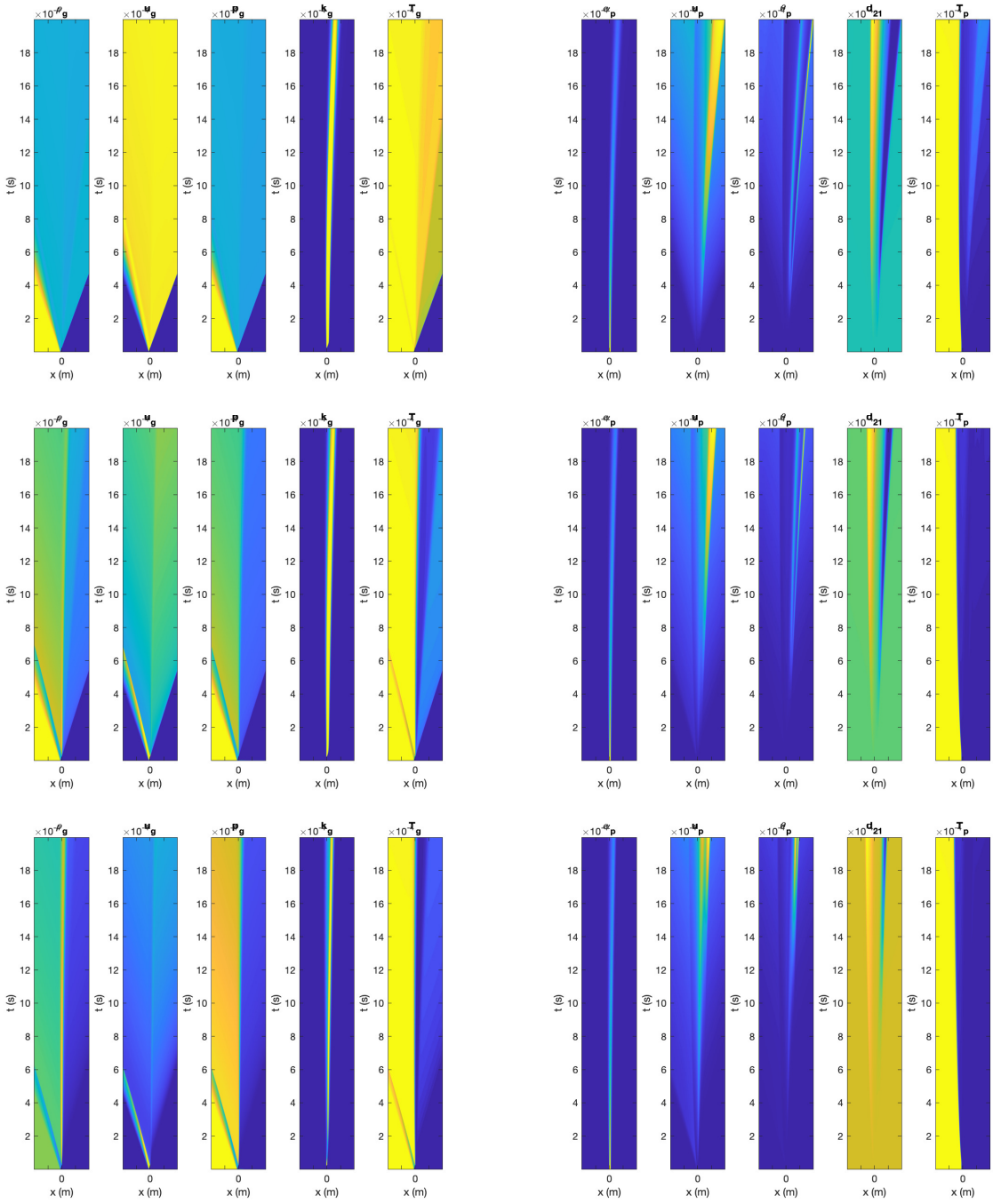

Figure 3: Space–time contour plots for the polydisperse particle curtain with initial $\alpha_p = 0.01$ (top), 0.2 (middle), 0.6 (bottom). Left: Gas-phase variables (ρ_g, u_g, p_g, k_g, T_g). Right: Particle-phase variables (α_p, u_p, Θ_p, d_{21}, T_p). The reflected shock is most easily observed from ρ_g in the far-left column, while size segregation is seen from the mean particle size d_{21}.

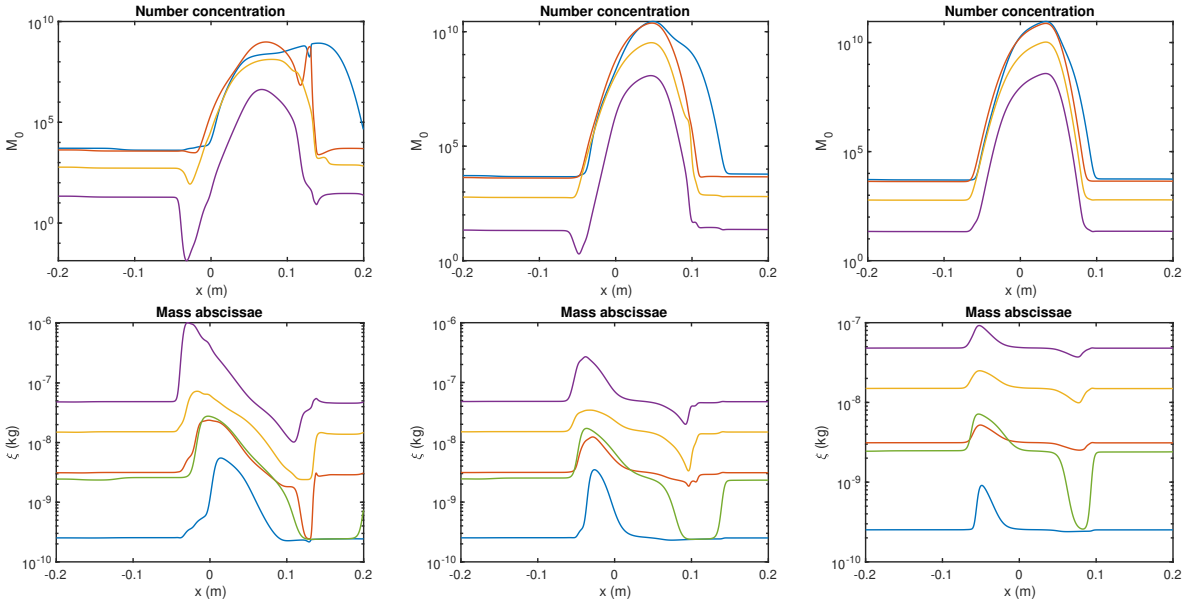

Figure 4: Model predictions for the polydisperse particle curtain with initial $\alpha_p = 0.01$ (left), 0.2 (middle), 0.6 (right) at $t = 2 \times 10^{-3}$ s. Number concentrations (top) corresponding to mass abscissae (bottom) with the same color. The green curve (bottom) is the mean particle mass.

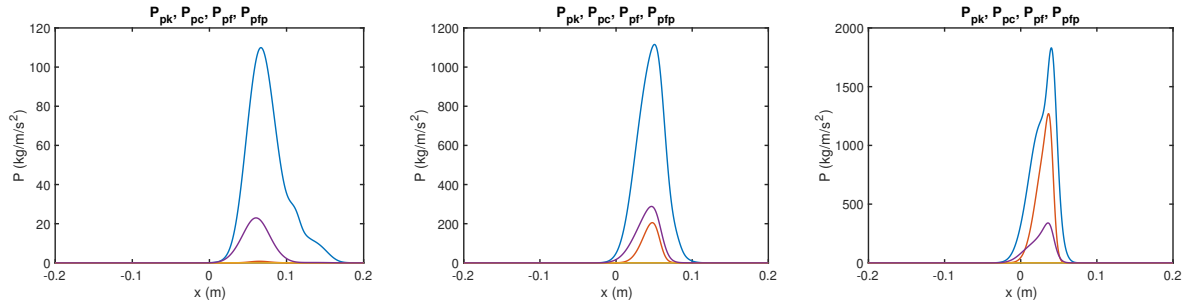

Figure 5: Particle-phase pressure components for the polydisperse particle curtain with initial $\alpha_p = 0.01$ (left), 0.2 (middle), 0.6 (right) at $t = 2 \times 10^{-3}$ s. Kinetic (blue), collisional (red), frictional (gold) and pfp pressure (purple).

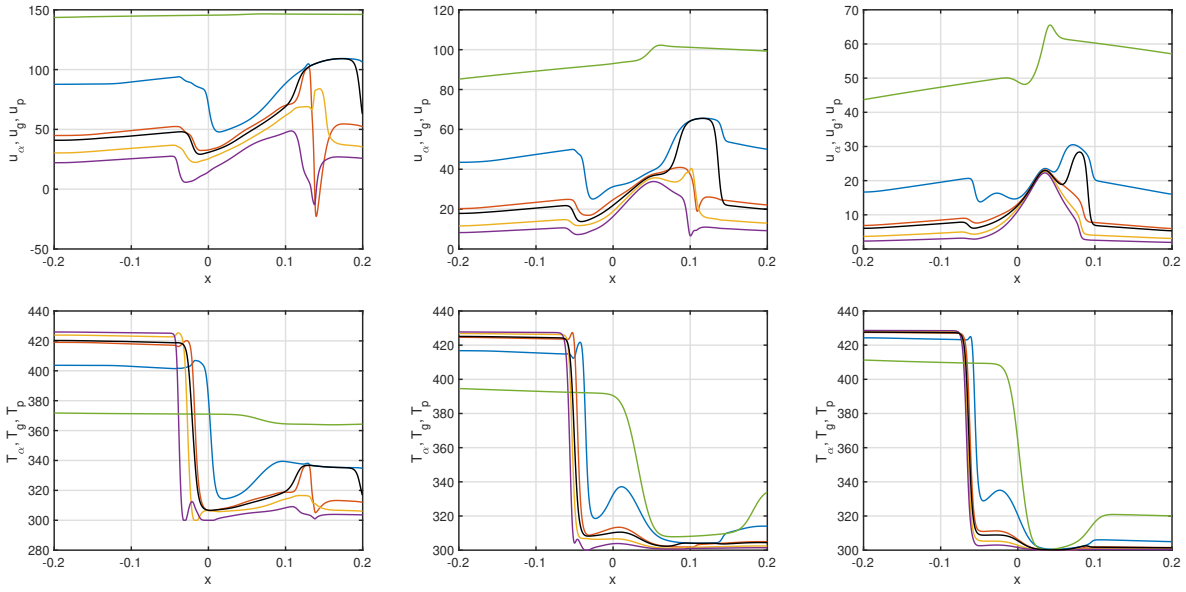

Figure 6: Mass-conditioned velocity (top) and temperature (bottom) for the polydisperse particle curtain with initial $\alpha_p = 0.01$ (left), 0.2 (middle), 0.6 (right) at $t = 2\times10^{-3}$ s. Colors correspond to mass abscissae in fig. 4. The green curve is the gas velocity u_g (top) and temperature T_g (bottom). The black curve is the mean particle velocity u_p (top) and temperature T_p (bottom).

However, when adapting N to the local conditions, care must be taken to conserve the particle-phase mass, momentum and energy (which can be accomplished even in the monodisperse limit with $N = 1$). In practice, reducing N will be simpler from a computational standpoint than increasing N in regions where the variance of the mass NDF abruptly increases (e.g., crossing jets).

6.2. Results for polydisperse crossing jets

Crossing jets are often used to test QBMM for the velocity moments in the absence of collisions [9]. It is well known that collision-less systems require velocity moments up to at least third order to correctly capture trajectory crossing [11]. Here, however, the polydisperse model is closed at the level of second-order velocity moments because we assume that α_p is large enough that particle–particle collisions cannot be neglected [29]. Thus, for this example, the initial particle volume fraction is uniform with $\alpha_p = 0.2$. The initial phase velocities are 100 m/s (left) and -100 m/s (right). The initial fluid and particle temperatures are 300 °K. The initial granular temperature is null, but grows rapidly at $x = 0$ due to the crossing jets. The collision model is therefore very important, and we shall vary the restitution coefficient e_c to investigate the effect of inelastic collisions and particle heating. For this example, size segregation is not as important as in the previous example. Nonetheless, to test the transport scheme for mass moments, we use a mass NDF on each side of $x = 0$ (see fig. 2) with mean diameters that differ by a factor of two. Finally, the simulation with $e_c = 0.9$ was ran until $t = 2\times10^{-3}$ s, while for larger e_c the end time was set as 1×10^{-3} s due to the difference in the dynamics.

Space–time contour plots of the variables at the end of the simulation are shown in fig. 7 for $e_c = (1, 0.999, 0.9)$. Due to the balance between the left and right incoming momenta, the fluid and particle velocities are null in the center region. Otherwise, the behavior of the variables is highly dependent on e_c. For elastic collisions, α_p never reaches close-packed conditions (maximum $\alpha_p \approx 0.36$), which is not the case for $e_c = 0.999$. Indeed, even with a small amount of in-elasticity, the strong collisions between the crossing jets transforms kinetic to internal energy, which lowers the collisional pressure (see fig. 8). Once the particles in the center reach close-packed conditions, the granular temperature goes to zero, leaving only the frictional pressure. With $e_c = 0.9$, this process occurs very early and only a tiny region with significant collisional pressure is observed. In summary, there are two possible regimes: with and without a close-packed region, that depend on the inlet α_p and, most importantly, on e_c. If α_p is too small, the dynamics are driven by the gas phase and particles are pushed out before they can become close-packed. Otherwise,

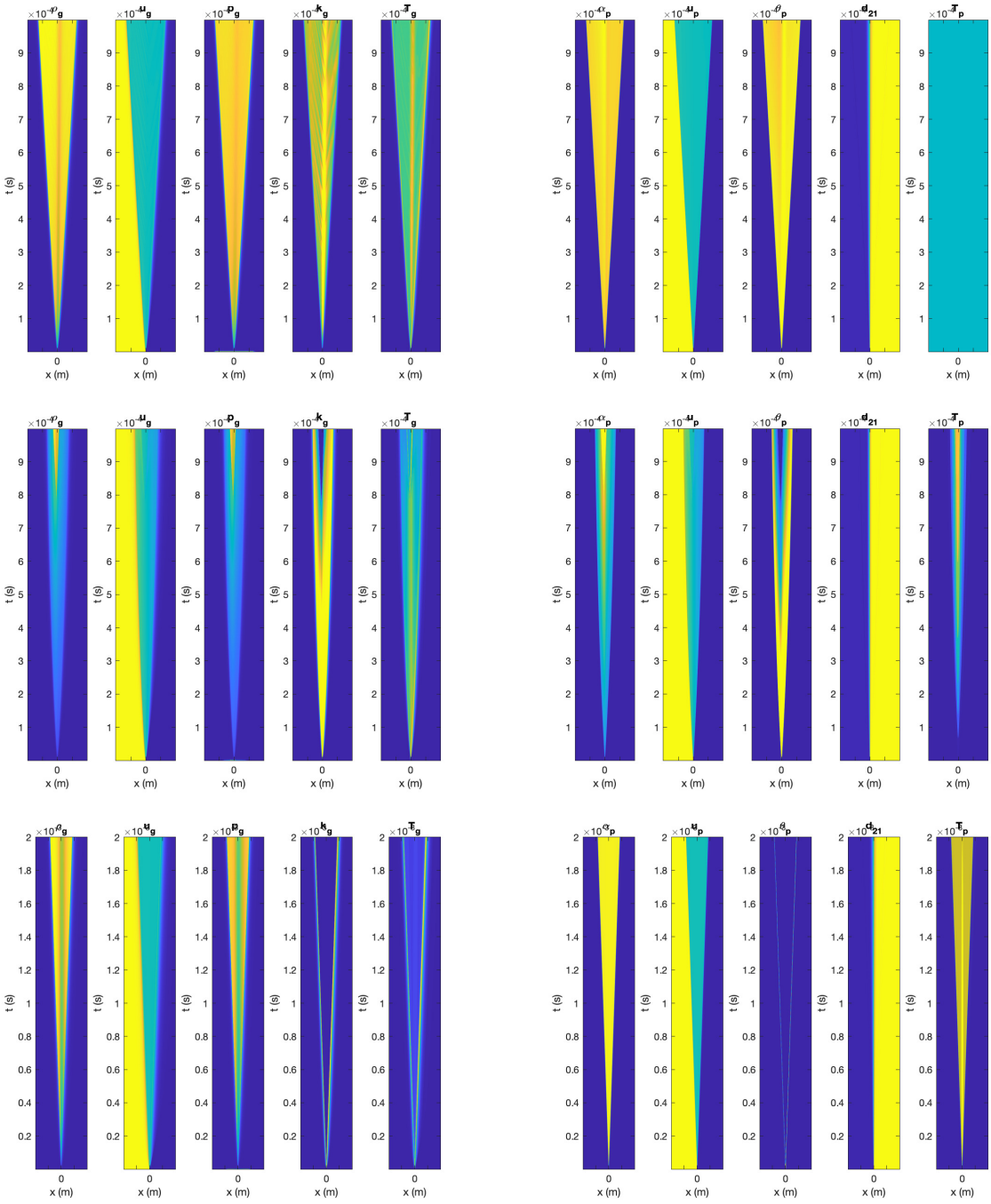

Figure 7: Space–time contour plots for the polydisperse crossing jets with $e_c = 1$ (top), 0.999 (middle), 0.9 (bottom). Left: Gas-phase variables (ρ_g, u_g, p_g, k_g, T_g). Right: Particle-phase variables (α_p, u_p, Θ_p, d_{21}, T_p). For elastic collisions (top), α_p never reaches close-packed conditions and the granular temperature remains large along the line $x = 0$. Otherwise, for inelastic collisions, a close-packed region is formed.

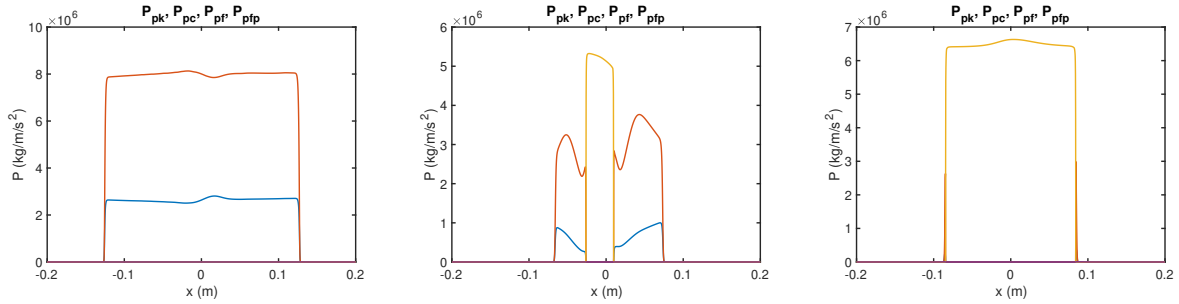

Figure 8: Particle-phase pressure components for the polydisperse crossing jets with $e_c = 1$ (left), 0.999 (middle), 0.9 (right) at the end of the simulation. Kinetic (blue), collisional (red), frictional (gold), and pfp pressure (purple). Elastic collisions lead to zero frictional pressure and large collisional pressure. The opposite is observed for inelastic collisions.

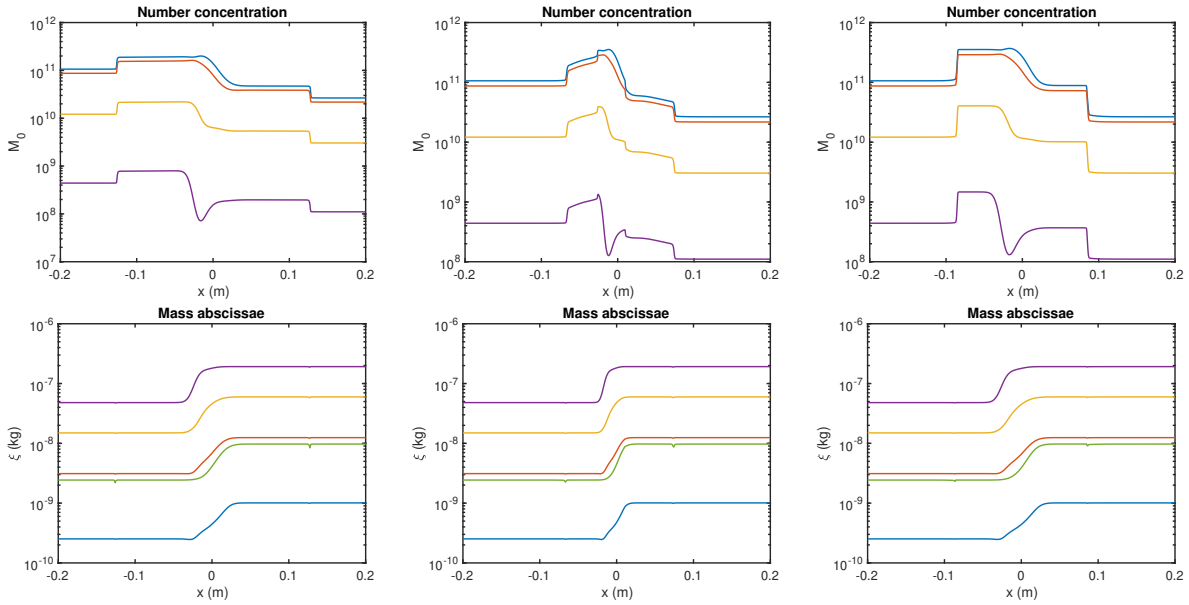

Figure 9: Model predictions for the polydisperse crossing jets with $e_c = 1$ (left), 0.999 (middle), 0.9 (right) at the end of the simulation. Number concentrations (top) correspond to mass abscissae (bottom) with the same color. The green curve (bottom) is the mean particle mass. With inelastic collisions, the particle size distribution are 'frozen' in place due to lack of transport.

the dynamics are driven by the particle phase as discussed in more detail below. Finally, note from fig. 8 that the pfp pressure plays no role in the dynamics for this example, which are dominated by the collisional and/or frictional pressure.

In fig. 9, it can be observed that the mass abscissae do not change outside the region (-0.05,0.05). This is because the mass-conditioned velocities are 'frozen' to the mean particle velocity due to collisions and friction (see fig. 10).[11] On the other hand, the mass-conditioned temperatures depend strongly on the value of e_c due to collisional/frictional heating (H_p). Notice in fig. 10 that the individual temperatures remain separated in the close-packed regime. This is due to two reasons. First, collisions between the smaller particles are more frequent due to their small mass leading to a higher granular temperature. This causes them to heat up faster than larger particles. Second, we have neglected conductive heat transfer between particles in contact (see eq. (34)). This implies that the particle temperatures can reach equilibrium only due to heat transfer with the fluid phase. Nonetheless, the equilibrium temperature is T_p (black

[11] Unlike the mass-conditioned velocities, the mass-conditioned granular temperatures in the collisional regime will not be equal because they depend on the particle mass. At equilibrium, $\xi_\beta \Theta_p(\xi_\beta)$ will be the same for all β.

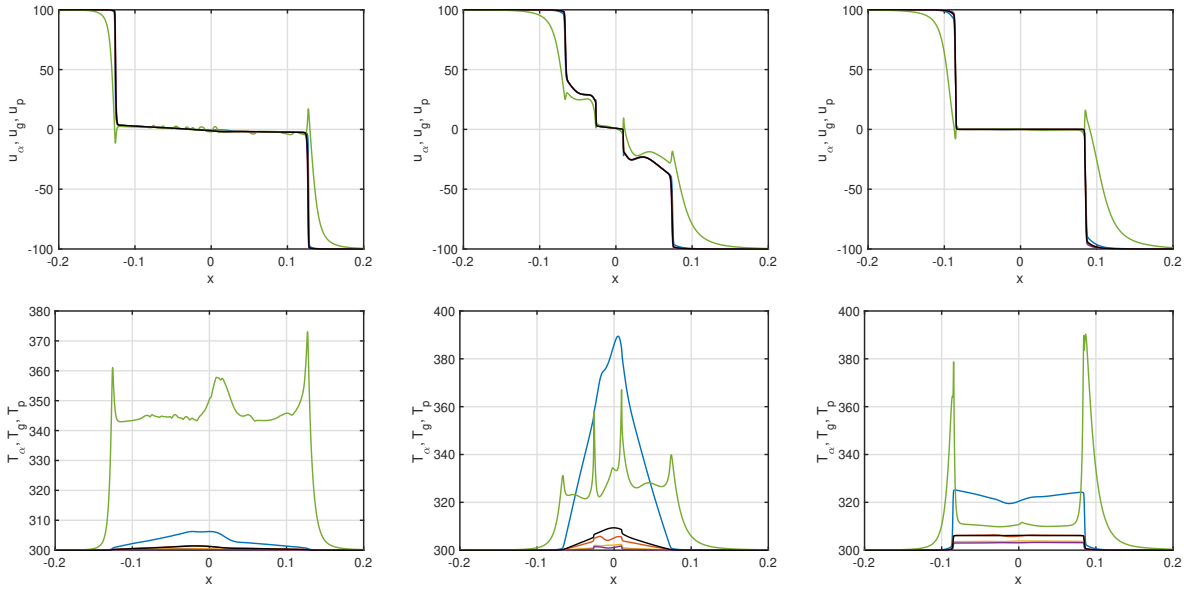

Figure 10: Mass-conditioned velocity (top) and temperature (bottom) for the polydisperse crossing jets with $e_c = 1$ (left), 0.999 (middle), 0.9 (right) at the end of the simulation. Colors correspond to mass abscissae in fig. 9. The green curve is the gas velocity u_g (top) and temperature T_g (bottom). The black curve is the mean particle velocity u_p (top) and temperature T_p (bottom). With inelastic collisions, the smallest particles can have higher temperature than the gas.

curve), whose value is very different for elastic versus inelastic collisions. Finally, it is also interesting to observe how the gas temperature T_g differs in the collisional ($e_c = 1$, $\alpha_p \approx 0.36$) versus frictional ($e_c = 0.9$, $\alpha_p \approx 0.63$) regimes.

In order to understand the differences in the dynamics, the flux eigenvalues employed in the HLL solver are shown in fig. 11, along with the maximum/minimum particle-phase eigenvalues found by neglecting the frictional pressure. Notice that the eigenvalues on the left/right sides of each figure are the same because they correspond to the initial conditions where the HLL eigenvalues are set by the fluid. For $e_c = 1$, the HLL eigenvalues in the center are set by the particle-phase collisional pressure, and the corresponding speed of sound is significantly larger than for the fluid. In contrast, for $e_c = 0.9$ the HLL eigenvalues are set by the frictional pressure. Interestingly, in this case the speed of sound in the close-packed region matches the values in the fluid at the interface. This is because $\alpha_p > \alpha_{max}$ in the close-packed region adjusts to match the interface pressures. The case with $e_c = 0.999$ has more complicated behavior. For the close-packed region in the center, the HLL eigenvalues show the same behavior as $e_c = 0.9$. Likewise for the collisional region on the outside. However, there is a small transition region between the close-packed and collisional

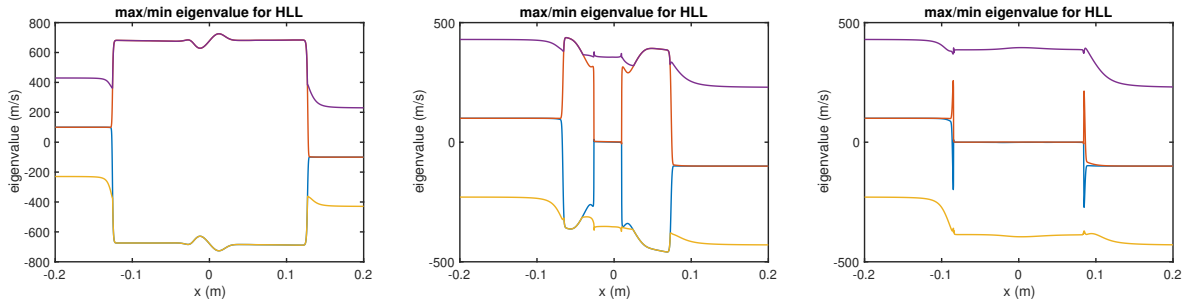

Figure 11: Eigenvalues used in HLL for the polydisperse crossing jets with $e_c = 1$ (left), 0.999 (middle), 0.9 (right) at the end of the simulation. Particle-phase without friction minimum (blue) and maximum (red). HLL minimum (gold) and maximum (purple). The collisional region corresponds to the red/blue curves being maximum/minimum. The frictional region corresponds to the center region where the red and blue curves overlap. A transition region separates the collisional and frictional regions when $e_c = 0.999$.

regions wherein the HLL eigenvalues are set by the fluid speed of sound. Hyperbolic solvers such as HLL that require estimates of the maximum/minimum eigenvalues may fail in the transition region if the magnitudes of the eigenvalues are underestimated.

7. Conclusions

In this work, we have extended the macroscale model developed in [6] to handle particles with different diameters but with the same solid density using the polydisperse kinetic theory from [19]. The first step was to develop a kinetic model for the number density function $f(\xi, \mathbf{u}, e)$ based on the underlying physics, which includes size-dependent particle acceleration due to fluid drag, buoyancy, unsteady forces, and the particle–fluid–particle pressure, as well as particle–particle interactions due to collisions and friction, and heat transfer with the fluid phase. The resulting kinetic equation is in closed form and contains all of the physical models for the microscale physics. The second step was to derive balance equations for selected moments of $f(\xi, \mathbf{u}, e)$ that ensure mass, momentum and energy conservation as well as predicting the evolution of the properties of the particle mass distribution. Because they contain integrals with respect to $f(\xi, \mathbf{u}, e)$, these balances equations are not closed given only the selected moments, which represent the conserved variables. Thus, the third step was to provide moment closures using quadrature-based moment methods. The final step was to develop a numerical algorithm for solving the system of conserved variables, ensuring that the moments remain realizable when advanced in time throughout the computational domain. For this purpose, the hyperbolic conservation equations were solved using an HLL scheme for the spatial fluxes [21, 28] and operator splitting with semi-analytical solutions for each of the sources terms. The robustness of the numerical scheme was tested using two examples of 1-D high-speed, gas–particle flows with very different physics. Moreover, the basic structure of the 1-D solver carries over to 2-D and 3-D spatial domains [18]. Furthermore, as shown in [6], the effect of added mass is included in the basic two-fluid model, which allows it to handle any particle-to-fluid density ratio (e.g., polydisperse bubbly flows).

In future work, the polydisperse model can be extended in several different directions. For example, chemical species can be added in each phase [18] to simulate chemically reacting flows, or multiple particle phases with different solid properties for each phase can be derived to account for interactions between particles types. Another potential extension would be to add terms to the kinetic equation that describe changes in the particle mass (e.g., breakage or aggregation) [22]. In any case, the starting point for deriving such models for the particle phase is a closed kinetic equation containing all of the relevant microscale physics. In this work we have limited the description of the particle velocity to the trace of the second-order velocity moments (i.e., the particle-phase kinetic energy). However, it is well known [9] that crossing jets in the absence of collisions cannot be described by a Maxwellian distribution for the particle velocity. Thus, a macroscale model that closes at the level of the particle-phase kinetic energy will yield qualitatively incorrect results for dilute impinging jets. However, if third- and fourth-order velocity moments are added to the model and closed with HyQMOM [11], the correct behavior will the captured. Starting from the kinetic model, it is straightforward to derive the additional balance equations for these moments [13]. Finally, to improve the numerical solution, high-order schemes (such as is done in [5, 6, 18] for monodisperse particles) will need to be developed for the polydisperse model equations.

Acknowledgments

When preparing this work, ROF was supported by the Fulbright–Tocqueville Distinguished Chair Award and the Jean D'Alembert Senior Professor Chair at the Université de Paris-Saclay. RWH and JWP were supported by AFRL contract FA8651-21-C-0015.

References

[1] P. Andries, K. Aoki, and B. Perthame. A consistent BGK-type model for gas mixtures. Journal of Statistical Physics, 106:993–1018, 2002.

[2] K. Balakrishnan and J. Bellan. High-fidelity modeling and numerical simulation of cratering induced by the interaction of a supersonic jet with a granular bed of solid particles. International Journal of Multiphase Flow, 99:1–29, 2018.

[3] G. K. Batchelor and R. W. O'Brien. Thermal or electrical conduction through a granular material. Proceeding of the Royal Society of London. A. Mathematical and Physical Sciences, 355(1682):313–333, 1977.

[4] E. X. Berry and R. L. Reinhardt. An analysis of cloud drop growth by collection: Part I. Double distributions. Journal of Atmospheric Sciences, 31(7):1814–1824, 1974.
[5] V. Boniou and R. O. Fox. Shock–particle-curtain-interaction study with a hyperbolic two-fluid model: Effect of particle force models. International Journal of Multiphase Flow, 169:104591, 2023.
[6] V. Boniou, R. O. Fox, and F. Laurent. A kinetic-based model for high-speed, monodisperse, fluid–particle flows. HAL preprint https://hal.science/hal-04037062, 2023.
[7] J. Capecelatro and O. Desjardins. An Euler–Lagrange strategy for simulating particle-laden flows. Journal of Computational Physics, 238:1–31, 2013.
[8] C. Cimarelli and K. Genareau. A review of volcanic electrification of the atmosphere and volcanic lightning. Journal of Volcanology and Geothermal Research, 422:107449, 2022.
[9] R. O. Fox. A quadrature-based third-order moment method for dilute gas–particle flows. Journal of Computational Physics, 227(12):6313–6350, 2008.
[10] R. O. Fox. A kinetic-based hyperbolic two-fluid model for binary hard-sphere collisions. Journal of Fluid Mechanics, 877:282–329, 2019.
[11] R. O. Fox and F. Laurent. Hyperbolic quadrature method of moments for the one-dimensional kinetic equation. SIAM Journal on Applied Mathematics, 82(2):750–771, 2022.
[12] R. O. Fox, F. Laurent, and A. Passalacqua. The generalized quadrature method of moments. Journal of Aerosol Science, 167:106096, 2023.
[13] R. O. Fox, F. Laurent, and A. Vié. Conditional hyperbolic quadrature method of moments for kinetic equations. Journal of Computational Physics, 365:269–293, 2018.
[14] R. O. Fox, F. Laurent, and A. Vié. A hyperbolic two-fluid model for compressible flows with arbitrary material-density ratios. Journal of Fluid Mechanics, 903:A5, 2020.
[15] W. Gautschi. Orthogonal Polynomials: Computation and Approximation. Oxford University Press, Oxford, UK, 2004.
[16] W. Gautschi and S. Li. Gauss–Radau and Gauss–Labatto quadratures with double end points. Journal of Computational and Applied Mathematics, 34(3):343–360, 1991.
[17] E. Heulhard de Montigny and A. Llor. Taming the "stiff stiffness" of pressure work and equilibrium in numerical schemes for compressible multi-fluid flows. International Journal of Multiphase Flow, 153:104078, 2022.
[18] R. W. Houim and E. S. Oran. A multiphase model for compressible granular–gaseous flows: formulation and initial tests. Journal of Fluid Mechanics, 789:166–220, 2016.
[19] B. Kong and R. O. Fox. A moment-based kinetic theory model for polydisperse gas–particle flow. Powder Technology, 365:92–105, 2020.
[20] S. Lai, R. W. Houim, and E. S. Oran. Effects of particle size and density on dust dispersion behind a moving shock. Physical Review Fluids, 3:064306, Jun 2018.
[21] F. Laurent and R. O. Fox. Evaluation of the 1-D hyperbolic quadrature method of moments for non-equilibrium flows. ESAIM ProcS, page in press, 2023.
[22] D. L. Marchisio and R. O. Fox. Computational Models for Polydisperse Particulate and Multiphase Systems. Cambridge University Press, Cambridge, UK, 2013.
[23] A. Neri, T. Esposti Ongaro, G. Macedonio, and D. Gidaspow. Multiparticle simulation of collapsing volcanic columns and pyroclastic flow. Journal of Geophysical Research: Solid Earth, 108(B4), 2003.
[24] A. N. Osnes, M. Vartdal, M. Khalloufi, J. Capecelatro, and S. Balachandar. Comprehensive quasi-steady force correlations for compressible flow through random particle suspensions. International Journal of Multiphase Flow, 165:104485, 2023.
[25] J. W. Posey, B. Roque, S. Guhathakurta, and R. W. Houim. Mechanisms of prompt and delayed ignition and combustion of explosively dispersed aluminum powder. Physics of Fluids, 33(11), 2021.
[26] A. Santos, S. B. Yuste, and M. López de Haro. Equation of state of a multicomponent d-dimensional hard-sphere fluid. Molecular Physics, 96:1–5, 1999.
[27] G. S. Shallcross, R. O. Fox, and J. Capecelatro. A volume-filtered description of compressible particle-laden flows. International Journal of Multiphase Flow, 122:103138, 2020.
[28] E. F. Toro. Riemann Solvers and Numerical Methods for Fluid Dynamics. Springer-Verlag, Berlin Heidelberg, 3rd edition, 2009.
[29] A. Vié, F. Doisneau, and M. Massot. On the anisotropic Gaussian velocity closure for inertial-particle laden flows. Communications in Computational Physics, 17(01):1–46, 2015.
[30] M. Wang, Y. Yang, D. Z. Zhang, and S. Balachandar. Numerical calculation of the particle–fluid–particle stress in random arrays of fixed particles. Physical Review Fluids, 6:104306, 2021.
[31] C. Yuan and R. O. Fox. Conditional quadrature method of moments for kinetic equations. Journal of Computational Physics, 230(22):8216–8246, 2011.

Appendix A. Multi-component, inelastic BGK model

Here, we review the kinetic model proposed in [1] for elastic collisions, and extended in [22] to inelastic collisions. First, we present the formulas for a binary system with particles of different diameters, and then these expressions are generalized for a continuous size distribution. By construction, this hard-sphere collision model is exact for velocity moments up to second order.

Appendix A.1. Collisional source terms for binary systems

Following the notation in [22], the multi-component BGK model with inelastic collisions yields source terms for a binary system of the form

$$\begin{aligned} C_1^i &= \kappa_{11}(M_1^0 G_{11}^i - M_1^i) + \kappa_{12}(M_1^0 G_{12}^i - M_1^i), \\ C_2^i &= \kappa_{21}(M_2^0 G_{21}^i - M_2^i) + \kappa_{22}(M_2^0 G_{22}^i - M_2^i). \end{aligned} \tag{A.1}$$

Here, M_1^i (M_2^i) is the mass-weighted velocity moment of order i for a type 1 (2) particle, and C_1^i (C_2^i) is its collisional source term. The Gaussian moments $G_{\alpha\beta}^i$ are found from a Gaussian distribution with mean $\mathbf{u}_{\alpha\beta}$ and covariance matrix $\boldsymbol{\sigma}_{\alpha\beta}$. For example,

$$G_{\alpha\beta}^0 = 1, \;\; G_{\alpha\beta}^1 = \mathbf{u}_{\alpha\beta}, \;\; G_{\alpha\beta}^2 = \mathbf{u}_{\alpha\beta} \otimes \mathbf{u}_{\alpha\beta} + \boldsymbol{\sigma}_{\alpha\beta}. \tag{A.2}$$

It is the definitions of these means and variances that determine the evolution of the velocity moments.

In terms of notation, we first define the mean velocity and granular temperature for each particle type:

$$\mathbf{u}_1 = \frac{M_1^1}{M_1^0}, \;\; \mathbf{u}_2 = \frac{M_2^1}{M_2^0}, \;\; 3\Theta_1 = \frac{M_1^2}{M_1^0} - \mathbf{u}_1 \cdot \mathbf{u}_1, \;\; 3\Theta_2 = \frac{M_2^2}{M_2^0} - \mathbf{u}_2 \cdot \mathbf{u}_2 \tag{A.3}$$

where $\boldsymbol{\sigma}_1 = \Theta_1 \mathbf{I}$ and $\boldsymbol{\sigma}_2 = \Theta_2 \mathbf{I}$ for a Maxwellian distribution (which corresponds to the Euler equation for the particle phase). Also, $\alpha_i/\alpha_p = \xi_i M_i^0/(\rho_e \alpha_p^\star)$ defines the component volume fractions. The particle diameters are d_1 and d_2, and we define $d_{12} = (d_1 + d_2)/2$ and $\chi_{\alpha\beta} = d_{\alpha\beta}/d_\beta$. Thus, $\chi_{11} = \chi_{22} = 1, \chi_{12} = d_{12}/d_2$ and $\chi_{21} = d_{12}/d_1$. Finally, let[12] $\mu_{\alpha\beta} = 2d_\beta^3/(d_\alpha^3 + d_\beta^3)$, so that $\mu_{11} = \mu_{22} = 1$. For later use, we note that $\mu_{\alpha\beta}\chi_{\alpha\beta}^3 = 2d_{\alpha\beta}^3/(d_\alpha^3 + d_\beta^3) = \mu_{\beta\alpha}\chi_{\beta\alpha}^3$.

We can now define the means and variances of the Gaussian distributions:

$$\mathbf{u}_{11} = \mathbf{u}_1, \;\; \mathbf{u}_{12} = \mathbf{u}_1 + \frac{1}{4}(1+e_c)\mu_{12}(\mathbf{u}_2 - \mathbf{u}_1), \;\; \mathbf{u}_{21} = \mathbf{u}_2 + \frac{1}{4}(1+e_c)\mu_{21}(\mathbf{u}_1 - \mathbf{u}_2), \;\; \mathbf{u}_{22} = \mathbf{u}_2, \tag{A.4}$$

and

$$\begin{aligned} &\boldsymbol{\sigma}_{11} = \boldsymbol{\sigma}_1 + \frac{1}{2}(1+e_c)\left[\frac{1}{4}(1+e_c)\mathbf{S}_1 - \boldsymbol{\sigma}_1\right], \;\; \boldsymbol{\sigma}_{12} = \boldsymbol{\sigma}_1 + \frac{1}{2}(1+e_c)\mu_{12}\left[\frac{1}{4}(1+e_c)\mu_{12}\mathbf{S}_{12} - \boldsymbol{\sigma}_1\right], \\ &\boldsymbol{\sigma}_{21} = \boldsymbol{\sigma}_2 + \frac{1}{2}(1+e_c)\mu_{21}\left[\frac{1}{4}(1+e_c)\mu_{21}\mathbf{S}_{12} - \boldsymbol{\sigma}_2\right], \;\; \boldsymbol{\sigma}_{22} = \boldsymbol{\sigma}_2 + \frac{1}{2}(1+e_c)\left[\frac{1}{4}(1+e_c)\mathbf{S}_2 - \boldsymbol{\sigma}_2\right] \end{aligned} \tag{A.5}$$

where (the first equality is for arbitrary distributions, while the second is for a Maxwellian)

$$\mathbf{S}_1 = \boldsymbol{\sigma}_1 + \Theta_1 \mathbf{I} = 2\Theta_1 \mathbf{I}, \;\; \mathbf{S}_{12} = \frac{1}{2}(\boldsymbol{\sigma}_1 + \boldsymbol{\sigma}_2 + E_{12}\mathbf{I}) = \frac{1}{2}(\Theta_1 + \Theta_2 + E_{12})\mathbf{I}, \;\; \mathbf{S}_2 = \boldsymbol{\sigma}_2 + \Theta_2 \mathbf{I} = 2\Theta_2 \mathbf{I}, \tag{A.6}$$

and $E_{12} = \Theta_1 + \Theta_2 + \frac{1}{3}(\mathbf{u}_1 - \mathbf{u}_2)^2$. The collision rates $\kappa_{\alpha\beta}$ are defined by

$$\kappa_{11} = \frac{24 g_{11}\alpha_1 \Theta_1^{1/2}}{\sqrt{\pi} d_1}, \;\; \kappa_{12} = \frac{24 g_{12}\alpha_2 \chi_{12}^3 E_{12}^{1/2}}{\sqrt{2\pi} d_{12}}, \;\; \kappa_{22} = \frac{24 g_{22}\alpha_2 \Theta_2^{1/2}}{\sqrt{\pi} d_2}, \;\; \kappa_{21} = \frac{24 g_{12}\alpha_1 \chi_{21}^3 E_{12}^{1/2}}{\sqrt{2\pi} d_{12}}, \tag{A.7}$$

and are inversely proportional to the collision time τ_c.

Applying the kinetic model to evaluate momentum exchange, we find

$$C_1^1 = \rho_e \alpha_1 \alpha_2 \frac{12 g_{12} E_{12}^{1/2}}{\sqrt{2\pi}} \frac{(1+e_c) d_{12}^2}{(d_1^3 + d_2^3)}(\mathbf{u}_2 - \mathbf{u}_1), \;\; C_2^1 = \rho_e \alpha_1 \alpha_2 \frac{12 g_{12} E_{12}^{1/2}}{\sqrt{2\pi}} \frac{(1+e_c) d_{12}^2}{(d_1^3 + d_2^3)}(\mathbf{u}_1 - \mathbf{u}_2) = -C_1^1. \tag{A.8}$$

As it must be, momentum is conserved during collisions, and there is a net exchange of momentum between particle types with different mean velocities. In the moderately dense regime, momentum exchange will reduce the velocity difference considerably. In general, the velocity difference decreases faster than the granular-temperature difference.

[12] The $\mu_{\alpha\beta}$ are mass ratios, but here the densities of both particle types are equal.

Applying the kinetic model to determine the energy exchange and dissipation, we find

$$C_1^2 = -\rho_e \alpha_1^2 \frac{6 g_{11} \Theta_1^{1/2}}{\sqrt{\pi} d_1}(1-e_c^2)\Theta_1 + \rho_e \alpha_1 \alpha_2 \frac{12 g_{12} E_{12}^{1/2}}{\sqrt{2\pi}} \frac{(1+e_c) d_{12}^2}{(d_1^3+d_2^3)} \left[\frac{1}{4}(1+e_c)\mu_{12} E_{12} - \Theta_1 - \mathbf{u}_1 \cdot (\mathbf{u}_1 - \mathbf{u}_2)\right] \tag{A.9}$$

and

$$C_2^2 = -\rho_e \alpha_2^2 \frac{6 g_{22} \Theta_2^{1/2}}{\sqrt{\pi} d_2}(1-e_c^2)\Theta_2 + \rho_e \alpha_1 \alpha_2 \frac{12 g_{12} E_{12}^{1/2}}{\sqrt{2\pi}} \frac{(1+e_c) d_{12}^2}{(d_1^3+d_2^3)} \left[\frac{1}{4}(1+e_c)\mu_{21} E_{12} - \Theta_2 - \mathbf{u}_2 \cdot (\mathbf{u}_2 - \mathbf{u}_1)\right]. \tag{A.10}$$

The first term on the right-hand side is dissipation of granular energy due to like collisions. The second term is the exchange/dissipation of kinetic energy due to collisions of unlike particles. At equilibrium ($e_c = 1$), $\mathbf{u}_1 = \mathbf{u}_2$ and $\rho_e d_1^3 \Theta_1 = \rho_e d_2^3 \Theta_2$ as expected. Note that because $\mu_{12} + \mu_{21} = 2$, the sum $C_1^2 + C_2^2 \le 0$ where the equality holds for $e_c = 1$. When $e_c < 1$, the lost kinetic energy increases the internal energy of the particle phase. This provides the definition of H_p (without friction) for a binary system:

$$H_p = \rho_e \alpha_p^\star (1-e_c^2) \frac{12}{\alpha_p \sqrt{\pi}} \left(\alpha_1^2 \frac{g_{11}}{d_1} \Theta_1^{3/2} + \alpha_1 \alpha_2 \frac{\sqrt{2} g_{12} d_{12}^2}{(d_1^3+d_2^3)} E_{12}^{3/2} + \alpha_2^2 \frac{g_{22}}{d_2} \Theta_2^{3/2} \right). \tag{A.11}$$

Note that if particle types 1 and 2 are identical, then using $\alpha_p = \alpha_1 + \alpha_2$ reduces the right-hand side to $\rho_e \alpha_p^\star (1 - e_c^2) \frac{12}{\sqrt{\pi}} \alpha_p \frac{g_0}{d_p} \Theta_p^{3/2}$, which is the expected result for monodisperse particles. This property is referred to as the *indifferentiability principle* [1], and it follows from the definition of hard-sphere collisions.

Appendix A.2. Collisional source terms for multi-component systems with binary collisions

For a continuous distribution of particle sizes, we can define the collision term by making use of the NDF, denoted by $n(\xi)$. As in the main text, the moments of the NDF are $\mathcal{M}_i$. We will also need to define the mass-conditioned mean velocity of order i, denoted by $M^i(\xi)$, and the mass-conditioned granular temperature $3\Theta(\xi) = M^2(\xi) - \mathbf{M}^1(\xi) \cdot \mathbf{M}^1(\xi)$ where $\mathbf{M}^1(\xi)$ is the mass-conditioned velocity vector. Formally, the collision model for moment $\mathcal{U}_s^i$ is

$$C_s^i = \beta \int \xi^s C^i(\xi) n(\xi)\, \mathrm{d}\xi \tag{A.12}$$

where, for a given mass ξ, the change in $M^i(\xi)$ is modeled by a mass-conditioned multi-component BGK model:

$$C^i(\xi) = \int \kappa(\xi,\zeta)[G^i(\xi,\zeta) - M^i(\xi)]\, \mathrm{d}\zeta. \tag{A.13}$$

For a binary system, this model must reproduce the results in Appendix A.1. In particular, eq. (A.12) will have the form

$$C_s^i = \beta \xi_1^s M_1^0 C_1^i + \beta \xi_2^s M_2^0 C_2^i \tag{A.14}$$

for $s = 0, 1$; which is the weighted average of the binary collisions terms in eq. (A.1).

The means and variances of the Gaussian distribution function with moments $G_i(\xi,\zeta)$ are defined by

$$\begin{aligned} \mathbf{u}(\xi,\zeta) &= \mathbf{M}^1(\xi) + \frac{1}{4}(1+e_c)\mu_{\xi,\zeta}[\mathbf{M}^1(\zeta) - \mathbf{M}^1(\xi)], \\ \boldsymbol{\sigma}(\xi,\zeta) &= \Theta(\xi)\mathbf{I} + \frac{1}{2}(1+e_c)\mu_{\xi,\zeta}\left[\frac{1}{8}(1+e_c)\mu_{\xi,\zeta}[\Theta(\xi) + \Theta(\zeta) + E(\xi,\zeta)] - \Theta(\xi)\right]\mathbf{I} \end{aligned} \tag{A.15}$$

where $E(\xi,\zeta) = \Theta(\xi) + \Theta(\zeta) + \frac{1}{3}[\mathbf{M}^1(\zeta) - \mathbf{M}^1(\xi)]^2$. Note that when $\zeta = \xi$, these definitions are consistent with self collisions. For the velocity moments up to second order, the Gaussian moments in eq. (A.13) are

$$G^0(\xi,\zeta) = 1, \;\; G^1(\xi,\zeta) = \mathbf{u}(\xi,\zeta), \;\; G^2(\xi,\zeta) = \mathbf{u}(\xi,\zeta) \otimes \mathbf{u}(\xi,\zeta) + \boldsymbol{\sigma}(\xi,\zeta). \tag{A.16}$$

The other parameters in the collision model are generalizations of the binary case:

$$\kappa(\xi,\zeta) = \frac{24 g_0(\xi,\zeta)\alpha(\zeta)\chi^3_{\xi,\zeta}\sqrt{E(\xi,\zeta)}}{\sqrt{2\pi}d_{\xi,\zeta}}, \quad d_{\xi,\zeta} = \frac{1}{2}[d_p(\xi)+d_p(\zeta)],$$
$$\mu_{\xi,\zeta} = \frac{2d_p^3(\zeta)}{d_p^3(\xi)+d_p^3(\zeta)}, \quad \chi_{\xi,\zeta} = \frac{d_{\xi,\zeta}}{d_p(\zeta)}, \quad \alpha(\zeta) = \frac{\zeta}{\rho_p} n(\zeta), \tag{A.17}$$

and $g_0(\xi,\zeta)$ is the radial distribution function given in eq. (46). Likewise, the particle diameter $d_p(\xi)$ is given by eq. (15). Note that for multi-component systems, $H_p = -C_1^2$. In the numerical implementation described in Appendix C, the integrals in eqs. (A.12) and (A.13) are evaluated using Gaussian quadrature, and thus eq. (A.12) is represented by a double summation over all binary collision partners.

Appendix A.3. Collisional pressure

For the collisional pressure P_c, the polydisperse version [10, 19] has the form of eq. (17) with the exact expression for binary hard-sphere collisions given by

$$p_c(\xi) = 2(1+e_c)\int \alpha(\zeta) g_0(\xi,\zeta)\chi^3_{\xi,\zeta}\mu_{\xi,\zeta} y_{\xi,\zeta} E(\xi,\zeta)\,\mathrm{d}\zeta \tag{A.18}$$

where

$$y_{\xi,\zeta} = \begin{cases} \frac{1}{2}\mu_{\xi,\zeta} & \text{if } \xi \le \zeta \\ \frac{1}{2}\mu_{\zeta,\xi} & \text{if } \xi \ge \zeta \end{cases} \quad \Longrightarrow \quad 0.5 \le y_{\xi,\zeta} \le 1. \tag{A.19}$$

In the monodisperse limit, this expression with eq. (17) yields the monodisperse expression. In general, computing P_c with GQMOM requires a double summation over the N mass abscissae:

$$\rho_e \alpha_p^\star P_c = \sum_{i=1}^{N} w_i \xi_i p_c(\xi_i) = 2(1+e_c)\sum_{i=1}^{N}\sum_{j=1}^{N} w_i \xi_i \alpha_j g_{ij}\chi^3_{ij}\mu_{ij} y_{ij} E_{ij} \tag{A.20}$$

where $\alpha_p = \sum_{i=1}^{N}\alpha_i$ and the subscripts ij indicate the masses of the two colliding particles. When all particles have the same mass, velocity and granular temperature, eq. (A.20) reduces to the definition of P_c for monodisperse particles.

The expression for P_c in (A.20), used in the main text, applies the same collisional pressure to each particle type. In contrast, the exact treatment with GQMOM based on (A.18) yields

$$p_{c,i} = 2(1+e_c)\sum_{j=1}^{N}\alpha_j g_{ij}\chi^3_{ij}\mu_{ij} y_{ij} E_{ij} = 2(1+e_c)\left(\alpha_i g_{ii}\Theta_i + \frac{1}{2}\sum_{j<i}\alpha_j g_{ji}\chi^3_{ji}\mu^2_{ji}E_{ji} + \frac{1}{2}\sum_{j>i}\alpha_j g_{ij}\chi^3_{ij}\mu^2_{ij}E_{ij}\right) \tag{A.21}$$

where we have made use of the identity $\chi^3_{ij}\mu_{ij} = \chi^3_{ji}\mu_{ji}$. In the last form, the first term corresponds to self-collisions of type i particles, the second term to collisions with smaller particles, and the third term to collisions with larger particles. For example, for a binary system we have

$$p_{c,1} = 2(1+e_c)\left(\alpha_1 g_{11}\Theta_1 + \frac{1}{2}\alpha_2 g_{12}\chi^3_{12}\mu^2_{12}E_{12}\right), \quad p_{c,2} = 2(1+e_c)\left(\alpha_2 g_{22}\Theta_2 + \frac{1}{2}\alpha_1 g_{12}\chi^3_{12}\mu^2_{12}E_{12}\right), \tag{A.22}$$

which satisfy the indifferentiability principle [1]. The exact collisional pressure for particle types 1 and 2 are $w_1\xi_1 p_{c,1}$ and $w_2\xi_2 p_{c,2}$, respectively, which are different than $\rho_e\alpha_p^\star P_c$.

For an exact treatment, it is straightforward to modify the collisional pressure in the polydisperse kinetic model in (11) to use (A.21). In the particle-phase momentum and kinetic-energy balances in table 4, the following substitutions

are required for the collisional pressure (the frictional pressure contribution remains the same):

$$\mathcal{M}_s P_c \;\to\; \sum_{\beta=1}^{N} w_\beta \xi_\beta^s p_{c,\beta}, \quad \boldsymbol{\mathcal{U}}_s^1 P_c \;\to\; \sum_{\beta=1}^{N} w_\beta \xi_\beta^s \mathbf{u}_p(\xi_\beta) p_{c,\beta}. \tag{A.23}$$

Note that these expressions are in closed form, depending on the known mass-conditioned moments. However, the mathematical form of (A.23) (in particular, the energy flux[13]) makes it more difficult to estimate the eigenvalues of the polydisperse model and, hence, to show that the model is hyperbolic.

Appendix B. Numerical treatment of drag-like exchange terms

The fluid–particle coupling terms (e.g., drag, friction, and heat transfer) are advanced over a time step Δt by employing operator splitting. Using drag as an example, the model equations in table 4 reduce to the following:

$$\begin{aligned}
\partial_t \rho_f \alpha_f^\star &= 0 \\
\partial_t \mathcal{M}_s &= 0 \\
\partial_t \alpha_p &= 0 \\
\partial_t \rho_f \alpha_f^\star \mathbf{u}_f &= \mathcal{A}_1^1 \\
\partial_t \boldsymbol{\mathcal{U}}_s^1 &= -\mathcal{A}_s^1 \\
\partial_t \rho_f \alpha_f^\star E_f &= \mathcal{A}_1^2 - (1-a)\mathcal{B}_1^2 \\
\partial_t \rho_f \alpha_f^\star k_f &= \mathcal{A}_1^f - (2-2a+C_g)\,\mathcal{B}_1^f\, k_f \\
\partial_t \mathcal{K}_s &= -\mathcal{A}_s^2 + (1-a)\mathcal{B}_s^2 \\
\partial_t \mathcal{E}_s &= 0
\end{aligned}
\quad \Longrightarrow \quad
\begin{aligned}
\rho_f \alpha_f^\star &= constant \\
\mathcal{M}_s &= constant \\
\alpha_p &= constant \\
\partial_t \mathbf{u}_f &= \frac{\mathcal{A}_1^1}{\rho_f \alpha_f^\star} \\
\partial_t \boldsymbol{\mathcal{U}}_s^1 &= -\mathcal{A}_s^1 \\
\partial_t E_f + \frac{\partial_t \mathcal{K}_1}{\rho_f \alpha_f^\star} &= 0 \\
\partial_t k_f &= \frac{\mathcal{A}_1^f - (2-2a+C_g)\,\mathcal{B}_1^f\, k_f}{\rho_f \alpha_f^\star} \\
\partial_t \mathcal{K}_s &= -\mathcal{A}_s^2 + (1-a)\mathcal{B}_s^2 \\
\mathcal{E}_s &= constant
\end{aligned} \tag{B.1}$$

so that the mass variables and particle-phase internal energies remain constant. The change in the fluid-phase total energy E_f results from conservation of energy.

The non-constant variables can be rewritten using their mass-conditioned versions. Thus, since the moments $\mathcal{M}_s$ are constant, we have w_β and ξ_β constant so that for $\beta = 1, \ldots, N$ the mean velocities obey

$$\begin{aligned}
\partial_t \mathbf{u}_p(\xi_\beta) &= \frac{1}{\tau_p(\xi_\beta)}[\mathbf{u}_f - \mathbf{u}_p(\xi_\beta)], \\
\partial_t \mathbf{u}_f &= \sum_{\beta=1}^{N} \frac{w_\beta \xi_\beta}{\rho_f \alpha_f^\star \tau_p(\xi_\beta)}[\mathbf{u}_p(\xi_\beta) - \mathbf{u}_f],
\end{aligned} \tag{B.2}$$

and the fluctuating kinetic energies obey

$$\begin{aligned}
\partial_t \Theta_p(\xi_\beta) &= -\frac{2a}{\tau_p(\xi_\beta)}\Theta_p(\xi_\beta) + \frac{4(1-a)}{3\tau_p(\xi_\beta)} k_f, \\
\partial_t k_f &= \sum_{\beta=1}^{N} \frac{w_\beta \xi_\beta}{\rho_f \alpha_f^\star \tau_p(\xi_\beta)} \left[3a\Theta_p(\xi_\beta) - (2-2a+C_g)k_f\right] + \sum_{\beta=1}^{N} \frac{w_\beta \xi_\beta}{\rho_f \alpha_f^\star \tau_p(\xi_\beta)} (\mathbf{u}_p(\xi_\beta) - \mathbf{u}_f)^2.
\end{aligned} \tag{B.3}$$

[13] The energy flux does not have the form of the velocity multiplied by the collisional pressure. It may be possible to approximate the energy flux by such a form, but further work is needed to test such alternatives.

Over the time step Δt, we assume that $\tau_p(\xi_\beta)$ is constant. Thus, eq. (B.2) is a linear ODE with $N + 1$ components and constant coefficients that can be solved analytically using the matrix exponential.

Likewise, eq. (B.3) is also a linear ODE with constant coefficients and a non-negative inhomogeneous term depending on the squared velocity differences that act to increase k_f. The latter are known from solving eq. (B.2). In the analytical solution of eq. (B.3), the inhomogeneous term yields an integral that we approximate with the mid-point rule (i.e., at $\Delta t/2$). Finally, given the updated mass-conditioned particle velocities and granular temperatures, we compute $\mathcal{K}_1(t + \Delta t)$ and then $E_f(t + \Delta t)$ using eq. (B.1). By construction, this method conserves the mixture momentum and total energy, while increasing the fluid-phase internal energy since $a_{min} \leq a \leq 1$. The treatments of friction and heat transfer follow the same procedure.

Appendix C. Numerical treatment of particle–particle collisions

We start by considering the binary system in Appendix A.1 and the mass-conditioned velocity moments of types 1 and 2. In particular, the moments $(M_1^0, M_1^1, M_1^2) = (w_1, w_1\mathbf{u}_1, 2w_1K_1)$ and $(M_2^0, M_2^1, M_2^2) = (w_2, w_2\mathbf{u}_2, 2w_2K_2)$, with volume fractions α_1, α_2, etc. Using time splitting and keeping the collision parameters $\kappa_{\alpha\beta}$ constant over the time step, the change in the moments for each particle type results in a linear ODE system. Most importantly, when extending the algorithm to more than two particle types, the contribution from each collision pair can be solved separately.

Appendix C.1. $N = 2$

Here, we use the following identities:

$$\frac{\kappa_{21}\mu_{21}}{\kappa_{12}\mu_{12}} = \frac{\alpha_1}{\alpha_2}, \quad \mu_{12} + \mu_{21} = 2, \tag{C.1}$$

to eliminate κ_{21} and μ_{21}, respectively. We also have $\alpha_1 + \alpha_2 = \alpha_p$. During collisions, the number of particles does not change so that M_1^0 and M_2^0 are constant. The momentum for each particle type changes by[14]

$$\begin{aligned} \frac{1}{M_1^0}\frac{dM_1^1}{dt} = \kappa_{12}(\mathbf{u}_{12} - \mathbf{u}_1) \quad &\Longrightarrow \quad \frac{d\mathbf{u}_1}{dt} = \kappa_{12}\frac{1}{4}(1 + e_c)\mu_{12}(\mathbf{u}_2 - \mathbf{u}_1), \\ \frac{1}{M_2^0}\frac{dM_2^1}{dt} = \kappa_{21}(\mathbf{u}_{21} - \mathbf{u}_2) \quad &\Longrightarrow \quad \frac{d\mathbf{u}_2}{dt} = \kappa_{21}\frac{1}{4}(1 + e_c)\mu_{21}(\mathbf{u}_1 - \mathbf{u}_2), \end{aligned} \quad \Longrightarrow \quad \frac{d}{dt}\begin{bmatrix}\mathbf{u}_1 \\ \mathbf{u}_2\end{bmatrix} = \mathbf{A}\begin{bmatrix}\mathbf{u}_1 \\ \mathbf{u}_2\end{bmatrix} \tag{C.2}$$

where $\mathbf{u}_{12}$ and $\mathbf{u}_{21}$ are defined in eq. (A.4), and $\mathbf{A}$ is the 2×2 coefficient matrix:

$$\mathbf{A} = -\frac{(1 + e_c)\kappa_{12}\mu_{12}}{4\alpha_2}\begin{bmatrix}\alpha_2 & -\alpha_2 \\ -\alpha_1 & \alpha_1\end{bmatrix}. \tag{C.3}$$

We can observe that the following identities hold:

$$\mathbf{A}\begin{bmatrix}1 \\ 1\end{bmatrix} = \begin{bmatrix}0 \\ 0\end{bmatrix}, \quad \begin{bmatrix}\alpha_1 & \alpha_2\end{bmatrix}\mathbf{A} = \begin{bmatrix}0 & 0\end{bmatrix}. \tag{C.4}$$

The first leads to the steady state $\mathbf{u}_1 = \mathbf{u}_2$, while the second is due to momentum conservation. One eigenvalue of $\mathbf{A}$ is null, while the other is the trace:

$$\lambda_{12} = -\frac{(1 + e_c)\kappa_{12}\mu_{12}\alpha_p}{4\alpha_2} < 0. \tag{C.5}$$

The left/right eigenvectors for the zero eigenvalue are given in eq. (C.4).

Taking $\mathbf{A}$ as constant during the time step, eq. (C.2) gives

$$\begin{bmatrix}\mathbf{u}_1(t) \\ \mathbf{u}_2(t)\end{bmatrix} = e^{\mathbf{A}t}\begin{bmatrix}\mathbf{u}_1(0) \\ \mathbf{u}_2(0)\end{bmatrix} \tag{C.6}$$

[14] Each element of $\mathbf{u}_i$ is multiplied by the same scalar in eq. (C.2), so the vector solution uses the velocity vectors as components.

where $\mathbf{u}_i(0)$ is the velocity before the collision step, and the matrix exponential is

$$e^{\mathbf{A}t} = \frac{1}{\alpha_p}\begin{bmatrix}\alpha_1 + \alpha_2 e^{\lambda_{12}t} & \alpha_2(1 - e^{\lambda_{12}t}) \\ \alpha_1(1 - e^{\lambda_{12}t}) & \alpha_2 + \alpha_1 e^{\lambda_{12}t}\end{bmatrix}. \tag{C.7}$$

In summary, the 2×2 exponential matrix $\exp(\mathbf{A}t)$ gives the change in momentum for each particle type.

For the fluctuating energy change due to collisions, the starting equations are

$$\begin{aligned} 3\frac{d\Theta_1}{dt} &= \kappa_{11}(G_{11}^2 - \mathbf{u}_1 \cdot \mathbf{u}_1 - 3\Theta_1) + \kappa_{12}(G_{12}^2 - \mathbf{u}_1 \cdot \mathbf{u}_1 - 3\Theta_1) - 2\mathbf{u}_1 \cdot \frac{d\mathbf{u}_1}{dt}, \\ 3\frac{d\Theta_2}{dt} &= \kappa_{21}(G_{21}^2 - \mathbf{u}_2 \cdot \mathbf{u}_2 - 3\Theta_2) + \kappa_{22}(G_{22}^2 - \mathbf{u}_2 \cdot \mathbf{u}_2 - 3\Theta_2) - 2\mathbf{u}_2 \cdot \frac{d\mathbf{u}_2}{dt}, \end{aligned} \tag{C.8}$$

where the traces of the Gaussian second-order moments are $G_{\alpha\beta}^2 = \mathbf{u}_{\alpha\beta} \cdot \mathbf{u}_{\alpha\beta} + tr(\boldsymbol{\sigma}_{\alpha\beta})$. In particular,

$$\begin{aligned} G_{11}^2 - \mathbf{u}_1 \cdot \mathbf{u}_1 - 3\Theta_1 &= -\frac{3}{4}(1 - e_c^2)\Theta_1, \\ G_{12}^2 - \mathbf{u}_1 \cdot \mathbf{u}_1 - 3\Theta_1 &= \frac{1}{2}(1 + e_c)\mu_{12}[\mathbf{u}_1 \cdot (\mathbf{u}_2 - \mathbf{u}_1) - 3\Theta_1] + \frac{1}{8}(1 + e_c)^2\mu_{12}^2[3\Theta_1 + 3\Theta_2 + (\mathbf{u}_2 - \mathbf{u}_1)^2], \\ G_{21}^2 - \mathbf{u}_2 \cdot \mathbf{u}_2 - 3\Theta_2 &= \frac{1}{2}(1 + e_c)\mu_{21}[\mathbf{u}_2 \cdot (\mathbf{u}_1 - \mathbf{u}_2) - 3\Theta_2] + \frac{1}{8}(1 + e_c)^2\mu_{21}^2[3\Theta_1 + 3\Theta_2 + (\mathbf{u}_2 - \mathbf{u}_1)^2], \\ G_{22}^2 - \mathbf{u}_2 \cdot \mathbf{u}_2 - 3\Theta_2 &= -\frac{3}{4}(1 - e_c^2)\Theta_2. \end{aligned} \tag{C.9}$$

Thus, the linear system for the granular temperatures is

$$\begin{aligned} \frac{d\Theta_1}{dt} &= -\kappa_{11}\frac{1}{4}(1 - e_c^2)\Theta_1 - \kappa_{12}\frac{1}{2}(1 + e_c)\mu_{12}\Theta_1 + \kappa_{12}\frac{1}{8}(1 + e_c)^2\mu_{12}^2\left[\Theta_1 + \Theta_2 + \frac{1}{3}(\mathbf{u}_2 - \mathbf{u}_1)^2\right], \\ \frac{d\Theta_2}{dt} &= -\kappa_{22}\frac{1}{4}(1 - e_c^2)\Theta_2 - \kappa_{21}\frac{1}{2}(1 + e_c)\mu_{21}\Theta_2 + \kappa_{21}\frac{1}{8}(1 + e_c)^2\mu_{21}^2\left[\Theta_1 + \Theta_2 + \frac{1}{3}(\mathbf{u}_2 - \mathbf{u}_1)^2\right]. \end{aligned} \tag{C.10}$$

This system must be solved with initial conditions $\Theta_1(0)$ and $\Theta_2(0)$.

Using eq. (C.2), we can write the mean-velocity difference as

$$|\mathbf{u}_2(t) - \mathbf{u}_1(t)| = e^{\lambda_{12}t}|\mathbf{u}_2(0) - \mathbf{u}_1(0)|, \tag{C.11}$$

which is non-negative and decreases with t. The analytical solution of eq. (C.10) is then

$$\begin{bmatrix}\Theta_1(t) \\ \Theta_2(t)\end{bmatrix} = e^{\mathbf{B}t}\begin{bmatrix}\Theta_1(0) \\ \Theta_2(0)\end{bmatrix} + [e^{2\lambda_{12}\mathbf{I}t} - e^{\mathbf{B}t}](2\lambda_{12}\mathbf{I} - \mathbf{B})^{-1}\mathbf{D}|\mathbf{u}_2(0) - \mathbf{u}_1(0)|^2 \tag{C.12}$$

where (treating $\kappa_{\alpha\beta}$ as constants over the time step) $\mathbf{B} = \mathbf{B}_\theta + \mathbf{B}_{12}$,

$$\mathbf{B}_\theta = -\frac{1}{4}(1 - e_c^2)\begin{bmatrix}\kappa_{11} & 0 \\ 0 & \kappa_{22}\end{bmatrix}, \tag{C.13}$$

$$\mathbf{B}_{12} = -\frac{(1 + e_c)\kappa_{12}\mu_{12}}{2\alpha_2}\begin{bmatrix}\alpha_2 - \alpha_2\frac{1+e_c}{4}\mu_{12} & -\alpha_2\frac{1+e_c}{4}\mu_{12} \\ -\alpha_1\frac{1+e_c}{4}\mu_{21} & \alpha_1 - \alpha_1\frac{1+e_c}{4}\mu_{21}\end{bmatrix}, \tag{C.14}$$

and

$$\mathbf{D} = \frac{(1 + e_c)^2\kappa_{12}\mu_{12}}{24\alpha_2}\begin{bmatrix}\alpha_2\mu_{12} \\ \alpha_1\mu_{21}\end{bmatrix}. \tag{C.15}$$

When $e_c < 1$, the total energy of the particle phase will decrease, and the lost energy is added to the internal energy. When $e_c = 1$, $\mathbf{B}$ has a null eigenvalue, reflecting the conservation of total granular energy, and the other is equal to the

trace.

Appendix C.2. $N = 3$

For $N = 3$ and larger, the semi-analytical solutions follow the same general pattern, which accounts for all possible pairwise collisions. For $N = 3$, the six collision pairs are (1,1), (1,2), (1,3), (2,2), (2,3) and (3,3). Here, we use the following identities:

$$\frac{\kappa_{21}\mu_{21}}{\kappa_{12}\mu_{12}} = \frac{\alpha_1}{\alpha_2}, \quad \frac{\kappa_{31}\mu_{31}}{\kappa_{13}\mu_{13}} = \frac{\alpha_1}{\alpha_3}, \quad \frac{\kappa_{32}\mu_{32}}{\kappa_{23}\mu_{23}} = \frac{\alpha_2}{\alpha_3}, \quad \mu_{12} + \mu_{21} = 2, \quad \mu_{13} + \mu_{31} = 2, \quad \mu_{23} + \mu_{32} = 2,$$

to eliminate κ_{21}, κ_{31}, κ_{32}, μ_{21}, μ_{31}, μ_{32}, respectively. For $N = 3$, the momentum balance yields

$$\frac{d}{dt}\begin{bmatrix}\mathbf{u}_1\\ \mathbf{u}_2\\ \mathbf{u}_3\end{bmatrix} = \mathbf{A}\begin{bmatrix}\mathbf{u}_1\\ \mathbf{u}_2\\ \mathbf{u}_3\end{bmatrix} \tag{C.16}$$

where $\mathbf{A} = \mathbf{A}_{12} + \mathbf{A}_{13} + \mathbf{A}_{23}$,

$$\begin{gathered}\mathbf{A}_{12} = \frac{(1+e_c)\kappa_{12}\mu_{12}}{4\alpha_2}\begin{bmatrix}-\alpha_2 & \alpha_2 & 0\\ \alpha_1 & -\alpha_1 & 0\\ 0 & 0 & 0\end{bmatrix}, \ \mathbf{A}_{13} = \frac{(1+e_c)\kappa_{13}\mu_{13}}{4\alpha_3}\begin{bmatrix}-\alpha_3 & 0 & \alpha_3\\ 0 & 0 & 0\\ \alpha_1 & 0 & -\alpha_1\end{bmatrix},\\ \mathbf{A}_{23} = \frac{(1+e_c)\kappa_{23}\mu_{23}}{4\alpha_3}\begin{bmatrix}0 & 0 & 0\\ 0 & -\alpha_3 & \alpha_3\\ 0 & \alpha_2 & -\alpha_2\end{bmatrix}.\end{gathered} \tag{C.17}$$

We can observe that the following identities hold:

$$\mathbf{A}\begin{bmatrix}1\\ 1\\ 1\end{bmatrix} = \begin{bmatrix}0\\ 0\\ 0\end{bmatrix}, \quad \begin{bmatrix}\alpha_1 & \alpha_2 & \alpha_3\end{bmatrix}\mathbf{A} = \begin{bmatrix}0 & 0 & 0\end{bmatrix}. \tag{C.18}$$

The first leads to the steady state $\mathbf{u}_1 = \mathbf{u}_2 = \mathbf{u}_2$, while the second represents momentum conservation. Due to conservation of momentum, one eigenvalue of $\mathbf{A}$ is null. Again, the right/left eigenvectors of the zero eigenvalue appear in eq. (C.18).

Taking $\mathbf{A}$ as constant during the time step, eq. (C.16) gives

$$\begin{bmatrix}\mathbf{u}_1(t)\\ \mathbf{u}_2(t)\\ \mathbf{u}_3(t)\end{bmatrix} = e^{\mathbf{A}t}\begin{bmatrix}\mathbf{u}_1(0)\\ \mathbf{u}_2(0)\\ \mathbf{u}_3(0)\end{bmatrix}. \tag{C.19}$$

In summary, it is necessary to compute the 3×3 exponential matrix $\exp(\mathbf{A}t)$ to find the change in momentum for each particle type.

For the velocity differences $\Delta_{ij}(t) = \mathbf{u}_i(t) - \mathbf{u}_j(t)$, we define the matrices

$$\mathbf{P} = \begin{bmatrix}1 & -1 & 0\\ 1 & 0 & -1\\ \alpha_1 & \alpha_2 & \alpha_3\end{bmatrix}, \quad \begin{bmatrix}X_{12}(t)\\ X_{13}(t)\\ C_3\end{bmatrix} = \mathbf{P}\begin{bmatrix}\mathbf{u}_1(t)\\ \mathbf{u}_2(t)\\ \mathbf{u}_3(t)\end{bmatrix} = \begin{bmatrix}\Delta_{12}(t)\\ \Delta_{13}(t)\\ \alpha_1\mathbf{u}_1(t) + \alpha_2\mathbf{u}_2(t) + \alpha_3\mathbf{u}_3(t)\end{bmatrix} \tag{C.20}$$

where C_3 is constant due to conservation of momentum. Using the change of variables and $\mathbf{PAP}^{-1}$ with eq. (C.16) yields

$$\frac{d\mathbf{X}}{dt} = \hat{\mathbf{A}}\mathbf{X}, \quad \hat{\mathbf{A}} = -\frac{1+e_c}{4}\begin{bmatrix}\frac{\alpha_1+\alpha_2}{\alpha_2}\kappa_{12}\mu_{12} + \kappa_{23}\mu_{23} & \kappa_{13}\mu_{13} - \kappa_{23}\mu_{23}\\ \kappa_{12}\mu_{12} - \frac{\alpha_2}{\alpha_3}\kappa_{23}\mu_{23} & \frac{\alpha_1+\alpha_3}{\alpha_3}\kappa_{13}\mu_{13} + \frac{\alpha_2}{\alpha_3}\kappa_{23}\mu_{23}\end{bmatrix}, \tag{C.21}$$

where the two eigenvalues of $\hat{\mathbf{A}}$ are negative. Thus, the analytical solution is

$$\mathbf{X}(t) = \begin{bmatrix} \Delta_{12}(t) \\ \Delta_{13}(t) \end{bmatrix} = e^{\hat{\mathbf{A}}t} \begin{bmatrix} \Delta_{12}(0) \\ \Delta_{13}(0) \end{bmatrix}, \tag{C.22}$$

and $\Delta_{23}(t) = \Delta_{12}(t) - \Delta_{13}(t)$. In summary, it is necessary to compute the 2×2 exponential matrix $\exp(\hat{\mathbf{A}}t)$ to find the velocity differences, which can be done analytically.

The linear system for the granular temperatures is

$$\frac{d}{dt} \begin{bmatrix} \Theta_1 \\ \Theta_2 \\ \Theta_3 \end{bmatrix} = \mathbf{B} \begin{bmatrix} \Theta_1 \\ \Theta_2 \\ \Theta_3 \end{bmatrix} + \mathbf{D}_{12}\Delta_{12}^2(t) + \mathbf{D}_{13}\Delta_{13}^2(t) + \mathbf{D}_{23}\Delta_{23}^2(t) \tag{C.23}$$

where $\mathbf{B} = \mathbf{B}_\theta + \mathbf{B}_{12} + \mathbf{B}_{13} + \mathbf{B}_{23}$,

$$\mathbf{B}_\theta = -\frac{1 - e_c^2}{4} \begin{bmatrix} \kappa_{11} & 0 & 0 \\ 0 & \kappa_{22} & 0 \\ 0 & 0 & \kappa_{33} \end{bmatrix}, \tag{C.24}$$

$$\mathbf{B}_{12} = -\frac{(1 + e_c)\kappa_{12}\mu_{12}}{2\alpha_2} \begin{bmatrix} \alpha_2 - \alpha_2 \frac{1+e_c}{4}\mu_{12} & -\alpha_2 \frac{1+e_c}{4}\mu_{12} & 0 \\ -\alpha_1 \frac{1+e_c}{4}\mu_{21} & \alpha_1 - \alpha_1 \frac{1+e_c}{4}\mu_{21} & 0 \\ 0 & 0 & 0 \end{bmatrix}, \tag{C.25}$$

$$\mathbf{B}_{13} = -\frac{(1 + e_c)\kappa_{13}\mu_{13}}{2\alpha_3} \begin{bmatrix} \alpha_3 - \alpha_3 \frac{1+e_c}{4}\mu_{13} & 0 & -\alpha_3 \frac{1+e_c}{4}\mu_{13} \\ 0 & 0 & 0 \\ -\alpha_1 \frac{1+e_c}{4}\mu_{31} & 0 & \alpha_1 - \alpha_1 \frac{1+e_c}{4}\mu_{31} \end{bmatrix}, \tag{C.26}$$

$$\mathbf{B}_{23} = -\frac{(1 + e_c)\kappa_{23}\mu_{23}}{2\alpha_3} \begin{bmatrix} 0 & 0 & 0 \\ 0 & \alpha_3 - \alpha_3 \frac{1+e_c}{4}\mu_{23} & -\alpha_3 \frac{1+e_c}{4}\mu_{23} \\ 0 & -\alpha_2 \frac{1+e_c}{4}\mu_{32} & \alpha_2 - \alpha_2 \frac{1+e_c}{4}\mu_{32} \end{bmatrix}, \tag{C.27}$$

and

$$\mathbf{D}_{12} = \frac{(1 + e_c)^2\kappa_{12}\mu_{12}}{24\alpha_2} \begin{bmatrix} \alpha_2\mu_{12} \\ \alpha_1\mu_{21} \\ 0 \end{bmatrix}, \ \mathbf{D}_{13} = \frac{(1 + e_c)^2\kappa_{13}\mu_{13}}{24\alpha_3} \begin{bmatrix} \alpha_3\mu_{13} \\ 0 \\ \alpha_1\mu_{31} \end{bmatrix}, \ \mathbf{D}_{23} = \frac{(1 + e_c)^2\kappa_{23}\mu_{23}}{24\alpha_3} \begin{bmatrix} 0 \\ \alpha_3\mu_{23} \\ \alpha_2\mu_{32} \end{bmatrix}. \tag{C.28}$$

The eigenvalues of $\mathbf{B}$ are negative if $e_c < 1$, and, if $e_c = 1$ due to conservation of energy, one of them is null with left eigenvector $[\alpha_1 \ \alpha_2 \ \alpha_3]$.

The analytical solution of eq. (C.23) is

$$\begin{bmatrix} \Theta_1(t) \\ \Theta_2(t) \\ \Theta_3(t) \end{bmatrix} = e^{\mathbf{B}t} \begin{bmatrix} \Theta_1(0) \\ \Theta_2(0) \\ \Theta_3(0) \end{bmatrix} + \int_0^t e^{\mathbf{B}(t-s)} [\mathbf{D}_{12}\Delta_{12}^2(s) + \mathbf{D}_{13}\Delta_{13}^2(s) + \mathbf{D}_{23}\Delta_{23}^2(s)] \, \mathrm{d}s. \tag{C.29}$$

Unlike with eq. (C.12), evaluating the source terms in eq. (C.29) is complicated. However, to ensure conservation of total energy for $e_c = 1$, this evaluation must be exact. The 3×3 exponential matrix $\exp(\mathbf{B}t)$ is also difficult to find analytically. Thus, it may be necessary to solve eq. (C.23) numerically. For this purpose, if the time step Δt is small, the midpoint formula

$$\begin{bmatrix} \Theta_1(\Delta t) \\ \Theta_2(\Delta t) \\ \Theta_3(\Delta t) \end{bmatrix} = e^{\mathbf{B}\Delta t} \begin{bmatrix} \Theta_1(0) \\ \Theta_2(0) \\ \Theta_3(0) \end{bmatrix} + e^{\frac{1}{2}\mathbf{B}\Delta t} [\mathbf{D}_{12}\Delta_{12}^2(\Delta t/2) + \mathbf{D}_{13}\Delta_{13}^2(\Delta t/2) + \mathbf{D}_{23}\Delta_{23}^2(\Delta t/2)]\Delta t \tag{C.30}$$

may suffice. Numerical tests with $e_c = 1$ show a kinetic energy difference of less than one percent for parameters representing the target application.

Appendix C.3. Particle-phase internal energy change due to binary collisions

When $e_c < 1$, particle-phase kinetic energy is transformed to internal energy e_p during collisions. Let e_i be the internal energy of type i particles. During binary collisions, we assume $e_i + 3\Theta_i + u_i^2$ is constant.[15] For $N = 3$, the governing equation for $\alpha_i e_i$ during binary collisions is

$$\frac{d}{dt}\begin{bmatrix}\alpha_1 e_1\\ \alpha_2 e_2\\ \alpha_3 e_3\end{bmatrix} = \hat{\mathbf{B}}\begin{bmatrix}\Theta_1(t)\\ \Theta_2(t)\\ \Theta_3(t)\end{bmatrix} + \hat{\mathbf{D}}_{12}\Delta_{12}^2(t) + \hat{\mathbf{D}}_{13}\Delta_{13}^2(t) + \hat{\mathbf{D}}_{23}\Delta_{23}^2(t) \tag{C.31}$$

where $\hat{\mathbf{B}} = \hat{\mathbf{B}}_\theta + \hat{\mathbf{B}}_{12} + \hat{\mathbf{B}}_{13} + \hat{\mathbf{B}}_{23}$,

$$\hat{\mathbf{B}}_\theta = \frac{3(1-e_c^2)}{4}\begin{bmatrix}\alpha_1\kappa_{11} & 0 & 0\\ 0 & \alpha_2\kappa_{22} & 0\\ 0 & 0 & \alpha_3\kappa_{33}\end{bmatrix}, \tag{C.32}$$

$$\hat{\mathbf{B}}_{12} = \frac{3(1-e_c^2)\alpha_1\kappa_{12}\mu_{12}}{8}\begin{bmatrix}\mu_{12} & \mu_{12} & 0\\ \mu_{21} & \mu_{21} & 0\\ 0 & 0 & 0\end{bmatrix}, \tag{C.33}$$

$$\hat{\mathbf{B}}_{13} = \frac{3(1-e_c^2)\alpha_1\kappa_{13}\mu_{13}}{8}\begin{bmatrix}\mu_{13} & 0 & \mu_{13}\\ 0 & 0 & 0\\ \mu_{31} & 0 & \mu_{31}\end{bmatrix}, \tag{C.34}$$

$$\hat{\mathbf{B}}_{23} = \frac{3(1-e_c^2)\alpha_2\kappa_{23}\mu_{23}}{8}\begin{bmatrix}0 & 0 & 0\\ 0 & \mu_{23} & \mu_{23}\\ 0 & \mu_{32} & \mu_{32}\end{bmatrix}, \tag{C.35}$$

and

$$\hat{\mathbf{D}}_{12} = \frac{(1-e_c^2)\alpha_1\kappa_{12}\mu_{12}}{8}\begin{bmatrix}\mu_{12}\\ \mu_{21}\\ 0\end{bmatrix},\ \hat{\mathbf{D}}_{13} = \frac{(1-e_c^2)\alpha_1\kappa_{13}\mu_{13}}{8}\begin{bmatrix}\mu_{13}\\ 0\\ \mu_{31}\end{bmatrix},\ \hat{\mathbf{D}}_{23} = \frac{(1-e_c^2)\alpha_2\kappa_{23}\mu_{23}}{8}\begin{bmatrix}0\\ \mu_{23}\\ \mu_{32}\end{bmatrix}. \tag{C.36}$$

Note that all matrices are null when $e_c = 1$ as expected, and the matrices $\hat{\mathbf{B}}_{ij}$ have two zero and one positive eigenvalue. Thus, the right-hand side of eq. (C.31) is non-negative, which ensures that the internal energies never decrease. In the simulation code, over a small time step the solution to eq. (C.31) is approximated by

$$\begin{bmatrix}\alpha_1 e_1(\Delta t)\\ \alpha_2 e_2(\Delta t)\\ \alpha_3 e_3(\Delta t)\end{bmatrix} = \begin{bmatrix}\alpha_1 e_1(0)\\ \alpha_2 e_2(0)\\ \alpha_3 e_3(0)\end{bmatrix} + \frac{1}{2}\hat{\mathbf{B}}\begin{bmatrix}\Theta_1(\Delta t) + \Theta_1(0)\\ \Theta_2(\Delta t) + \Theta_2(0)\\ \Theta_3(\Delta t) + \Theta_3(0)\end{bmatrix}\Delta t + [\hat{\mathbf{D}}_{12}\Delta_{12}^2(\Delta t/2) + \hat{\mathbf{D}}_{13}\Delta_{13}^2(\Delta t/2) + \hat{\mathbf{D}}_{23}\Delta_{23}^2(\Delta t/2)]\Delta t \tag{C.37}$$

where eq. (C.30) is used to find $\Theta_i(\Delta t)$. The increase in the particle-phase internal energy is found from the identity $\alpha_p e_p = \alpha_1 e_1 + \alpha_2 e_2 + \alpha_3 e_3$.

The extension to an arbitrary number of particle sizes follows the same pattern as for $N = 3$, i.e., one must account for binary collisions for each pair of particle sizes. In our code, the algorithm is implemented for four particle sizes ($N = 4$). Given the number of particle pairs, the computational cost for collisions increases significantly with increasing N.

Appendix C.4. Correction algorithm for conservation of particle-phase total energy

Due to numerical errors in eqs. (C.30) and (C.37), the particle-phase total energy will not be exactly conserved. Thus, at each time step, either the kinetic energies $\Theta_i(\Delta t)$ or the internal energies $e_i(\Delta t)$ are multiplied by a correction factor to ensure total-energy conservation. Specifically, if the total energy has increased during the time step, then the kinetic energies are decreased; otherwise, if the total energy has decreased, then the internal energies are increased to

[15] This assumption is sufficient, but not necessary since the lost kinetic energy could be distributed differently, depending on the particle mass. Here, we assume that the kinetic energy lost by type i stays with type i in the form of internal energy.

ensure conservation. Numerical tests with $e_c = 1$ (i.e., no change is internal energies) have shown that this correction scheme performs as expected, i.e., the total energy at the end of the time step is always too large so that the kinetic energies are decreased. In any case, this scheme ensures that the internal energies can never decrease during collisions. Moreover, without a correction scheme, the kinetic energies can increase nonphysically with time and eventually can cause a simulation to fail.

Appendix C.5. Treatment of frictional collisions

For frictional collisions, the kinetic energy lost by particles is redistributed as internal energy proportional to the mass of each particle type. The increase in particle-phase internal energy due to friction is found from

$$\frac{de_p}{dt} = -\frac{dK_p}{dt} = \frac{1}{\tau_f}\frac{3}{2}\Theta_p. \tag{C.38}$$

Since the particle density is constant, the mass fraction is proportional to the volume fraction. Thus, if $\Delta\mathcal{E}_s$ is the change of $\mathcal{E}_s$ over the time step, then $\Delta\mathcal{E}_s = -\mathcal{M}_s\Delta K_p$ where $\Delta K_p \leq 0$ is the change in particle-phase kinetic energy.

Appendix D. Numerical treatment of buoyancy-like exchange terms

Time splitting is used to update the buoyancy-like exchange terms in the momentum and energy balances. For a monodisperse particle phase, this amounts to solving the system

$$\begin{aligned} \partial_t \rho_e \alpha_p^\star &= 0, \\ \partial_t \rho_e \alpha_p^\star \mathbf{u}_p &= -\mathbf{B}, \\ \partial_t \rho_e \alpha_p^\star K_p &= -\mathbf{B}\cdot\mathbf{u}_p \\ \partial_t \rho_e \alpha_p^\star e_p &= 0 \end{aligned} \tag{D.1}$$

where the vector

$$\mathbf{B} = \alpha_p^\star(\partial_{\mathbf{x}}\hat{p}_f + \mathbf{F}_{pf}) + \partial_{\mathbf{x}}\cdot\mathbf{P}_{pfp} \tag{D.2}$$

is held constant over the time step. Given that $\rho_e\alpha_p^\star$ is constant and $K_p = \frac{1}{2}(3\Theta_p + u_p^2)$, we can observe that the second-order central moment Θ_p is also constant over the time step. The same is true for higher-order central velocity moments, i.e., they remain constant when only the buoyancy-like exchange terms are included. This observation has important implications on the numerical integration because only the mean velocity, and not the central moments, will change over a time step.

Using a Euler time step, and denoting the value at the end of the time step as $(\cdot)^*$, we find (in conservative form)

$$\begin{aligned} (\rho_e\alpha_p^\star)^* &= \rho_e\alpha_p^\star, \\ (\rho_e\alpha_p^\star\mathbf{u}_p)^* &= \rho_e\alpha_p^\star\mathbf{u}_p - \mathbf{B}\Delta t, \\ (\rho_e\alpha_p^\star K_p)^* &= \rho_e\alpha_p^\star K_p + \frac{1}{2}\rho_e\alpha_p^\star\left(\mathbf{u}_p^*\cdot\mathbf{u}_p^* - \mathbf{u}_p\cdot\mathbf{u}_p\right), \\ (\rho_e\alpha_p^\star e_p)^* &= \rho_e\alpha_p^\star e_p, \end{aligned} \tag{D.3}$$

which conserves the central moment Θ_p for arbitrary Δt. For the fluid phase, the corresponding equations are

$$\begin{aligned} \partial_t \rho_f\alpha_f^\star &= 0, \\ \partial_t \rho_f\alpha_f^\star\mathbf{u}_f &= \mathbf{B}, \\ \partial_t \rho_f\alpha_f^\star E_f &= \mathbf{B}\cdot\mathbf{u}_p, \end{aligned} \quad\Longrightarrow\quad \begin{aligned} (\rho_f\alpha_f^\star)^* &= \rho_f\alpha_f^\star, \\ (\rho_f\alpha_f^\star\mathbf{u}_f)^* &= \rho_f\alpha_f^\star\mathbf{u}_f + \rho_e\alpha_p^\star(\mathbf{u}_p - \mathbf{u}_p^*), \\ (\rho_f\alpha_f^\star E_f)^* &= \rho_f\alpha_f^\star E_f + \rho_e\alpha_p^\star(K_p - K_p^*), \end{aligned} \tag{D.4}$$

which conserve the mass, momentum and total energy of the two phases. Note that with higher-order time accuracy beyond Euler, only the formula for the updated velocity $\mathbf{u}_p^*$ will change.

For the polydisperse case, the integration formulas for mass-conditioned velocity moments are analogous to eq. (D.3). Defining the second-order central moment $3\mathcal{M}_s\Theta_s = 2\mathcal{K}_s - \boldsymbol{\mathcal{U}}_s^1 \cdot \boldsymbol{\mathcal{U}}_s^1/\mathcal{M}_s$, this can be shown for $s = 0, 1, \ldots, N-1$ starting from

$$\begin{aligned} \partial_t \mathcal{M}_s &= 0, & \mathcal{M}_s^* &= \mathcal{M}_s, \\ \partial_t \boldsymbol{\mathcal{U}}_s^1 &= -\frac{\mathcal{M}_s}{\mathcal{M}_1}\mathbf{B}, \quad \Longrightarrow & \boldsymbol{\mathcal{U}}_s^{1*} &= \boldsymbol{\mathcal{U}}_s^1 - \frac{\mathcal{M}_s}{\mathcal{M}_1}\mathbf{B}\Delta t, \\ \partial_t \mathcal{K}_s &= -\frac{1}{\mathcal{M}_1}\mathbf{B}\cdot\boldsymbol{\mathcal{U}}_s^1, & \mathcal{K}_s^* &= \mathcal{K}_s + \frac{1}{2\mathcal{M}_s}\left(\boldsymbol{\mathcal{U}}_s^{1*}\cdot\boldsymbol{\mathcal{U}}_s^{1*} - \boldsymbol{\mathcal{U}}_s^1\cdot\boldsymbol{\mathcal{U}}_s^1\right). \end{aligned} \tag{D.5}$$

Note that the central moment Θ_s is constant over the time step. For the fluid phase, eq. (D.4) again conserves the overall mass, momentum and energy.

More generally, by defining the vector

$$\mathbf{C}_s = \frac{1}{\mathcal{M}_s}(\boldsymbol{\mathcal{U}}_s^{1*} - \boldsymbol{\mathcal{U}}_s^1) \quad \Longleftrightarrow \quad \boldsymbol{\mathcal{U}}_s^{1*} = \boldsymbol{\mathcal{U}}_s^1 + \mathcal{M}_s\mathbf{C}_s, \tag{D.6}$$

we can write

$$\frac{1}{\mathcal{M}_s}\left(\boldsymbol{\mathcal{U}}_s^{1*}\cdot\boldsymbol{\mathcal{U}}_s^{1*} - \boldsymbol{\mathcal{U}}_s^1\cdot\boldsymbol{\mathcal{U}}_s^1\right) = 2\boldsymbol{\mathcal{U}}_s^1\cdot\mathbf{C}_s + \mathcal{M}_s\mathbf{C}_s\cdot\mathbf{C}_s \tag{D.7}$$

so that

$$\mathcal{K}_s^* = \mathcal{K}_s^2 + \boldsymbol{\mathcal{U}}_s^1\cdot\mathbf{C}_s + \frac{1}{2}\mathcal{M}_s\mathbf{C}_s\cdot\mathbf{C}_s; \tag{D.8}$$

or, for the full second-order velocity tensor,

$$\boldsymbol{\mathcal{U}}_s^{2*} = \boldsymbol{\mathcal{U}}_s^2 + \boldsymbol{\mathcal{U}}_s^1\otimes\mathbf{C}_s + \mathbf{C}_s\otimes\boldsymbol{\mathcal{U}}_s^1 + \mathcal{M}_s\mathbf{C}_s\otimes\mathbf{C}_s. \tag{D.9}$$

Similar formulas can be derived for higher-order moments, and preserve the central-moment velocity tensors during the time step for arbitrary Δt.

Appendix E. Numerical treatment of added-mass source terms

Time splitting is used to update the added-mass source terms. For the particle phase, this amounts to solving a linear system of ODEs:

$$\begin{aligned} \partial_t\mathcal{M}_s &= C_\xi\mathcal{M}_s \\ \partial_t\mathcal{E}_s &= C_u e_f\mathcal{M}_s + (C_\xi - C_u)\mathcal{E}_s \\ \partial_t\boldsymbol{\mathcal{U}}_s^1 &= C_u\mathbf{u}_f\mathcal{M}_s + (C_\xi - C_u)\boldsymbol{\mathcal{U}}_s^1 \\ \partial_t\mathcal{K}_s &= C_u K_f\mathcal{M}_s + (C_\xi - C_u)\mathcal{K}_s \end{aligned} \quad \Longrightarrow \quad \begin{aligned} \partial_t\mathcal{M}_s &= C_\xi\mathcal{M}_s \\ \partial_t\left(\frac{\mathcal{E}_s}{\mathcal{M}_s}\right) &= C_u e_f - C_u\left(\frac{\mathcal{E}_s}{\mathcal{M}_s}\right) \\ \partial_t\left(\frac{\boldsymbol{\mathcal{U}}_s^1}{\mathcal{M}_s}\right) &= C_u\mathbf{u}_f - C_u\left(\frac{\boldsymbol{\mathcal{U}}_s^1}{\mathcal{M}_s}\right) \\ \partial_t\left(\frac{\mathcal{K}_s}{\mathcal{M}_s}\right) &= C_u K_f - C_u\left(\frac{\mathcal{K}_s}{\mathcal{M}_s}\right) \end{aligned} \tag{E.1}$$

with e_f, $\mathbf{u}_f$, K_f, C_ξ, and C_u held constant. The analytical solution for the size moments at time t is

$$\mathcal{M}_s(t) = \mathcal{M}_s(0)\, e^{C_\xi t} \tag{E.2}$$

with $s = 0, \frac{1}{2}, 1, \frac{3}{2}, 2, \frac{5}{2}, 3$. As expected, since all size moments change by the same factor, this step leaves the mass abscissae unchanged. The change of mass in the fluid phase over the time step Δt is then $\mathcal{M}_1(0) - \mathcal{M}_1(\Delta t)$.

For the internal energy, momentum, and kinetic energy ($s = 0, 1, 2, 3$), the analytical solutions are

$$\frac{\mathcal{E}_s(t)}{\mathcal{M}_s(t)} = \frac{\mathcal{E}_s(0)}{\mathcal{M}_s(0)}e^{-C_u t} + e_f\left(1 - e^{-C_u t}\right), \tag{E.3}$$

$$\frac{\boldsymbol{\mathcal{U}}_s^1(t)}{\mathcal{M}_s(t)} = \frac{\boldsymbol{\mathcal{U}}_s^1(0)}{\mathcal{M}_s(0)} e^{-C_u t} + \mathbf{u}_f \left(1 - e^{-C_u t}\right) \tag{E.4}$$

and

$$\frac{\mathcal{K}_s(t)}{\mathcal{M}_s(t)} = \frac{\mathcal{K}_s(0)}{\mathcal{M}_s(0)} e^{-C_u t} + K_f \left(1 - e^{-C_u t}\right). \tag{E.5}$$

The change in momentum and total energy in the fluid phase are computed in the same manner as for mass with $s = 1$.

Appendix F. Generalized CQMOM

Roughly speaking, generalized CQMOM (GCQMOM) is employed when $N_g > N$ quadrature nodes are used to find mass-conditioned moments from N mass-weighted moments. In this case, we must find an interpolation scheme in mass phase space that satisfies the N mass-weighted moments appearing on the right-hand side of the linear system used with CQMOM. Because $N_g > N$, the direct application of CQMOM is under determined (more conditional moments than constraints); however, we can obtain a fully determined linear system by interpolating between the N mass-conditioned moments found at the N quadrature-method-of-moments (QMOM) nodes. Recall that QMOM uses $2N$ moments that satisfy [22]

$$\mathcal{M}_s = \sum_{\alpha=1}^{N} \hat{w}_\alpha \hat{\xi}_\alpha^s, \quad s \in (0, 1, \ldots, 2N-1) \tag{F.1}$$

for the mass moments (or equivalent equations for the half-order moments). Hereinafter, we will describe the method using the conserved mass moments $(\mathcal{M}_0, \mathcal{M}_1, \ldots, \mathcal{M}_{N_s})$ with $N_s \geq 2N$; however, it is straightforward to use size or half-order moments. Given the conserved moments, GQMOM provides $N_g > N$ quadrature nodes. In the following, we use a hat to indicate the weights and abscissae found with QMOM, and those from GQMOM are shown without a hat. Keeping this goal in mind, the basic idea behind GCQMOM is as follows.

Appendix F.1. Definition of GCQMOM

For arbitrary $N_g > N$, the GQMOM representation for mass ξ can be combined with CQMOM for a fixed number N of QMOM mass abscissas. (Recall that N fixes the number of velocity moments needed for the polydisperse model.) We assume that the mass moments, denoted here by $\langle \xi^k \rangle = \mathcal{M}_k$, are known for $k = 0, 1, \ldots, 2N-1$. Applying QMOM with these mass moments gives the N weights $\hat{w}_\alpha$ and N mass abscissae $\hat{\xi}_\alpha$. Let ϕ denote a particle property other than mass (e.g., velocity, internal energy, etc.). As described in the main text, for mass conditioning CQMOM uses the joint moments, denoted here by $\langle \phi \xi^k \rangle$, to find an approximation for the conditional expected value of ϕ given ξ, denoted by $\langle \phi | \xi \rangle$. Finally, we assume that $\phi_0 = \langle \phi | \xi = 0 \rangle$ is known (e.g., smallest particles have properties in equilibrium with fluid phase), while $\phi_\alpha = \langle \phi | \xi = \hat{\xi}_\alpha \rangle$ for $\alpha = 1, \ldots, N$ must be found from the N mass-weighted moments $\langle \phi \xi^k \rangle$ with $k = 0, 1, \ldots, N-1$.

The main difference between CQMOM and GCQMOM is that the latter provides values for $\langle \phi | \xi \rangle$ in between the QMOM quadrature nodes, i.e., at the GQMOM quadrature nodes. By definition, we have the following relation between the conditional moments and the GQMOM quadrature:

$$\langle \phi \xi^k \rangle = \sum_{\alpha=0}^{N_g} w_\alpha \xi_\alpha^k \langle \phi | \xi = \xi_\alpha \rangle = \sum_{\alpha=0}^{N_g} w_\alpha \xi_\alpha^k \phi(\xi_\alpha) \tag{F.2}$$

where we define $\xi_0 = 0$. Analogous to eq. (56), this formula provides a set of N constraints, one for each value of k. If $N_g = N$, then the problem reduces to CQMOM since $\xi_\alpha = \hat{\xi}_\alpha$. Otherwise, we will use an interpolation formula to represent the function $\phi(\xi) = \langle \phi | \xi \rangle$ given the data $(\hat{\xi}_\alpha, \phi_\alpha)$ for $\alpha = 0, 1, \ldots, N$. The constraints in eq. (F.2) will be used to compute the unknowns, i.e., ϕ_α.

Let the interpolation formula have the form

$$\phi(\xi) = \sum_{\beta=0}^{N} f_\beta(\xi) \phi_\beta \tag{F.3}$$

with the property $\phi_\alpha = \phi(\hat{\xi}_\alpha)$, which implies that $f_\beta(\hat{\xi}_\alpha) = \delta_{\alpha,\beta}$. The interpolation functions $f_\alpha(\xi)$ depend on the type of interpolation, and on the QMOM abscissae. For example, we can use a linear interpolation between the QMOM nodes. In any case, the important point is that eq. (F.3) is linear in the unknowns ϕ_β. Thus, for example, when ϕ is independent of ξ, the interpolation functions must have the property $\sum_{\beta=0}^{N} f_\beta(\xi) = 1$ for all ξ. Using eq. (F.3) in eq. (F.2) gives the joint-moment constraints in terms of the unknowns:

$$\langle \phi \xi^k \rangle = \sum_{\alpha=0}^{N_g} w_\alpha \xi_\alpha^k \sum_{\beta=0}^{N} f_\beta(\xi_\alpha)\phi_\beta = \sum_{\beta=0}^{N} \langle \xi^k f_\beta \rangle \phi_\beta = \langle \xi^k f_0 \rangle \phi_0 + \sum_{\beta=1}^{N} \langle \xi^k f_\beta \rangle \phi_\beta \tag{F.4}$$

where we have introduced the notation

$$\langle \xi^k f_\beta \rangle = \sum_{\alpha=0}^{N_g} w_\alpha \xi_\alpha^k f_\beta(\xi_\alpha). \tag{F.5}$$

Note that after the interpolation method has been chosen $\langle \xi^k f_\beta \rangle$ can be computed using GQMOM. In other words, $\langle \xi^k f_\beta \rangle$ does not depend on the moments involving ϕ. In the case where $N_g = N$, we have $\langle \xi^k f_\beta \rangle = \hat{w}_\beta \hat{\xi}_\beta^k$, which corresponds to QMOM.

The linear system for GCQMOM is found from eq. (F.4) by setting $k = 0, 1, \ldots, N-1$:

$$\begin{bmatrix} \langle f_1 \rangle & \langle f_2 \rangle & \cdots & \langle f_N \rangle \\ \langle \xi f_1 \rangle & \langle \xi f_2 \rangle & \cdots & \langle \xi f_N \rangle \\ \vdots & \vdots & & \vdots \\ \langle \xi^{N-1} f_1 \rangle & \langle \xi^{N-1} f_2 \rangle & \cdots & \langle \xi^{N-1} f_N \rangle \end{bmatrix} \begin{bmatrix} \phi_1 \\ \phi_2 \\ \vdots \\ \phi_N \end{bmatrix} = \begin{bmatrix} \langle \phi \rangle - \langle f_0 \rangle \phi_0 \\ \langle \phi \xi \rangle - \langle \xi f_0 \rangle \phi_0 \\ \vdots \\ \langle \phi \xi^{N-1} \rangle - \langle \xi^{N-1} f_0 \rangle \phi_0 \end{bmatrix} \tag{F.6}$$

where ϕ_0 is known. Given that the abscissae coming from a Gaussian quadrature are distinct, the coefficient matrix is non-singular, in which case the solution to the linear system is unique. Thus, the interpolation function $\phi(\xi)$ found from eq. (F.3) is well defined and satisfies the joint-moment constraints.

Appendix F.2. Example of piece-wise linear interpolation with $N = 3$

In this case, the interpolation function is

$$\phi(\xi) = f_0(\xi)\phi_0 + f_1(\xi)\phi_1 + f_2(\xi)\phi_2 + f_3(\xi)\phi_3 \tag{F.7}$$

for the interval $\xi \in [0, \infty)$, and ϕ_0 is known. For piece-wise linear interpolation based on the mass, we have

$$\begin{aligned} f_0(\xi) &= I_{[0,\hat{\xi}_0)}(\xi) + \frac{\hat{\xi}_1 - \xi}{\hat{\xi}_1 - \hat{\xi}_0} I_{[\hat{\xi}_0,\hat{\xi}_1)}(\xi), \\ f_1(\xi) &= \frac{\xi - \hat{\xi}_0}{\hat{\xi}_1 - \hat{\xi}_0} I_{[\hat{\xi}_0,\hat{\xi}_1)}(\xi) + \frac{\hat{\xi}_2 - \xi}{\hat{\xi}_2 - \hat{\xi}_1} I_{[\hat{\xi}_1,\hat{\xi}_2)}(\xi), \\ f_2(\xi) &= \frac{\xi - \hat{\xi}_1}{\hat{\xi}_2 - \hat{\xi}_1} I_{[\hat{\xi}_1,\hat{\xi}_2)}(\xi) + \frac{\hat{\xi}_3 - \xi}{\hat{\xi}_3 - \hat{\xi}_2} I_{[\hat{\xi}_2,\hat{\xi}_3)}(\xi), \\ f_3(\xi) &= \frac{\xi - \hat{\xi}_2}{\hat{\xi}_3 - \hat{\xi}_2} I_{[\hat{\xi}_2,\hat{\xi}_3)}(\xi) + I_{[\hat{\xi}_3,\infty)}(\xi) \end{aligned} \tag{F.8}$$

where we set $\hat{\xi}_0 = 0$ in our code. Notice (i.e., final term in $f_3(\xi)$) that extrapolation with a constant value is used for this example. Another choice would be constant-slope extrapolation. The indicator function $I_{[a,b)}(x)$ is unity for $x \in [a, b)$ and zero otherwise. The functions in eq. (F.8) can be averaged using GQMOM to compute the coefficient matrices in eq. (F.6). In practice, interpolation based on the size (i.e., $\zeta = \xi^{1/3}$) or half-order mass (i.e., $\varsigma = \xi^{1/2}$) may be preferred.

For other interpolation schemes (e.g., cubic splines), the interpolation functions are more complex than in eq. (F.8). Nonetheless, the computational algorithm for finding ϕ_α from $\langle \xi^k \rangle$ and $\langle \phi \xi^k \rangle$ remains the same. It is important to note

that N_g can be made larger than N without changing the number of moment transport equations that must be solved in the polydisperse model. Thus, in theory at least, it would be possible to approximate more closely the mass NDF by increasing N_g without a significant increase in the computational cost. However, based on our experience with GQMOM [12], since the exact form of the mass NDF is unknown, the value of N, and not N_g, controls the accuracy of the approximation in most cases. Thus, choosing $N_g > 2N + 1$ usually will not lead to any further improvements. Likewise, setting the number of mass moments $N_s > 2N$ is only useful when the Stokes numbers of the particles are small such that the mass-conditioned particle velocities are close to the fluid velocity.